SEPARATING LOAD TORQUE OSCILLATION AND ROTOR FAULTS IN STATOR CURRENT BASED-INDUCTION MOTOR CONDITION MONITORING

A Dissertation
Presented to
The Academic Faculty

By

Long Wu

In Partial Fulfillment
Of the Requirements for the Degree
Doctor of Philosophy in Electrical Engineering

Georgia Institute of Technology

May 2007

SEPARATING LOAD TORQUE OSCILLATION AND ROTOR FAULTS IN STATOR CURRENT BASED-INDUCTION MOTOR CONDITION MONITORING

Approved by:

Dr. Thomas G. Habetler, Advisor
School of Electrical and Computer Engineering
Georgia Institute of Technology

Dr. Jennifer E. Michaels
School of Electrical and Computer Engineering
Georgia Institute of Technology

Dr. Ronald G. Harley
School of Electrical and Computer Engineering
Georgia Institute of Technology

Dr. J. Rhett Mayor
School of Mechanical Engineering
Georgia Institute of Technology

Dr. Deepakraj M. Divan
School of Electrical and Computer Engineering
Georgia Institute of Technology

Date Approved: December 8, 2006

Dedicated to my parents Mr. Zongwei Wu and Mrs. Guangrong Zhai

and my wife Mrs. Ruilin Tian

for their love and support

ACKNOWLEDGEMENTS

Few goals are ever achieved without the help of many other people. During my Ph.D. study at Georgia Tech, I have been very fortunate to receive tremendous guidance, encouragement and support from my mentors, colleagues, friends and family.

Dr. Thomas G. Habetler has been a wise and trusted advisor throughout the entire process. His confidence in my capabilities has given me immense opportunities to stimulate my research potential and improve my professional communication skills. I greatly appreciate his continuous guidance and support.

I am also grateful to Dr. Ronald G. Harley for his patient guidance, constant encouragement and invaluable suggestions for my research work. I have benefited significantly from his knowledge and experience. I would also like to thank Dr. Deepakraj M. Divan, Dr. Jennifer E. Michaels and Dr. J. Rhett Mayor for taking time to read my thesis and serve as my dissertation committee members.

I wish to express my gratitude to the Grainger Center for Electric Machinery and Electromechanics (CEME) at the University of Illinois and the Powerix Technologies, LLC for their generous financial support for the past three years.

I was fortunate to have many exceptional peers and colleagues in my research lab. Among them, I would like to give my sincere thanks to Dr. Xianghui Huang, Dr. Zhi Gao, Dr. Bin Lu, Wei Zhou, Young-kook Lee, Aristidis Zachas, Yi Yang, Wei Qiao and Dr. Sang-Bin Lee for their helpful discussions and collaborations. I also wish to thank Dr. Salman Mohagheghi, Dr. Satish Rajagopalan, Dr. Joy Mazumdar, Afroz Imam,

Harjeet Johal, Jyoti Sastry and other fellow graduate students in the electric power group for their friendship and company throughout my studies at Georgia Tech.

Most of all, I am deeply indebted to my parents for being an eternal source of support, encouragement and motivation throughout my life. My dear wife and best friend, Ruilin Tian, has been with me for every single step during this long journey. Without their generous love, support and understanding, everything I have accomplished would not have been possible.

TABLE OF CONTENTS

ACKNOWLEDGEMENTS ..... **iv**

LIST OF TABLES ..... **x**

LIST OF FIGURES ..... **xi**

SUMMARY ..... **xvi**

CHAPTER 1 INTRODUCTION **1**

1.1 Overview 1

1.2 Rotor Eccentricities in Induction Motors 2

1.3 Broken Rotor Bars in Induction Motors 4

1.4 Varying Mechanical Loads 4

1.4.1 Position-Varying Load Torque Oscillation 5

1.4.2 Single Frequency Oscillating Load Torque 6

1.4.3 Periodic Load Torque Dip 7

1.4.4 Random Load Torque Dip 8

1.5 Objective of the Research 8

1.6 Dissertation Outline 9

CHAPTER 2 SUMMARY OF PREVIOUS WORK ON SEPARATING LOAD EFFECTS FROM ROTOR FAULT DETECTION **11**

2.1 Overview 11

2.2 Model Reference Estimation 11

2.3 Current Park's Vector Approach 14

2.4 Vienna Monitoring Method 14

2.5 Other Techniques for Eliminating Load Effects 16
2.6 Mechanical Load Monitoring by Unsupervised NN Approach 19
2.7 Load Diagnostics Utilizing Instantaneous Power Spectrum 19
2.8 Load Fault Detection by Time-Frequency Analysis 21
2.9 Chapter Summary 22
CHAPTER 3 MAGNETIC FIELD ANALYSIS FOR ECCENTRIC MOTORS 24
3.1 Overview 24
3.2 Purely Rotor Static Eccentricity 24
3.2.1 Modified Stator and Rotor MMFs 25
3.2.2 Motor Inductance Reformulation 29
3.2.3 Motor Current Characteristics 32
3.3 Purely Dynamic Rotor Eccentricity 33
3.3.1 Modified Stator and Rotor MMFs 33
3.3.2 Motor Inductance Reformulation 34
3.3.3 Motor Current Characteristics 36
3.4 Mixed Rotor Eccentricity 36
3.4.1 Modified Stator and Rotor MMFs 36
3.4.2 Motor Inductance Reformulation 37
3.4.3 Motor Current Characteristics 44
3.5 Motor Current Characteristics for a Load Oscillation 44
3.6 Chapter Summary 45
CHAPTER 4 EXTRACTING NEGATIVE SEQUENCE HARMONIC INFORMATION 46
4.1 Overview 46

4.2 Traditional Symmetrical Component Decomposition 46

4.3 Rotating Reference Frame Transformation Method 48

4.4 New FFT Technique to Separate Sequence Information 51

4.5 Application for Phase-Phase Measurements 55

4.6 Chapter Summary 57

CHAPTER 5 DEVELOPMENT AND SIMULATION OF NEW ROTOR ECCENTRICITY FAULT INDICATORS 59

5.1 Overview 59

5.2 A New Eccentricity Indicator in Mains-Fed Machines 59

5.3 Matlab Simulation for a Mains-Fed Induction Motor 61

5.3.1 Induction Motor Dynamic Model 61

5.3.2 Purely Static Eccentricity in a Mains-Fed IM 65

5.3.3 Purely Dynamic Eccentricity in a Mains-Fed IM 70

5.3.4 Mixed Rotor Eccentricity in a Mains-Fed IM 72

5.3.5 Position-Dependent Load Oscillation in a Mains-Fed IM 77

5.4 A New Eccentricity Indicator for Drive-Connected Machines 79

5.5 Matlab Simulation for a Drive-Connected Induction Motor 82

5.5.1 Mixed Rotor Eccentricity in a Drive-Connected IM 84

5.5.2 Position-Dependent Load Oscillation in a Mains-Fed IM 84

5.6 Simulation Results Based on Finite Element Model 89

5.6.1 2-D Finite Element Model 89

5.6.2 Mixed Rotor Eccentricity for a Mains-Fed Machine 90

5.6.3 Position-Dependent Load Oscillation for a Mains-Fed Machine 90

5.6.4 FEA Simulation for a Drive-Connected Machine 93

5.7 Chapter Summary 94

CHAPTER 6 SEPARATING ROTOR ECCENTRICITY INDUCED MOTOR ASYMMETRY FROM OTHER SOURCES 95

6.1 Overview 95

6.2 Inherent Motor Asymmetry 95

6.3 Stator Inter-Turn Faults 95

6.4 Zero-Sequence Information 96

6.4.1 Zero-Sequence Information for a Stator Inter-Turn Fault 97

6.4.2 Zero-Sequence Information for Rotor Eccentricity 99

6.4.3 Comparison of Zero-Sequence Information 99

6.5 Chapter Summary 100

CHAPTER 7 EXPERIMENTAL SETUP AND IMPLEMENTATION OF LOAD TORQUE OSCILLATION 101

7.1 Overview - Basic Experimental Setup 101

7.1.1 Motor Eccentricity Implementation 101

7.1.2 Motor Dynamometer System 103

7.1.3 Closed-Loop Drive Configuration 103

7.1.4 Voltage and Current Measurements 104

7.2 Implementation of Load Torque Oscillation 105

7.2.1 Purely Load Oscillation Implementation Principle 105

7.2.2 IGBT Configurations 106

7.3 Chapter Summary 110

CHAPTER 8 RELIABLE ROTOR ECCENTRICTY DETECTION SCHEME AND EXPERIMENTAL RESULTS 111

8.1 Overview 111

8.2 Experimental Results for Mains-Fed Condition 112

8.3 Experimental Results for Closed-Loop Drive-Connected Condition 118

8.4 Reliable Rotor Eccentricity Detection Scheme 122

8.5 Chapter Summary 125

CHAPTER 9 CONCLUSIONS, CONTRIBUTIOINS, AND RECOMMENDATIONS FOR FUTURE WORK 127

9.1 Conclusions 127

9.2 Contributions 130

9.3 Recommendations for Future Work 131

APPENDIX A MOTOR PARAMETERS USED FOR SIMULATION 133

APPENDIX B MOTOR AND DRIVE PARAMETERS USED FOR EXPERIMENTS 134

APPENDIX C INTRODUCTIOIN TO SHARK DSP BOARD USED FOR CREATING LOAD OSCILLATIOIN 136

REFERENCES 138

VITA 145

LIST OF TABLES

Table 7.1 Mechanism to implement a quasi sinusoidal load oscillation..... 109

Table 8.1 Normalized negative sequence components at $-f_e$, $-(f_e + f_{rm})$ and $-(f_e - f_{rm})$ in supply currents..... 118

Table A.1 Motor parameters used for simulation..... 133

Table B.1 Nameplate information for the experimental motor..... 134

Table B.2 Impedance information for the experimental motor..... 134

Table B.3 Main parameters for the Allen-Bradley drive and encoder..... 135

LIST OF FIGURES

Figure 2.1 Block diagram of the model reference estimation 13

Figure 2.2 Vienna Monitoring Method voltage model (a) and current model (b) 15

Figure 2.3 Flowchart of the baseline calculation during the initiation stage 18

Figure 2.4 General structure of the ANN used for eccentricity detection under different load conditions 18

Figure 3.1 Static air-gap eccentricity. 27

Figure 3.2 An elementary 2-pole induction machine with static eccentricity, showing a closed magnetic loop abcda. 27

Figure 4.1 Positive and negative sequence harmonic space vector in (a) stationary reference frame and (b) rotating reference frame 51

Figure 4.2 Procedure to obtain per phase sequence components from phase-phase measurements 56

Figure 4.3 Relationship between sequence components from per-phase and phase-phase quantities 56

Figure 5.1 Simulink schematics using reformulated motor inductances for mains-fed machines 64

Figure 5.2 Simulated mains-fed i_a^s spectrum with $\xi_s = 0.5$, $\alpha = 0$, $slip = 0.0125$ 67

Figure 5.3 Simulated mains-fed i_q^f spectrum with $\xi_s = 0.5$, $\alpha = 0$, $slip = 0.0125$ 67

Figure 5.4 Simulated mains-fed $\vec{I}$ spectrum with $\xi_s = 0.5$, $\alpha = 0$, $slip = 0.0125$ 68

Figure 5.5 Normalized negative sequence fundamental component w.r.t. the load level where $\xi_s = 0.5$, $\alpha = 0$ 68

Figure 5.6 Normalized negative sequence fundamental component w.r.t. the degree of static eccentricity where $slip = 0.0125$, $\alpha = 0$ 69

Figure 5.7 Phase angle difference between positive and negative sequence components w.r.t. the motor fault position where $\xi_s = 0.5$ 69

Figure 5.8 Simulated mains-fed i_a^s spectrum with $\xi_d = 0.5$, $\beta = 0$, $slip = 0.0125$ 71

Figure 5.9 Simulated mains-fed $\vec{I}$ spectrum with $\xi_d = 0.5$, $\beta = 0$, $slip = 0.0125$ 71

Figure 5.10 Simulated mains-fed i_a^s spectrum with $\xi_s = 0.5$, $\xi_d = 0.5$, α=15°, $\beta = 0$, $slip = 0.0125$ 73

Figure 5.11 Simulated mains-fed $\vec{I}$ spectrum with $\xi_s = 0.5$, $\xi_d = 0.5$, α=15°, $\beta = 0$, $slip = 0.0125$ 73

Figure 5.12 Simulated mains-fed motor shaft speed profile with $\xi_s = 0.5$, $\xi_d = 0.5$, α=15°, $\beta = 0$, $slip = 0.0125$ 74

Figure 5.13 Simplified Simulink schematics to simulate mains-fed rotor eccentricities 74

Figure 5.14 Simulated mains-fed i_a^s spectrum with $\xi_s = 0.3$, $\xi_d = 0.2$, α=0, $\beta = 0$, $slip = 0.0125$ 75

Figure 5.15 Simulated mains-fed $\vec{I}$ spectrum with $\xi_s = 0.3$, $\xi_d = 0.2$, α=0, $\beta = 0$, $slip = 0.0125$ 76

Figure 5.16 Simulated mains-fed motor shaft speed profile with $\xi_s = 0.3$, $\xi_d = 0.2$, α=0, $\beta = 0$, $slip = 0.0125$ 76

Figure 5.17 Simulated mains-fed i_a^s spectrum with 100% load torque oscillation 77

Figure 5.18 Simulated mains-fed $\vec{I}$ spectrum with 100% load torque oscillation..... 78

Figure 5.19 Simulated mains-fed motor shaft speed profile for a healthy motor with 100% load torque oscillation..... 78

Figure 5.20 A typical closed-loop induction motor drive system..... 80

Figure 5.21 Simulink schematics using reformulated motor inductances for closed-loop drive-connected machines..... 83

Figure 5.22 Simulated drive-connected i_a^s spectrum with $\xi_s = 0.3$, $\xi_d = 0.2$, α=0, $\beta = 0$ 85

Figure 5.23 Simulated drive-connected v_a^s spectrum with $\xi_s = 0.3$, $\xi_d = 0.2$, α=0, $\beta = 0$ 85

Figure 5.24 Simulated drive-connected $\vec{I}$ spectrum with $\xi_s = 0.3$, $\xi_d = 0.2$, α=0, $\beta = 0$ 86

Figure 5.25 Simulated drive-connected $\vec{V}$ spectrum with $\xi_s = 0.3$, $\xi_d = 0.2$, α=0, $\beta = 0$ 86

Figure 5.26 Simulated drive-connected i_a^s spectrum with 100% load torque oscillation 87

Figure 5.27 Simulated drive-connected v_a^s spectrum with 100% load torque oscillation 87

Figure 5.28 Simulated drive-connected $\vec{I}$ spectrum with 100% load torque oscillation 88

Figure 5.29 Simulated drive-connected $\vec{V}$ spectrum with 100% load torque oscillation 88

Figure 5.30 Maxwell 2D model for the induction motor 89

Figure 5.31 FEA model simulated mains-fed i_a^s spectrum with 30% static eccentricity and 30% dynamic eccentricity 91

Figure 5.32 FEA model simulated mains-fed $\vec{I}$ spectrum with 30% static eccentricity and 30% dynamic eccentricity 91

Figure 5.33 FEA model simulated mains-fed i_a^s spectrum with 50% load torque oscillation 92

Figure 5.34 FEA model simulated mains-fed $\vec{I}$ spectrum with 50% load torque oscillation 92

Figure 5.35 Maxwell 2D solver setup interface 93

Figure 7.1 Illustration of experimental setup with load oscillation control circuit 102

Figure 7.2 Stator winding configuration for 230 Volts operation 104

Figure 7.3 Schematics to control load torque oscillation..... 107

Figure 7.4 Quasi sinusoidal load torque oscillation profile 107

Figure 7.5 IGBT board configuration 109

Figure 7.6 Connection between the DSP board and IGBT board..... 109

Figure 8.1 Mains-fed eccentric motor $\vec{I}$ spectrum at 1776 rpm with constant load... 115

Figure 8.2 Mains-fed healthy motor $\vec{I}$ spectrum at 1776 rpm with constant load..... 116

Figure 8.3 Mains-fed healthy motor $\vec{I}$ spectrum at average 1776 rpm with load oscillation 116

Figure 8.4 Normalized negative sequence harmonic currents at $-\left(f_e + f_{rm}\right)$ for an eccentric motor with constant load and a healthy motor with load oscillation 117

Figure 8.5 Normalized negative sequence harmonic currents at $-\left(f_e - f_{rm}\right)$ for an eccentric motor with constant load and a healthy motor with load oscillation 118

Figure 8.6 FFT spectrum of stator current space vector for the eccentric motor..... 119

Figure 8.7 FFT spectrum of stator voltage space vector for the eccentric motor 119

Figure 8.8 FFT spectrum of stator current space vector for the healthy motor 119

Figure 8.9 FFT spectrum of stator voltage space vector for the healthy motor..... 120

Figure 8.10 Normalized fundamental negative sequence stator current vs. reference speed..... 123

Figure 8.11 Normalized fundamental negative sequence stator voltage vs. reference speed..... 124

Figure 8.12 Normalized total fundamental negative sequence components vs. reference speed..... 124

Figure 8.13 Proposed complete online rotor eccentricity fault detection scheme for induction motors..... 126

Figure C.1 ADSP 21061 EZ-KIT Lite board layout..... 137

SUMMARY

Stator current spectral analysis techniques are usually used to detect rotor faults in induction machines. Magnetic field anomalies in the air-gap due to the rotor faults result in characteristic side-band harmonic components in the stator current spectrum, which can be measured as rotor fault signatures. A position-varying load torque oscillation at multiples of the rotational speed, however, has exactly the same effect. Stator current harmonics due to a load torque oscillation often obscure and even overwhelm rotor eccentricity fault detection since the magnitude of load oscillation induced harmonics is usually much larger.

Although previous research has suggested some methods to differentiate between these two effects, most of them rely heavily on the accurate estimation of motor parameters. The objective of this research is to develop a far more practical and computationally efficient method to detect rotor faults effectively in the presence of a load torque oscillation. A significant advantage of the proposed scheme is that it does not need any knowledge of motor parameters. The normalized negative sequence information induced by a mixed rotor eccentricity in the stator current or stator voltage space vector spectra, serves as a reliable rotor fault indicator to eliminate load oscillation effects.

Detailed airgap magnetic field analysis for an eccentric motor is performed and several machine inductance matrices as well as their derivatives are reformulated accordingly. Careful observation of these inductance matrices provides a fundamental understanding of motor operation characteristics under a fault condition. Simulation

results based on both induction motor dynamic model and Maxwell® 2D Finite Element Model demonstrate clearly the existence of the predicted rotor fault indicator. Extensive experimental results also validate the effectiveness and feasibility of the proposed detection scheme.

CHAPTER 1

INTRODUCTION

1.1 Overview

The induction motor (IM) has been the horse power of industry for many years. In an industrialized nation, they can typically consume 40%-50% of all the generated capacity of that country. Effective online condition monitoring of IMs is critical to improving the productivity, reliability and safety to avoid unexpected downtime and expensive repair cost. Therefore, the diagnosing of the health condition of IMs is receiving more and more attention from industry in the past decades since it can detect an incipient fault at an early stage. In general, noninvasive detection methods, such as the motor current signature analysis (MCSA) technique [1]-[3], for condition monitoring is preferred over other methods since it does not disturb the normal operation of IMs. In addition, the only required detection variables are the terminal supply currents, which are readily available in the motor control center (MCC). The most common two types of rotor faults are rotor eccentricities and broken rotor bars. Both of them introduce some fault characteristic harmonics in the stator current which can be monitored to detect rotor faults. Meanwhile, some mechanical load conditions have similar effects on the stator current spectrum, which may cause ambiguity either in the condition monitoring of IMs or in the mechanical fault detection [5]-[21].

1.2 Rotor Eccentricities in Induction Motors

Basically, there are two types of eccentricities: static eccentricity and dynamic eccentricity. In the case of a static eccentricity, the minimum radial airgap length is fixed in space. The center of rotation is located at the center of rotor and is away from the center of the stator bore. Static eccentricity might come from improper positioning of stator core and rotor cage, stator core ovality, an excessive axial load, or worn bearings. However, in the case of a dynamic eccentricity, the minimum radial airgap length is rotating with the rotor around the stator inner periphery, yet the center of rotation is still located at the center of stator. Dynamic eccentricity might come from a bent rotor shaft or operating at some critical speeds which cause mechanical resonance. In practice, both types of eccentricities tend to coexist because there is always an inherent level of static or dynamic eccentricity even in a newly commissioned motor due to the manufacturing and assembly imperfections. Therefore, purely static or dynamic eccentricity does not exist in a real machine.

Rotor eccentricities produce a radial magnetic force on the rotor shaft, which is well known as the unbalanced magnetic pull (UMP). UMP acts to pull the rotor even further away from the stator bore center. This enforced rotor displacement causes excessive stress on the machine and greatly increases bearing wear. Unless detected early, these effects may snowball finally into a stator-to-rotor rub, leading to significant damage to the stator core, stator windings, and rotor cage. Eventually, this damages results in a major breakdown of the machine and a costly repair.

Due to the airgap permeance modulation of the induced stator and rotor MMFs as well as the interactions among the static eccentricity, dynamic eccentricity, stator and

rotor slotting effects, saturation effects, and even stator and rotor space and time harmonics, rotor eccentricities give rise to the appearance of some high frequency characteristic side-band harmonics in the stator current spectrum, whose frequencies are located at [27],

$$f_{ecc\_high} = \left[(nR \pm n_d) \cdot (\frac{1-s}{p}) \pm 2n_{sa} \pm n_{ws} \right] \cdot f_e \qquad (1.1)$$

where $n = 1,\ 2,\ 3,\ldots$ is the rotor slotting effect order number, R is the number of rotor bars, n_d is the dynamic eccentricity order number ($n_d = 0$ corresponds to a pure static eccentricity), s is the per unit slip, p is the fundamental pole pair number, n_{sa} is the saturation effect order number, n_{ws} is the stator MMF time harmonics order number and f_e is the fundamental supply frequency, which is 60Hz in the U.S. The principal slot harmonics (PSHs) are also given in (1.1) by $n_d = 0$, $n_{sa} = 0$ and $n_{ws} = 1$. Frequency components given by (1.1) associated with triplen pole pair numbers should be ideally absent in the supply currents of a balanced 3-phase IM [4]. In other words, the eccentricity related high frequency characteristic harmonics can only have harmonic pole pair numbers of $m \cdot p$, where $m = 1,\ 5,\ 7,\ 11,\ 13,\ldots$ Obviously, the dominant characteristic frequency corresponds to the fundamental pole pair number p when $m = 1$. If the motor can not be dismantled to find the exact number of rotor bars, detecting rotor eccentricities using (1.1) might cause problems. In addition, it was demonstrated in [4] that for some combinations of p and R, the components given by (1.1) may not be present in the stator current spectrum. Moreover, with the increasing use of inverter-fed induction motor drives, these high frequency harmonics become difficult to identify due to the drive control loop filtering effects [24]-[28].

In the presence of a mixed eccentricity, low frequency side-band harmonics will also appear in the stator current spectrum. They are located at [24]-[26],

$$f_{ecc\_low} = (1 \pm k \cdot \frac{1-s}{p}) \cdot f_e \tag{1.2}$$

where k is an integer. The dominant low frequency characteristic fault components correspond to the case where $k = 1$. The existence of these harmonics is due to the interaction between both types of eccentricity. Theoretically speaking, only when both static eccentricity and dynamic eccentricity exist simultaneously, will harmonics given by (1.2) be expected to appear. Since there is always some residual level of static or dynamic eccentricity, (1.2) is commonly monitored to detect rotor eccentricities, irrespective of the combination of p and R.

1.3 Broken Rotor Bars in Induction Motors

For broken bar type of rotor faults, the corresponding side-band characteristic harmonics are located at [1]-[3],

$$f_{brb} = (1 \pm 2 \cdot k \cdot s) \cdot f_e \tag{1.3}$$

Again, the main fault indicators in the presence of this type of rotor fault correspond to the case where $k = 1$. However, if s is very small (at light load condition) or the FFT spectral resolution is too coarse, detecting broken rotor bars using (1.3) may pose some difficulty due to the intrinsic spectral leakage property of the FFT algorithm.

1.4 Varying Mechanical Loads

State of the art condition monitoring schemes for IM rotor faults are usually developed under the assumption of a constant load torque condition. Abnormal mechanical load conditions and varying load levels, however, have also a significant

impact on the characteristic fault signatures in the current spectrum. For example, the magnitudes of the low frequency side-band harmonics in (1.2) used for detecting rotor eccentricities can vary remarkably from no load to full load [12].

Some types of mechanical faults such as unbalanced load, angular and radial shaft misalignments, etc., essentially create a rotor eccentricity inside the motor. Therefore, detecting these mechanical faults can directly take advantage of those fault indicators expressed in (1.2). Other types of mechanical load anomalies may also introduce exactly the same side-band harmonics in the stator current spectrum while there is no impact on the rotor shaft. Alternatively speaking, these mechanical load anomalies do not produce any rotor faults inside the motor itself. Hence ambiguity may arise when detecting either rotor faults or mechanical load anomalies by analyzing side-band harmonics in a single phase stator current spectrum. These mechanical load anomalies include several working modes. Their expressions and corresponding effects on the stator current spectrum are briefly summarized below.

1.4.1 Position-Varying Load Torque Oscillation

A position-varying load torque oscillation has the following expression,

$$T_{load} = T_{avg} + \eta \cdot T_{avg} \cdot \cos(\theta_{rm}) \tag{1.4}$$

where T_{avg} is the average load torque, θ_{rm} is the mechanical rotor angle with respect to the stator, and the coefficient η denotes the load torque oscillation level. The value of η can be as more than 1.0 for some applications such as reciprocating compressors [5].

Assuming the mechanical system is linear, all the frequency components in the load torque will appear in the shaft torque, thus leading to a torque ripple in T_{em}. In an ideal

induction motor model with purely sinusoidal input voltage and negligible stator resistance, the qd-axis stator flux linkages contain only fundamental components. The instantaneous torque in an arbitrary reference frame is given by,

$$T_{em} = (\frac{3}{2}) \cdot p \cdot (\lambda_{ds} i_{qs} - \lambda_{qs} i_{ds}) \tag{1.5}$$

Obviously, any oscillation in the load torque at a multiple of the rotational speed $k \cdot f_{rm}$ will induce corresponding side-band harmonics in the stator current spectrum at,

$$f_{load} = f_e \pm k \cdot f_{rm} = (1 \pm k \frac{1-s}{p}) f_e \tag{1.6}$$

where f_{rm} is the rotor mechanical rotation frequency. It is clear that, equations (1.2) and (1.6) represent the same stator current side-band harmonics. Since the load oscillation-induced harmonics usually have a larger magnitude than those resulting from rotor eccentricities, it is very difficult to differentiate these two effects using conventional single phase stator current spectral analysis techniques.

1.4.2 Single Frequency Oscillating Load Torque

Similar to the previous case, one can consider an oscillating load torque at a single frequency f_0 superimposed to a constant average torque. The load torque can be expressed as,

$$T_{load} = T_{avg} + \eta \cdot T_{avg} \cdot \cos(2\pi f_0 t) = T_{avg} + T_{osc} \cos(2\pi f_0 t) \tag{1.7}$$

If both T_{osc} and f_0 are considerably small with respect to T_{avg} and f_s, respectively, the problem can be treated using a small signal approach. Analytical derivation [15] shows that side-band harmonics at $f_e \pm f_0$ appear in the stator current spectrum and the

amplitude of the harmonic current modulation ΔI is related to the load torque oscillation, ΔT_{load}, by,

$$\frac{\Delta I}{\sqrt{2} I cos\varphi} = \frac{\Delta T_{em}}{T_{avg}} = \frac{\xi}{\sqrt{\xi^2 + (2\pi f_0 J)^2}} \frac{\Delta T_{load}}{T_{avg}} \tag{1.8}$$

where $\sqrt{2} I cos\varphi$ is the fundamental stator current corresponding to the average load torque with $cos\varphi$ being power factor, ξ is the ratio between the shaft torque ripple and rotor speed ripple with $\xi = \Delta T_{em}(t) / \Delta \omega_{rm}(t)$, and J is the motor-load system inertia. At very low frequencies, if $2\pi f_0 J \ll \xi$, the shaft torque ripple is almost equal to the load torque ripple. As the frequency increases, the effect of load disturbance on the shaft torque and stator current will decrease accordingly.

1.4.3 Periodic Load Torque Dip

A typical periodic load disturbance is a dip in the torque. In this case, the spectrum of the load torque, assuming a period equal to $1/f_0$, will contain a fundamental component at frequency f_0, and a sequence of high order harmonics at frequencies $k \cdot f_0$, whose magnitudes obviously depend on the duty ratio of the torque dip. The total effect of this type of load anomaly can be considered as a superposition of a series of single frequency oscillating loads. Therefore, side-band harmonics located at $f_e \pm k \cdot f_0$ will appear in the stator current spectrum. In the case that f_0 is very close to the double slip frequency, i.e., $f_0 \approx 2s \cdot f_e$, the detection of broken rotor bars using fault indications in (1.3) may be confused by a periodic dip in the load torque.

1.4.4 Random Load Torque Dip

In case of a random dip in the load torque, the sliding window plays an important role in the spectral analysis. Different widths of the selected observation window assign different periods to the random dip signal in the load torque. The classical stator current spectral analysis is not suitable to detect this type of load anomaly since the location of fault signatures in the stator current spectrum depends on the selected width of the observation window. Time-frequency spectral approaches such as the Wigner Distribution method has to be employed to detect this type of load fault.

1.5 Objective of the Research

As can be seen from the background introduction presented in previous sections, both rotor faults and mechanical load anomalies introduce similar harmonic patterns in the stator current spectrum, which may cause ambiguity in condition monitoring of IMs. The objective of this research is to develop a simple, motor parameter-independent scheme to effectively detect rotor eccentricity faults in the presence of a position-varying load torque oscillation.

A mixed rotor eccentricity introduces unbalance in the motor parameters, which further leads to increased negative sequence information in the three phase supply currents. However, in the case of a position dependent load torque oscillation, the motor itself is still symmetric. Ideally only positive sequence information should exist in the stator currents. Therefore, by detecting the increased motor asymmetry level from the motor terminal quantities, these two effects can be effectively separated.

The ultimate goal of this research is to develop a reliable, computationally efficient and load independent algorithm for online rotor eccentricity detection in both mains-fed and drive-connected induction motors.

1.6 Dissertation Outline

A comprehensive literature review on the existing techniques to separate load effects from rotor fault detection is given in Chapter 2. Their respective merits and shortcomings are summarized to familiarize the reader with the background framework of this research. In Chapter 3, a detailed magnetic field analysis in the airgap due to a purely static eccentricity, a purely dynamic eccentricity and a mixed rotor eccentricity is presented. All kinds of machine inductances as well as their derivatives are reformulated accordingly. In order to accurately extract negative sequence harmonic information from three phase currents, a new FFT technique is proposed in Chapter 4. This method has significant advantages over the traditional symmetrical component decomposition method for this application.

Based on the fundamental understanding of motor operating characteristics under a fault condition, a new rotor eccentricity indicator is proposed in Chapter 5. Simulation results from both a simplified Matlab Simulink model and a time-consuming Finite Element Model are also presented in this Chapter. Considering that the motor asymmetry may also result form a possible stator inter-turn fault, zero-sequence information is utilized to distinguish these two causes. A detailed mathematical derivation on this topic is given in Chapter 6.

Chapter 7 describes the basic experimental setup including eccentric and healthy motors, the dynamometer, the closed-loop drive and the data acquisition system. The

principle and implementation method for the load torque oscillation are also explained therein. Experimental results for a mains-fed motor and a closed-loop drive-connected motor, with man-made eccentricity or with load torque oscillation, are all given in Chapter 8, in order to demonstrate the effectiveness of the proposed new rotor eccentricity indicator. Based on these experimental results, a reliable, computational efficient and load independent rotor eccentricity detection scheme is illustrated.

Finally, Chapter 9 concludes the dissertation and describes the contribution of this research as well as the recommended future remaining work.

CHAPTER 2

SUMMARY OF PREVIOUS WORK ON SEPARATING LOAD EFFECTS FROM ROTOR FAULT DETECTION

2.1 Overview

Both rotor eccentricity and broken rotor bar faults may be confused with different types of load anomalies in the stator current spectrum. Although these two types of rotor faults have different natures, they share the same basic rotor fault detection scheme. A single phase stator current is analyzed by FFT and corresponding characteristic fault signatures are located according to (1.2) or (1.3). In addition, the varying mechanical load levels or mechanical resonance points have significant impacts on the rotor faults detection as well. The literature review of this chapter will address these issues since they all deal with the same topic of separating load effects from rotor fault detection.

2.2 Model Reference Estimation

The research work of [5]-[7] proposes a scheme to determine the machine health condition in the presence of a position-varying load torque oscillation. This is accomplished by comparing the actual stator current to a model reference value which includes the load effects. The difference between these two signals provides a filtered quantity which is independent of load variations. This load independent current information can be used for continuous on-line condition monitoring without concern for the load effects.

In the synchronous reference frame with the d-axis aligned with the rotor flux linkage, the d-axis voltage equations can be written as,

$$v_{ds}^{er} = R_s i_{ds}^{er} - \omega_e \lambda_{qs}^{er} + \frac{d}{dt}\lambda_{ds}^{er} \tag{2.1}$$

$$v_{dr}^{er} = 0 = R_r i_{dr}^{er} + \frac{d}{dt}\lambda_{dr}^{er} \tag{2.2}$$

Obviously, equation (2.2) is independent of the rotor angular speed ω_r. Since the inductances still keep constant in the presence of a load oscillation, combining (2.2) with the d-axis flux linkage equations,

$$\lambda_{ds}^{er} = L_s i_{ds}^{er} + L_m i_{dr}^{er} \tag{2.3}$$

$$\lambda_{dr}^{er} = L_m i_{ds}^{er} + L_r i_{dr}^{er} \tag{2.4}$$

gives the following expression for the derivative of the d-axis stator current,

$$\frac{d}{dt} i_{ds}^{er} = \frac{R_r L_s i_{ds}^{er} - R_s \lambda_{ds}^{er} - L_r \frac{d}{dt}\lambda_{ds}^{er}}{L_m^2 - L_r L_s} \tag{2.5}$$

expressed in terms of stator variables only. Rearranging (2.1) allows the derivative of the d-axis stator flux linkage to be written as,

$$\frac{d}{dt}\lambda_{ds}^{er} = v_{ds}^{er} - R_s i_{ds}^{er} + \omega_e \lambda_{qs}^{er} \tag{2.6}$$

As shown in Figure 2.1, the derivative equations (2.5) and (2.6) can be used in the estimator to determine the present change rate in the d-axis stator current for an ideal machine under arbitrary load conditions. Once $\frac{d}{dt} i_{ds}^{er}$ has been determined in the estimator from the measured stator currents and voltages, the d-axis stator current at the next sampling instant can be estimated by Euler's method,

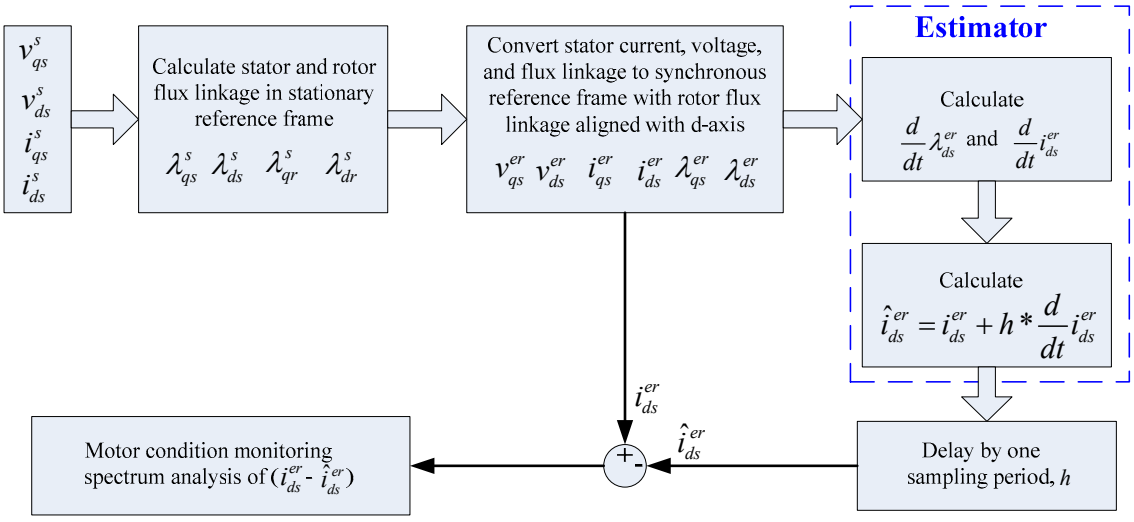

Figure 2.1 Block diagram of the model reference estimation

$$\hat{i}_{ds}^{er}(N+1) = i_{ds}^{er}(N) + h * \frac{d}{dt} i_{ds}^{er}(N) \tag{2.7}$$

where h is the time interval between two sampling points. The estimated d-axis stator current $\hat{i}_{ds}^{er}$ is then subtracted from the actually measured quantity i_{ds}^{er}. This difference is significant since it provides a detectable signal which is independent of the load effects while still containing the stator current harmonics information introduced by the rotor fault effects.

The major drawback of this scheme lies in its heavy dependence on the accurate estimate of motor parameters including R_s, R_r, L_m, L_{ls} and L_{lr}. In general, it is very difficult, if not impossible, to achieve such an accurate estimate due to the temperature rise, magnetic saturation and skin effects. Since the estimation scheme assumes the load torque remain constant during the sampling interval, the sampling frequency has a direct impact on the elimination of load effects. Meanwhile, in order to produce a sufficiently high frequency resolution in FFT analysis, the total sampling time can not be too short.

Therefore, the computational cost and memory requirement are relatively high for this scheme.

2.3 Current Park's Vector Approach

Cruz and Cardoso suggest using the synchronous reference frame Park's Vector Approach to detect rotor faults [8]-[9]. It is claimed that, by using this approach, effects of rotor faults can be differentiated from time-varying loads. Simulation results presented in this research work demonstrate that, for a time-varying mechanical load, the current Park's Vector representation in the synchronous reference frame is essentially a straight line, which is tangential to the classical circle diagram of the induction motor. However, the occurrence of broken rotor bar faults is characterized by the appearance of an elliptic pattern, whose major axis length is directly related to the severity degree of rotor faults. Onsite test results give a vague indication to identify rotor faults from time-varying loads. In summary, although this method can provide some clue to differentiate rotor faults from load effects, the confidence level of this judgment is relatively low, thus prevent it from serving as a reliable rotor fault indicator in the presence of a load torque oscillation.

2.4 Vienna Monitoring Method

The Vienna Monitoring Method (VMM) is based on the comparison of the calculated torque values from a voltage model and a current model [10]-[11], as shown in Figure 2.2. For an ideally symmetric machine, torque values from these two models should be equal. Rotor faults, however, lead to two different torque values. Therefore, broken bar type of rotor faults can be detected by assessing the ripple component in the torque difference at the double slip frequency.

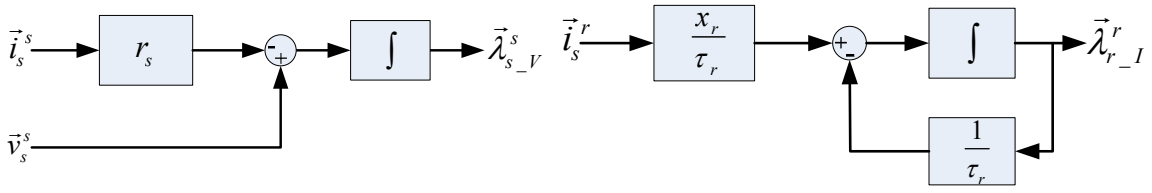

(a) (b)

Figure 2.2 Vienna Monitoring Method voltage model (a) and current model (b)

In the voltage model, the stator flux linkage space vector can be calculated by,

$$\frac{d}{dt}\vec{\lambda}_{s\_V}^{\,s} = \vec{v}_s^{\,s} - r_s\vec{i}_s^{\,s} \tag{2.8}$$

in the stationary reference frame. The current model is described in the rotor reference frame as,

$$\frac{d}{dt}\vec{\lambda}_{r\_I}^{\,r} + \frac{1}{\tau_r}\vec{\lambda}_{r\_I}^{\,r} = \frac{x_r}{\tau_r}\vec{i}_s^{\,r} \tag{2.9}$$

Transformation of the stator current space vector between the stationary and rotor reference frames is defined by,

$$\vec{i}_s^{\,s} = \vec{i}_s^{\,r} e^{j\omega_r t} \tag{2.10}$$

The voltage model and current model related torque values can be calculated as follows,

$$t^V = -\mathrm{Im}(conj(\vec{i}_s^{\,s})\vec{\lambda}_{s\_V}^{\,s}) \tag{2.11}$$

$$t^I = -\mathrm{Im}(conj(\vec{i}_s^{\,r})\vec{\lambda}_{r\_I}^{\,r}) \tag{2.12}$$

A broken bar rotor fault leads to a torque difference from two models. In order to eliminate the dependence on the load torque level, it is desirable to divide the torque difference by an estimated load torque and obtain a normalized torque difference signal,

$$\Delta\tilde{t} = \frac{t^V - t^I}{t_{load}} \tag{2.13}$$

The amplitude of this normalized quantity is independent of load level. The second harmonic component in (2.13) will server as the rotor fault indicator.

The primary advantage of VMM method is its independence on the varying load torque level and inertia although this scheme is still not reliable for light load conditions. In general, situations with load torque values below a certain threshold (around 40% of the full load) should be excluded for diagnostics using VMM. The effects of time-varying load torque oscillation on rotor faults detection in VMM are not clear yet. Similar to the model reference estimation method, the VMM also suffers significantly from the inaccurate estimate of motor parameters including stator resistance r_s, rotor reactance x_r and rotor time constant τ_r.

2.5 Other Techniques for Eliminating Load Effects

In recent publications, some other techniques are also proposed to eliminate varying load torque level and mechanical resonance effects on the stator current based-condition monitoring of IMs. Obaid [12]-[13] takes into account these issues by classifying the load levels into several bins and calculating an average threshold value for each load bin. To avoid missing mechanical resonance points within any load bin, the final baseline is obtained by sweeping the load level throughout each bin and then calculating an average baseline for different load levels within the bin. All final baselines for different load bins are computed during the initialization stage of the algorithm and combined together to serve as the fault threshold with a 50% tolerance margin. When the threshold value is continuously compared with actually measured fault signals, the health condition of IMs

can be detected under any load level. The flow chart of this baseline initialization procedure is shown in Figure 2.3.

Huang [14] realized the similar idea for the rotor eccentricity detection in a closed-loop drive-connected induction motor by using a supervised multi-layer perceptron feed forward neural network (MLP-FF-NN). In an AC drive, the mechanical speed can vary widely. This results in a variation in the eccentricity-related characteristic fault frequency, load level and magnitudes of the fault harmonics. The relationship between the harmonic magnitude and the load level (rotor speed) is non-monotonic in general due to the mechanical resonance effects. Since it is very difficult or even impossible to formulate this relationship in a strictly analytical manner, an artificial neural network (ANN) can be used to learn these complex relationships with only a finite number of operating points, and then estimating remaining fault signature amplitudes for other operating conditions. The actual motor speed ω_m and corresponding fundamental drive supply frequency f_1 are used as input to the ANN to determine the motor slip and thus the operating point. The output layer of the ANN gives the system output, namely the eccentricity related total harmonic amplitude $v_{f_{ecc}} + i_{f_{ecc}}$ as shown in Figure 2.4. After the training procedure is complete, the ANN is ready to detect rotor eccentricity fault under any operating condition.

In both techniques, data must be collected for a healthy motor at several operating points during the initialization or training stage. For some applications, however, it may not be possible to enforce this learning procedure.

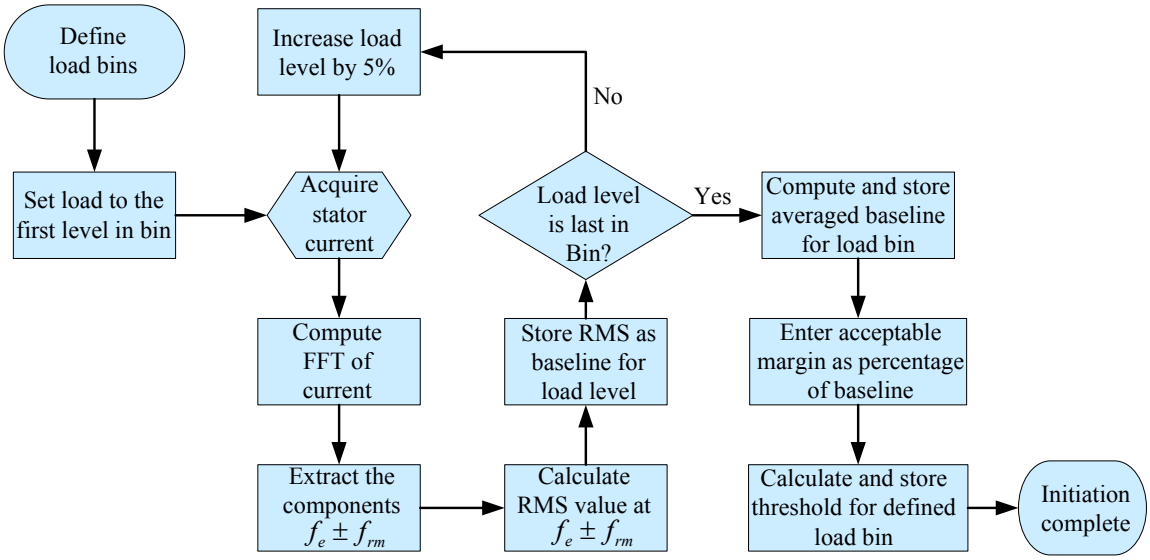

Figure 2.3 Flowchart of the baseline calculation during the initiation stage

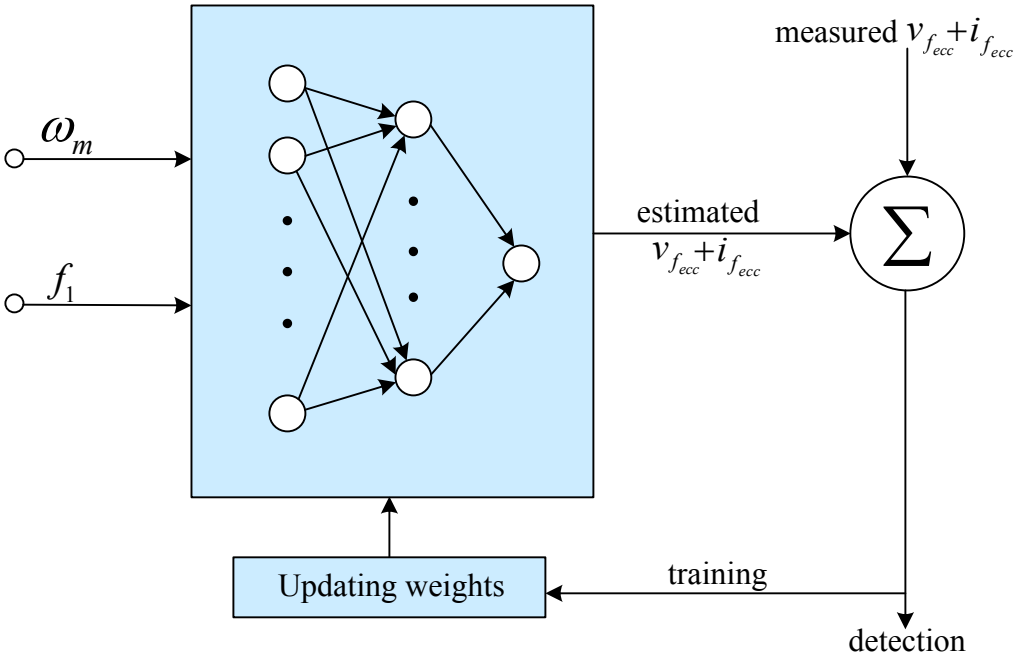

Figure 2.4 General structure of the ANN used for eccentricity detection under different load conditions

2.6 Mechanical Load Monitoring by Unsupervised NN Approach

As discussed in section 1.4, different types of mechanical load anomalies also introduce harmonic patterns in the stator current spectrum. Although induction motor itself can serve as a torque sensor to detect load troubles, this procedure may be misunderstood due to rotor fault effects. Salles and Filippetti [15]-[18] suggest an unsupervised self-organization mapping (SOM) neural network to distinguish among the signatures introduced by different load faults and those introduced by other machine troubles such as rotor faults. This technique utilizes a selected set of current spectral components as inputs to the system to perform fault classification. The data sets constructed from computer simulation results are used to train the neural network offline. Therefore, this method may not be suitable for online condition monitoring due to the relatively high computational cost. In addition, for each new type of motor, a set of new simulation results has to be produced to facilitate the training process. Experimental results demonstrate a good capability to distinguish among the periodic torque dip, single frequency oscillating torque and healthy mode. However, the distinction between the oscillating torque and broken bar fault, as well as that between the periodic dip and random dip are not explicit. Although it is possible to increase the dimension of the NN size to achieve better performance, the total computation cost increases accordingly.

2.7 Load Diagnostics Utilizing Instantaneous Power Spectrum

Assuming an ideal three phase supply and a healthy stator winding, the instantaneous power is defined as [19]-[20],

$$p(t) = v_{LN}(t) \cdot i_L(t) \tag{2.14}$$

where $v_{LN}(t)$ is the line-to-neutral voltage and $i_L(t)$ is the terminal phase current. For an ideal machine running at a constant load, the reference instantaneous power is given by,

$$\begin{aligned} p_0(t) &= V_m cos(2\pi f_s t) \cdot I_m cos(2\pi f_s t - \varphi) \\ &= \frac{V_m \cdot I_m}{2}[cos(2\pi(2f_s)t - \varphi) + \cos(\varphi)] \end{aligned} \tag{2.15}$$

where V_m and I_m denote the voltage and current amplitudes, respectively, and φ is the load angle. It is clear to see the instantaneous power spectrum include both DC component and fundamental component at $2f_s$. Assuming a mechanical fault causes a sinusoidal modulation of the stator current amplitude and the load angle φ does not change significantly, the modulated stator current can be expressed as,

$$\begin{aligned} i_L(t) &= I_m cos(2\pi f_s t - \varphi) \cdot [1 + Mcos(2\pi f_0 t)] \\ &= I_m cos(2\pi f_s t - \varphi) + \frac{MI_m}{2} cos[(2\pi(f_s - f_0)t - \varphi)] \\ &\quad + \frac{MI_m}{2} cos[(2\pi(f_s + f_0)t - \varphi)] \end{aligned} \tag{2.16}$$

where M is the modulation index and f_0 is the modulation frequency. Clearly, two side-band harmonics appear in the stator current spectrum. Combing equations (2.14) and (2.16) gives the modulated instantaneous power as,

$$\begin{aligned} p = p_0(t) &+ \frac{MV_m I_m}{2} cos(\varphi) cos(2\pi f_0 t) \\ &+ \frac{MV_m I_m}{4} cos[(2\pi(2f_s - f_0)t - \varphi)] + \frac{MV_m I_m}{4} cos[(2\pi(2f_s + f_0)t - \varphi)] \end{aligned} \tag{2.17}$$

Except for the fundamental and two side-band harmonics at $(2f_s - f_0)$ and $(2f_s + f_0)$, there exists an additional component located at the modulation frequency f_0 in (2.17). The last component provides extra diagnostic information in load fault detection.

Simulation results in [19] demonstrate that this technique has some advantages over other techniques in detecting mechanical load anomalies. However, it is still difficult to distinguish between the load oscillation effect and rotor asymmetry faults. On the contrary, this approach relieves the FFT spectral leakage phenomenon in some extent since the modulation frequency component appears far from the fundamental in the instantaneous power spectrum.

2.8 Load Fault Detection by Time-Frequency Analysis

This research work [21]-[22] introduces several signal processing methods in stator current fault signature analysis. Theoretical development using MMF wave approach in this research claims that a periodic load oscillation results in a sinusoidal phase modulation in a stator current component. The modulated stator current can be expressed in a general form by,

$$I(t) = i_{st}(t) + i_{rt}(t) = I_{st} sin(\omega_s t + \varphi_s) + I_{rt} sin(\omega_s t + \beta cos(\omega_c t)) \tag{2.18}$$

where ω_c is the load oscillation characteristic frequency in rad/s, the parameter β is called modulation index and φ_s is the initial phase difference between the rotor and stator MMFs. The term $i_{st}(t)$ resulting from the stator MMF is not modulated. However, the term $i_{rt}(t)$ which is closely related to the rotor MMF shows a phase modulation due to the considered load torque oscillation. The value of β is zero for a constant load condition. In the presence of a load oscillation, the stator current signal is no longer strictly stationary since the frequency of $i_{rt}(t)$ is varying sinusoidally with time.

The classical power spectrum density (PSD) method represents the basic signal analysis tool for stationary signals in frequency domain. It gives a first indication of a

possible load oscillation related mechanical fault by an increase of side-band harmonics at $f_s \pm f_c$. Since PSD may lead to an ambiguity between load fault and inherent rotor eccentricity, time-frequency spectrum analysis tools including instantaneous frequency (IF) estimation and Pseudo Wigner Distribution (PWD) are proposed to achieve better detection capability of phase modulation in a transient, non-stationary signal.

The effect of rotor eccentricity fault on the stator current amplitude and phase modulation is only assessed on a purely dynamic eccentricity model, not a mixed eccentricity. The experimental load torque oscillation is implemented by mounting an unbalance disk on the shaft [22], which essentially creates an eccentricity in the airgap in addition to the load oscillation. In other words, both the rotor eccentricity and the load torque oscillation, which is imposed on the motor shaft, yield mechanical faults inside the motor. Therefore it is still questionable to differentiate rotor mechanical faults from normal industrial loads with position-dependent torque oscillating characteristics, such as reciprocating compressors. In addition, this technique needs a very high sampling frequency for time-frequency signal analysis and leads to a relatively heavy computational burden.

2.9 Chapter Summary

A comprehensive literature review on the existing techniques of separating load effects from rotor faults detection is summarized in this chapter. Their respective merits and drawbacks are analyzed as well. Although it is an important industrial concern in online condition monitoring of induction motors, it was felt that very little work has been done on the topic of effectively detecting rotor eccentricity faults in the presence of a load torque oscillation for both mains-fed and drive-connected induction motors. This

task should be achieved without dependence on the accurate estimate of motor parameters. This serves as the motivation and objective of the current research work.

CHAPTER 3

MAGNETIC FIELD ANALYSIS FOR ECCENTRIC MOTORS

3.1 Overview

It is well known that the effects of a purely static eccentricity are quantitatively similar to those caused by a stator asymmetry, and a purely dynamic eccentricity leads to effects similar to a rotor asymmetry [32]-[33]. In practice, both types of eccentricities tend to coexist because there is always an inherent level of static or dynamic eccentricity even in a newly commissioned machine due to the manufacturing and assembly imperfectness.

3.2 Purely Rotor Static Eccentricity

An elementary 2-pole, 3-phase induction motor with sinusoidal winding distributions on both stator phases and equivalent rotor phases is modeled to evaluate the effect of a purely static eccentricity. For the purpose of clarity, and without loss of generality, space and time harmonics in the induced MMFs, stator and rotor slotting effects, and magnetic saturation effects are all neglected in the model. Under these assumptions, it is easy to understand that there is only fundamental component in supply currents.

For a purely static eccentricity, the first order approximation of the inverse air-gap length can be expressed as [24]-[26],

$$g^{-1}(\phi_s) = a_0 + a_1 \cos(\phi_s - \alpha) \tag{3.1}$$

where ϕ_s is the mechanical angular measure around the stator inner periphery, a_0 is the inverse of the average effective airgap length, $a_0 = 1/g_0$, and a_1 is termed as the static eccentricity permeance factor,

$$a_1 = \frac{2\left(1-\sqrt{1-\delta_s^2}\right)}{\delta_s\sqrt{1-\delta_s^2}} \tag{3.2}$$

where δ_s represents the degree of static eccentricity. That is, δ_s is ratio of the distance between the center of rotation and the center of the stator bore, to the nominal airgap length. Detailed Fourier series analysis has shown that, at a 40% degree of static eccentricity, the second harmonic coefficient of the Fourier series produced by the inversion of the airgap length is only 20% of the first harmonic coefficient [23]. It also shows that the first harmonic coefficient has a magnitude of 0.4554 on a normalized basis in this case. Therefore, equation (3.1) gives a very reasonable approximation of the inversion of the airgap length for a purely static eccentricity. The angle α in (3.2) denotes the relative position between the motor fault and stator magnetic axis as shown in Figure 3.1.

3.2.1 Modified Stator and Rotor MMFs

Assuming a sinusoidal winding distribution, the 3-phase stator winding distributions can be written as [37],

$$\begin{aligned}
N_{as}(\phi_s) &= -\frac{N_s}{2}\sin(\phi_s), && -\pi \le \phi_s \le 0 \\
N_{bs}(\phi_s) &= -\frac{N_s}{2}\sin\left(\phi_s - \frac{2\pi}{3}\right), && -\frac{\pi}{3} \le \phi_s \le \frac{2\pi}{3} \\
N_{cs}(\phi_s) &= -\frac{N_s}{2}\sin\left(\phi_s - \frac{4\pi}{3}\right), && \frac{\pi}{3} \le \phi_s \le \frac{4\pi}{3}
\end{aligned} \tag{3.3}$$

where N_s is the total number of turns per stator phase. Based on (3.3), the turns functions for 3-phase stator windings have the following form,

$$\begin{aligned} n_{as}(\phi_s) &= \frac{N_s}{2}\left[\cos(\phi_s)+1\right] \\ n_{bs}(\phi_s) &= \frac{N_s}{2}\left[\cos\left(\phi_s-\frac{2\pi}{3}\right)+1\right] \\ n_{cs}(\phi_s) &= \frac{N_s}{2}\left[\cos\left(\phi_s-\frac{4\pi}{3}\right)+1\right] \end{aligned} \tag{3.4}$$

For a healthy motor with constant airgap length, g_0, the MMF produced by a unit single phase stator winding current can be easily obtained by subtracting the average value of the turns function (dc offset) from itself. However, in the case of a rotor eccentricity, this method does not work since it does not satisfy the fundamental Gauss' Law. The following derivation for the modified MMFs in the presence of a purely static eccentricity is carried out in a similar way to [29]-[31] where it was originally derived for synchronous machines.

Considering a closed magnetic loop *abcda* in a 2-pole induction motor with purely static eccentricity and unit current excitation as shown in Figure 3.2, one can obtain the following expression from Ampere's Law,

$$\oint_{abcda} \vec{H}\cdot d\vec{l} = \int_S \vec{J}\cdot d\vec{S} \tag{3.5}$$

or

$$MMF(0)+MMF(\phi_s) = n(\phi_s) \tag{3.6}$$

where the permeability in both stator and rotor iron cores is assumed to be infinite and there is no MMF drop along the magnetic paths inside irons. In addition, all magnetic field quantities are assumed to have only radial components and remain constant along each radial direction. The fundamental Gauss' Law says that,

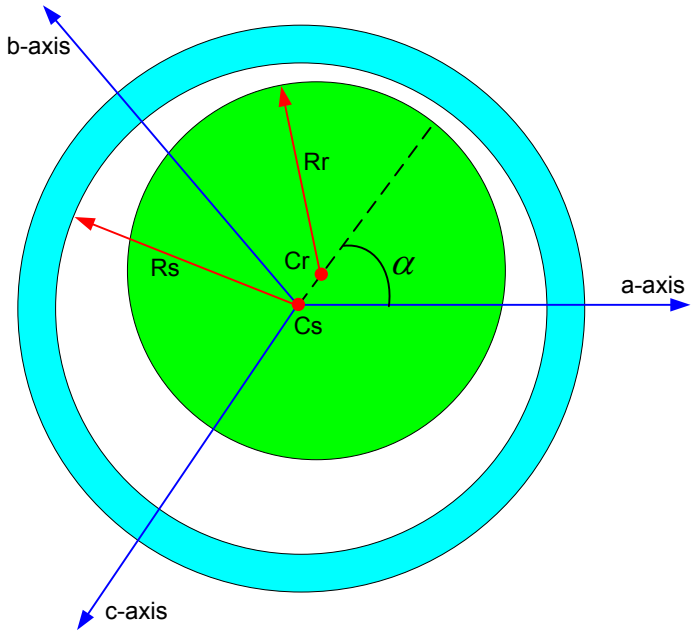

Figure 3.1 Static air-gap eccentricity.
Cs is the center of stator and Cr is the center of rotor.
Rs is the stator inner radius and Rr is the rotor outer radius.

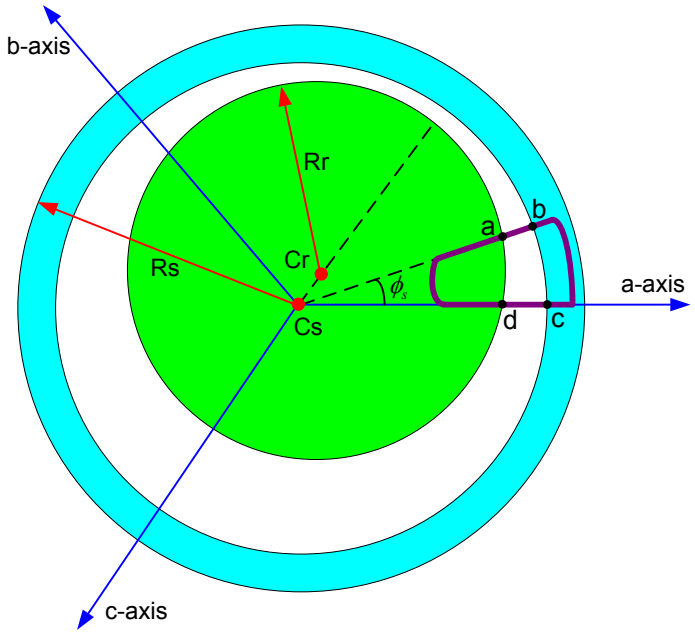

Figure 3.2 An elementary 2-pole induction machine with static eccentricity, showing a closed magnetic loop abcda.

$$\oint_S \vec{B}(\phi_s)\cdot d\vec{S} = 0 \tag{3.7}$$

where $\vec{B}(\phi_s)$ represents the radial magnetic field flux density in the airgap and the surface integral can be taken in a closed cylindrical surface just located outside the rotor outer periphery. Based on these assumptions, equation (3.7) can be rewritten as,

$$\int_0^{2\pi} \mu_0 \cdot MMF(\phi_s)\cdot g^{-1}(\phi_s)\cdot r\cdot l\cdot d\phi_s = 0 \tag{3.8}$$

or

$$\int_0^{2\pi} MMF(\phi_s)\cdot g^{-1}(\phi_s)\cdot d\phi_s = 0 \tag{3.9}$$

where μ_0 is the airgap permeability, r is the stator inner radius, and l is the axial stack length of the machine. Multiplying both sides of (3.6) by $g^{-1}(\phi_s)$ and integrating from 0 to 2π, one obtains,

$$\int_0^{2\pi} \left\{MMF(0)+MMF(\phi_s)\right\}\cdot g^{-1}(\phi_s)\cdot d\phi_s = \int_0^{2\pi} n(\phi_s)\cdot g^{-1}(\phi_s)\cdot d\phi_s \tag{3.10}$$

Substituting (3.9) into (3.10),

$$MMF(0) = \frac{\int_0^{2\pi} n(\phi_s)g^{-1}(\phi_s)d\phi_s}{\int_0^{2\pi} g^{-1}(\phi_s)d\phi_s} \tag{3.11}$$

Finally, from (3.6) and (3.11), the modified stator MMF can be expressed as,

$$MMF(\phi_s) = n(\phi_s) - \frac{\int_0^{2\pi} n(\phi_s)g^{-1}(\phi_s)d\phi_s}{\int_0^{2\pi} g^{-1}(\phi_s)d\phi_s} \tag{3.12}$$

Combining (3.1), (3.4) and (3.12) together, the modified 3-phase stator MMFs with a unit current excitation and a purely static eccentricity can be calculated as,

$$
\begin{aligned}
MMF_{as}(\phi_s) &= \frac{N_s}{2}\left[\cos(\phi_s) - \frac{\xi_s}{2}\cos(\alpha)\right] \\
MMF_{bs}(\phi_s) &= \frac{N_s}{2}\left[\cos\left(\phi_s - \frac{2\pi}{3}\right) - \frac{\xi_s}{2}\cos(\alpha - \frac{2\pi}{3})\right] \\
MMF_{cs}(\phi_s) &= \frac{N_s}{2}\left[\cos\left(\phi_s - \frac{4\pi}{3}\right) - \frac{\xi_s}{2}\cos(\alpha - \frac{4\pi}{3})\right]
\end{aligned} \tag{3.13}
$$

where $\xi_s = a_1/a_0$ is the static eccentricity coefficient. Similarly, the modified equivalent 3-phase rotor MMFs under the same conditions can be calculated as,

$$
\begin{aligned}
MMF_{ar}(\phi_r,\, \theta_r) &= \frac{N_r}{2}\left[\cos(\phi_r) - \frac{\xi_s}{2}\cos(\alpha - \theta_r)\right] \\
MMF_{br}(\phi_r,\, \theta_r) &= \frac{N_r}{2}\left[\cos\left(\phi_r - \frac{2\pi}{3}\right) - \frac{\xi_s}{2}\cos(\alpha - \theta_r - \frac{2\pi}{3})\right] \\
MMF_{cr}(\phi_r,\, \theta_r) &= \frac{N_r}{2}\left[\cos\left(\phi_r - \frac{4\pi}{3}\right) - \frac{\xi_s}{2}\cos(\alpha - \theta_r - \frac{4\pi}{3})\right]
\end{aligned} \tag{3.14}
$$

where N_r is the total number of turns per equivalent rotor phase, ϕ_r is the mechanical angular measure around the rotor outer periphery, and θ_r is the mechanical angular displacement between the stator a-phase magnetic axis and rotor A-phase magnetic axis. Note that, in order to obtain (3.14), the well known transformation between ϕ_s and ϕ_r, $\phi_s = \phi_r + \theta_r$, has to be applied into the calculation.

3.2.2 Motor Inductance Reformulation

Based on these modified stator and rotor MMFs, all kinds of machine inductances including stator self and mutual inductances, rotor self and mutual inductances, and stator to rotor mutual inductances are calculated using the regular double integral method [34]. For instance,

$$L_{asas} = L_{ls} + \int_{-\pi}^{0} N_{as}(\phi_s)\left\{\int_{\phi_s}^{\phi_s+\pi} \mu_0 \cdot r \cdot l \cdot MMF_{as}(\xi)\cdot g^{-1}(\xi)\cdot d\xi\right\} d\phi_s \tag{3.15}$$

All other machine inductances can be calculated in a similar way. Assuming the equivalent rotor phase has the same number of turns as the stator phase, $N_s = N_r$, one can further simplify the final inductance matrix expressions using the following preset symbols,

$$L_{ms} = \left(\frac{N_s}{2}\right)^2 \pi\mu_0 rla_0 = \left(\frac{N_s}{2}\right)\cdot\left(\frac{N_r}{2}\right)\pi\mu_0 rla_0 \tag{3.16}$$

Therefore, the stator self inductance matrix, stator to rotor mutual inductance matrix and rotor self inductance matrix can be expressed as,

$$\left[L_{ss}\right]_{static} = \begin{bmatrix} L_{ls} & 0 & 0 \\ 0 & L_{ls} & 0 \\ 0 & 0 & L_{ls} \end{bmatrix} + L_{ms}\cdot\begin{bmatrix} 1 & -\frac{1}{2} & -\frac{1}{2} \\ -\frac{1}{2} & 1 & -\frac{1}{2} \\ -\frac{1}{2} & -\frac{1}{2} & 1 \end{bmatrix} \tag{3.17}$$

$$-\frac{\xi_s^2}{2}L_{ms}\cdot\begin{bmatrix} \cos(\alpha)\cos(\alpha) & \cos(\alpha-\frac{2\pi}{3})\cos(\alpha) & \cos(\alpha-\frac{4\pi}{3})\cos(\alpha) \\ \cos(\alpha)\cos(\alpha-\frac{2\pi}{3}) & \cos(\alpha-\frac{2\pi}{3})\cos(\alpha-\frac{2\pi}{3}) & \cos(\alpha-\frac{4\pi}{3})\cos(\alpha-\frac{2\pi}{3}) \\ \cos(\alpha)\cos(\alpha-\frac{4\pi}{3}) & \cos(\alpha-\frac{2\pi}{3})\cos(\alpha-\frac{4\pi}{3}) & \cos(\alpha-\frac{4\pi}{3})\cos(\alpha-\frac{4\pi}{3}) \end{bmatrix}$$

$$\left[L_{sr}\right]_{static} = \left[L_{rs}\right]^{T}_{static} = L_{ms} \cdot \begin{bmatrix} \cos(\theta_r) & \cos(\theta_r + \frac{2\pi}{3}) & \cos(\theta_r + \frac{4\pi}{3}) \\ \cos(\theta_r + \frac{4\pi}{3}) & \cos(\theta_r) & \cos(\theta_r + \frac{2\pi}{3}) \\ \cos(\theta_r + \frac{2\pi}{3}) & \cos(\theta_r + \frac{4\pi}{3}) & \cos(\theta_r) \end{bmatrix} \tag{3.18}$$

$$-\frac{\xi_s^2}{2} L_{ms} \cdot \begin{bmatrix} \cos(\alpha)\cos(\alpha-\theta_r) & \cos(\alpha)\cos(\alpha-\theta_r-\frac{2\pi}{3}) & \cos(\alpha)\cos(\alpha-\theta_r-\frac{4\pi}{3}) \\ \cos(\alpha-\frac{2\pi}{3})\cos(\alpha-\theta_r) & \cos(\alpha-\frac{2\pi}{3})\cos(\alpha-\theta_r-\frac{2\pi}{3}) & \cos(\alpha-\frac{2\pi}{3})\cos(\alpha-\theta_r-\frac{4\pi}{3}) \\ \cos(\alpha-\frac{4\pi}{3})\cos(\alpha-\theta_r) & \cos(\alpha-\frac{4\pi}{3})\cos(\alpha-\theta_r-\frac{2\pi}{3}) & \cos(\alpha-\frac{4\pi}{3})\cos(\alpha-\theta_r-\frac{4\pi}{3}) \end{bmatrix}$$

$$\left[L_{rr}\right]_{static} = \begin{bmatrix} L_{lr} & 0 & 0 \\ 0 & L_{lr} & 0 \\ 0 & 0 & L_{lr} \end{bmatrix} + L_{ms} \cdot \begin{bmatrix} 1 & -\frac{1}{2} & -\frac{1}{2} \\ -\frac{1}{2} & 1 & -\frac{1}{2} \\ -\frac{1}{2} & -\frac{1}{2} & 1 \end{bmatrix} \tag{3.19}$$

$$-\frac{\xi_s^2}{2} L_{ms} \cdot \begin{bmatrix} \cos(\alpha-\theta_r)\cos(\alpha-\theta_r) & \cos(\alpha-\theta_r-\frac{2\pi}{3})\cos(\alpha-\theta_r) & \cos(\alpha-\theta_r-\frac{4\pi}{3})\cos(\alpha-\theta_r) \\ \cos(\alpha-\theta_r)\cos(\alpha-\theta_r-\frac{2\pi}{3}) & \cos(\alpha-\theta_r-\frac{2\pi}{3})\cos(\alpha-\theta_r-\frac{2\pi}{3}) & \cos(\alpha-\theta_r-\frac{4\pi}{3})\cos(\alpha-\theta_r-\frac{2\pi}{3}) \\ \cos(\alpha-\theta_r)\cos(\alpha-\theta_r-\frac{4\pi}{3}) & \cos(\alpha-\theta_r-\frac{2\pi}{3})\cos(\alpha-\theta_r-\frac{4\pi}{3}) & \cos(\alpha-\theta_r-\frac{4\pi}{3})\cos(\alpha-\theta_r-\frac{4\pi}{3}) \end{bmatrix}$$

The derivatives of these motor inductances are given below and will be used in Chapter 5 for dynamic simulation of the motor performance under fault conditions.

$$\frac{d\left[L_{ss}\right]_{static}}{d\theta_r} = \begin{bmatrix} 0 & 0 & 0 \\ 0 & 0 & 0 \\ 0 & 0 & 0 \end{bmatrix} \tag{3.20}$$

$$\frac{d\left[L_{sr}\right]_{static}}{d\theta_r} = \frac{d\left[L_{rs}\right]_{static}^{T}}{d\theta_r} = -L_{ms}\begin{bmatrix} \sin(\theta_r) & \sin(\theta_r+\frac{2\pi}{3}) & \sin(\theta_r+\frac{4\pi}{3}) \\ \sin(\theta_r+\frac{4\pi}{3}) & \sin(\theta_r) & \sin(\theta_r+\frac{2\pi}{3}) \\ \sin(\theta_r+\frac{2\pi}{3}) & \sin(\theta_r+\frac{4\pi}{3}) & \sin(\theta_r) \end{bmatrix} \tag{3.21}$$

$$-\frac{\xi_s^2}{2}L_{ms}\cdot\begin{bmatrix} \cos(\alpha)\sin(\alpha-\theta_r) & \cos(\alpha)\sin(\alpha-\theta_r-\frac{2\pi}{3}) & \cos(\alpha)\sin(\alpha-\theta_r-\frac{4\pi}{3}) \\ \cos(\alpha-\frac{2\pi}{3})\sin(\alpha-\theta_r) & \cos(\alpha-\frac{2\pi}{3})\sin(\alpha-\theta_r-\frac{2\pi}{3}) & \cos(\alpha-\frac{2\pi}{3})\sin(\alpha-\theta_r-\frac{4\pi}{3}) \\ \cos(\alpha-\frac{4\pi}{3})\sin(\alpha-\theta_r) & \cos(\alpha-\frac{4\pi}{3})\sin(\alpha-\theta_r-\frac{2\pi}{3}) & \cos(\alpha-\frac{4\pi}{3})\sin(\alpha-\theta_r-\frac{4\pi}{3}) \end{bmatrix}$$

$$\frac{d\left[L_{rr}\right]_{static}}{d\theta_r} = -\frac{\xi_s^2}{2}L_{ms}\cdot\begin{bmatrix} \sin(2\alpha-2\theta_r) & \sin(2\alpha-2\theta_r-\frac{2\pi}{3}) & \sin(2\alpha-2\theta_r-\frac{4\pi}{3}) \\ \sin(2\alpha-2\theta_r-\frac{2\pi}{3}) & \sin(2\alpha-2\theta_r-\frac{4\pi}{3}) & \sin(2\alpha-2\theta_r) \\ \sin(2\alpha-2\theta_r-\frac{4\pi}{3}) & \sin(2\alpha-2\theta_r) & \sin(2\alpha-2\theta_r-\frac{2\pi}{3}) \end{bmatrix} \tag{3.22}$$

3.2.3 Motor Current Characteristics

It is clear to see that the first rows in (3.17), (3.18) and (3.19) are just the regular inductance matrices for a healthy induction motor. However, due to the existence of a purely static eccentricity, additional inductance matrices are introduced into $\left[L_{ss}\right]_{static}$, $\left[L_{sr}\right]_{static}$, and $\left[L_{rr}\right]_{static}$.

Careful analysis of these inductance matrices provides some insight into the understanding of the motor operating characteristics under a fault condition. Obviously, the diagonal elements of $\left[L_{ss}\right]_{static}$ are no longer equal, even though $\left[L_{ss}\right]_{static}$ is still symmetric and constant. It is the parameter unbalance in the inductance matrices that introduces negative sequence information into motor terminal quantities for an eccentric case. In addition, the degree of motor asymmetry is closely related to the degree of rotor

eccentricity. Therefore, the higher the degree of eccentricity; the larger the magnitude of the corresponding negative sequence components. Since the simplified induction motor model considers a sinusoidal input, only the fundamental component appears in the stator current spectrum.

3.3 Purely Dynamic Rotor Eccentricity

For a purely dynamic eccentricity, the first order approximation of the inverse airgap length can be expressed as,

$$g^{-1}(\phi_r) = a_0 + a_2 \cos(\phi_r - \beta) \tag{3.23}$$

3.3.1 Modified Stator and Rotor MMFs

Similar to the case of a static eccentricity, the modified 3-phase stator and rotor MMFs for a purely dynamic eccentricity have the following form,

$$\begin{aligned}
MMF_{as} &= (\frac{N_s}{2})[\cos(\phi_s) - \frac{\xi_d}{2}\cos(\theta_r + \beta)] \cdot i_{as} \\
MMF_{bs} &= (\frac{N_s}{2})[\cos(\phi_s - \frac{2\pi}{3}) - \frac{\xi_d}{2}\cos(\theta_r + \beta - \frac{2\pi}{3})] \cdot i_{bs} \\
MMF_{cs} &= (\frac{N_s}{2})[\cos(\phi_s - \frac{4\pi}{3}) - \frac{\xi_d}{2}\cos(\theta_r + \beta - \frac{4\pi}{3})] \cdot i_{cs}
\end{aligned} \tag{3.24}$$

where $\xi_d = a_2 / a_0$ is the dynamic eccentricity coefficient.

$$\begin{aligned}
MMF_{ar} &= (\frac{N_r}{2})[\cos(\phi_r) - \frac{\xi_d}{2}\cos(\beta)] \cdot i_{ar} \\
MMF_{br} &= (\frac{N_r}{2})[\cos(\phi_r - \frac{2\pi}{3}) - \frac{\xi_d}{2}\cos(\beta - \frac{2\pi}{3})] \cdot i_{br} \\
MMF_{cr} &= (\frac{N_r}{2})[\cos(\phi_r - \frac{4\pi}{3}) - \frac{\xi_d}{2}\cos(\beta - \frac{4\pi}{3})] \cdot i_{cr}
\end{aligned} \tag{3.25}$$

3.3.2 Motor Inductance Reformulation

All machine inductances as well as their derivatives for a purely dynamic eccentric motor can be expressed as follows,

$$\left[L_{ss}\right]_{dynamic} = \begin{bmatrix} L_{ls} & 0 & 0 \\ 0 & L_{ls} & 0 \\ 0 & 0 & L_{ls} \end{bmatrix} + L_{ms} \cdot \begin{bmatrix} 1 & -\frac{1}{2} & -\frac{1}{2} \\ -\frac{1}{2} & 1 & -\frac{1}{2} \\ -\frac{1}{2} & -\frac{1}{2} & 1 \end{bmatrix} \tag{3.26}$$

$$-\frac{\xi_d^2}{2} L_{ms} \cdot \begin{bmatrix} \cos(\theta_r+\beta)\cos(\theta_r+\beta) & \cos(\theta_r+\beta-\frac{2\pi}{3})\cos(\theta_r+\beta) & \cos(\theta_r+\beta-\frac{4\pi}{3})\cos(\theta_r+\beta) \\ \cos(\theta_r+\beta)\cos(\theta_r+\beta-\frac{2\pi}{3}) & \cos(\theta_r+\beta-\frac{2\pi}{3})\cos(\theta_r+\beta-\frac{2\pi}{3}) & \cos(\theta_r+\beta-\frac{4\pi}{3})\cos(\theta_r+\beta-\frac{2\pi}{3}) \\ \cos(\theta_r+\beta)\cos(\theta_r+\beta-\frac{4\pi}{3}) & \cos(\theta_r+\beta-\frac{2\pi}{3})\cos(\theta_r+\beta-\frac{4\pi}{3}) & \cos(\theta_r+\beta-\frac{4\pi}{3})\cos(\theta_r+\beta-\frac{4\pi}{3}) \end{bmatrix}$$

$$\left[L_{sr}\right]_{dynamic} = \left[L_{rs}\right]_{dynamic}^{T} = L_{ms} \cdot \begin{bmatrix} \cos(\theta_r) & \cos(\theta_r+\frac{2\pi}{3}) & \cos(\theta_r+\frac{4\pi}{3}) \\ \cos(\theta_r+\frac{4\pi}{3}) & \cos(\theta_r) & \cos(\theta_r+\frac{2\pi}{3}) \\ \cos(\theta_r+\frac{2\pi}{3}) & \cos(\theta_r+\frac{4\pi}{3}) & \cos(\theta_r) \end{bmatrix} \tag{3.27}$$

$$-\frac{\xi_d^2}{2} L_{ms} \cdot \begin{bmatrix} \cos(\theta_r+\beta)\cos(\beta) & \cos(\theta_r+\beta)\cos(\beta-\frac{2\pi}{3}) & \cos(\theta_r+\beta)\cos(\beta-\frac{4\pi}{3}) \\ \cos(\theta_r+\beta-\frac{2\pi}{3})\cos(\beta) & \cos(\theta_r+\beta-\frac{2\pi}{3})\cos(\beta-\frac{2\pi}{3}) & \cos(\theta_r+\beta-\frac{2\pi}{3})\cos(\beta-\frac{4\pi}{3}) \\ \cos(\theta_r+\beta-\frac{4\pi}{3})\cos(\beta) & \cos(\theta_r+\beta-\frac{4\pi}{3})\cos(\beta-\frac{2\pi}{3}) & \cos(\theta_r+\beta-\frac{4\pi}{3})\cos(\beta-\frac{4\pi}{3}) \end{bmatrix}$$

$$\left[L_{rr}\right]_{dynamic}=\begin{bmatrix} L_{lr} & 0 & 0 \\ 0 & L_{lr} & 0 \\ 0 & 0 & L_{lr} \end{bmatrix}+L_{ms}\cdot\begin{bmatrix} 1 & -\frac{1}{2} & -\frac{1}{2} \\ -\frac{1}{2} & 1 & -\frac{1}{2} \\ -\frac{1}{2} & -\frac{1}{2} & 1 \end{bmatrix} \tag{3.28}$$

$$-\frac{\xi_d^2}{2}L_{ms}\cdot\begin{bmatrix} \cos(\beta)\cos(\beta) & \cos(\beta-\frac{2\pi}{3})\cos(\beta) & \cos(\beta-\frac{4\pi}{3})\cos(\beta) \\ \cos(\beta)\cos(\beta-\frac{2\pi}{3}) & \cos(\beta-\frac{2\pi}{3})\cos(\beta-\frac{2\pi}{3}) & \cos(\beta-\frac{4\pi}{3})\cos(\beta-\frac{2\pi}{3}) \\ \cos(\beta)\cos(\beta-\frac{4\pi}{3}) & \cos(\beta-\frac{2\pi}{3})\cos(\beta-\frac{4\pi}{3}) & \cos(\beta-\frac{4\pi}{3})\cos(\beta-\frac{4\pi}{3}) \end{bmatrix}$$

$$\frac{d\left[L_{ss}\right]_{dynamic}}{d\theta_r}=\frac{\xi_d^2}{2}L_{ms}\cdot\begin{bmatrix} \sin(2\theta_r+2\beta) & \sin(2\theta_r+2\beta-\frac{2\pi}{3}) & \sin(2\theta_r+2\beta-\frac{4\pi}{3}) \\ \sin(2\theta_r+2\beta-\frac{2\pi}{3}) & \sin(2\theta_r+2\beta-\frac{4\pi}{3}) & \sin(2\theta_r+2\beta) \\ \sin(2\theta_r+2\beta-\frac{4\pi}{3}) & \sin(2\theta_r+2\beta) & \sin(2\theta_r+2\beta-\frac{2\pi}{3}) \end{bmatrix} \tag{3.29}$$

$$\frac{d\left[L_{sr}\right]_{dynamic}}{d\theta_r}=\frac{d\left[L_{rs}\right]_{dynamic}^{T}}{d\theta_r}=-L_{ms}\begin{bmatrix} \sin(\theta_r) & \sin(\theta_r+\frac{2\pi}{3}) & \sin(\theta_r+\frac{4\pi}{3}) \\ \sin(\theta_r+\frac{4\pi}{3}) & \sin(\theta_r) & \sin(\theta_r+\frac{2\pi}{3}) \\ \sin(\theta_r+\frac{2\pi}{3}) & \sin(\theta_r+\frac{4\pi}{3}) & \sin(\theta_r) \end{bmatrix} \tag{3.30}$$

$$+\frac{\xi_d^2}{2}L_{ms}\cdot\begin{bmatrix} \sin(\theta_r+\beta)\cos(\beta) & \sin(\theta_r+\beta)\cos(\beta-\frac{2\pi}{3}) & \sin(\theta_r+\beta)\cos(\beta-\frac{4\pi}{3}) \\ \sin(\theta_r+\beta-\frac{2\pi}{3})\cos(\beta) & \sin(\theta_r+\beta-\frac{2\pi}{3})\cos(\beta-\frac{2\pi}{3}) & \sin(\theta_r+\beta-\frac{2\pi}{3})\cos(\beta-\frac{4\pi}{3}) \\ \sin(\theta_r+\beta-\frac{4\pi}{3})\cos(\beta) & \sin(\theta_r+\beta-\frac{4\pi}{3})\cos(\beta-\frac{2\pi}{3}) & \sin(\theta_r+\beta-\frac{4\pi}{3})\cos(\beta-\frac{4\pi}{3}) \end{bmatrix}$$

$$\frac{d\left[L_{rr}\right]_{dynamic}}{d\theta_r}=\begin{bmatrix} 0 & 0 & 0 \\ 0 & 0 & 0 \\ 0 & 0 & 0 \end{bmatrix} \tag{3.31}$$

3.3.3 Motor Current Characteristics

Again, the first rows in (3.26), (3.27) and (3.28) are just the regular inductance matrices for a healthy induction motor. However, due to the existence of a purely dynamic eccentricity, additional inductance matrices are introduced into $[L_{ss}]_{dynamic}$, $[L_{sr}]_{dynamic}$, and $[L_{rr}]_{dynamic}$. A purely dynamic eccentricity does not introduce negative sequence information into stator currents since the center of rotation is still located at the center of the stator bore. The airgap permeance modulation by the dynamic eccentricity produces some sideband harmonics into the stator currents.

3.4 Mixed Rotor Eccentricity

The first order approximation of the inverse airgap length for a mixed rotor eccentricity can be expressed as [24]-[26],

$$g^{-1}(\phi_s, \phi_r) = a_0 + a_1 \cos(\phi_s - \alpha) + a_2 \cos(\phi_r - \beta) \tag{3.32}$$

where $\phi_s = \phi_r + \theta_r$.

3.4.1 Modified Stator and Rotor MMFs

The modified 3-phase stator and rotor MMFs for a mixed rotor eccentricity are basically the summation of those for a purely static eccentricity and a purely dynamic eccentricity,

$$\begin{aligned}
MMF_{as} &= (\frac{N_s}{2})[\cos(\phi_s) - \frac{\xi_s}{2}\cos(\alpha) - \frac{\xi_d}{2}\cos(\theta_r + \beta)] \cdot i_{as} \\
MMF_{bs} &= (\frac{N_s}{2})[\cos(\phi_s - \frac{2\pi}{3}) - \frac{\xi_s}{2}\cos(\alpha - \frac{2\pi}{3}) - \frac{\xi_d}{2}\cos(\theta_r + \beta - \frac{2\pi}{3})] \cdot i_{bs} \\
MMF_{cs} &= (\frac{N_s}{2})[\cos(\phi_s - \frac{4\pi}{3}) - \frac{\xi_s}{2}\cos(\alpha - \frac{4\pi}{3}) - \frac{\xi_d}{2}\cos(\theta_r + \beta - \frac{4\pi}{3})] \cdot i_{bs}
\end{aligned} \tag{3.33}$$

$$
\begin{aligned}
MMF_{ar} &= (\frac{N_r}{2})[\cos(\phi_r) - \frac{\xi_s}{2}\cos(\alpha - \theta_r) - \frac{\xi_d}{2}\cos(\beta)] \cdot i_{ar} \\
MMF_{br} &= (\frac{N_r}{2})[\cos(\phi_r - \frac{2\pi}{3}) - \frac{\xi_s}{2}\cos(\alpha - \theta_r - \frac{2\pi}{3}) - \frac{\xi_d}{2}\cos(\beta - \frac{2\pi}{3})] \cdot i_{br} \\
MMF_{cr} &= (\frac{N_r}{2})[\cos(\phi_r - \frac{4\pi}{3}) - \frac{\xi_s}{2}\cos(\alpha - \theta_r - \frac{4\pi}{3}) - \frac{\xi_d}{2}\cos(\beta - \frac{4\pi}{3})] \cdot i_{cr}
\end{aligned}
\tag{3.34}
$$

3.4.2 Motor Inductance Reformulation

Machine inductance matrices for a mixed rotor eccentricity are even more complex since there is an interaction between the modified MMFs and airgap permeance modulation for different types of eccentricities. In other words, the modified MMF component from a purely static eccentricity interacts with the permeance modulation component from a purely dynamic eccentricity, and vice versa. All inductance matrices and their corresponding derivatives for a mixed rotor eccentricity, which are listed in the following pages, have a close relationship with those for a purely static or dynamic eccentricity. By setting $\xi_s = 0$ or $\xi_d = 0$, machine inductances for a mixed rotor eccentricity become those for a purely static or dynamic eccentricity.

$$\left[L_{ss}\right]_{mixed} = \begin{bmatrix} L_{ls} & 0 & 0 \\ 0 & L_{ls} & 0 \\ 0 & 0 & L_{ls} \end{bmatrix} + L_{ms} \cdot \begin{bmatrix} 1 & -\frac{1}{2} & -\frac{1}{2} \\ -\frac{1}{2} & 1 & -\frac{1}{2} \\ -\frac{1}{2} & -\frac{1}{2} & 1 \end{bmatrix} \tag{3.35}$$

$$-\frac{\xi_s^2}{2} L_{ms} \cdot \begin{bmatrix} \cos(\alpha)\cos(\alpha) & \cos(\alpha-\frac{2\pi}{3})\cos(\alpha) & \cos(\alpha-\frac{4\pi}{3})\cos(\alpha) \\ \cos(\alpha)\cos(\alpha-\frac{2\pi}{3}) & \cos(\alpha-\frac{2\pi}{3})\cos(\alpha-\frac{2\pi}{3}) & \cos(\alpha-\frac{4\pi}{3})\cos(\alpha-\frac{2\pi}{3}) \\ \cos(\alpha)\cos(\alpha-\frac{4\pi}{3}) & \cos(\alpha-\frac{2\pi}{3})\cos(\alpha-\frac{4\pi}{3}) & \cos(\alpha-\frac{4\pi}{3})\cos(\alpha-\frac{4\pi}{3}) \end{bmatrix}$$

$$-\frac{\xi_d^2}{2} L_{ms} \cdot \begin{bmatrix} \cos(\theta_r+\beta)\cos(\theta_r+\beta) & \cos(\theta_r+\beta-\frac{2\pi}{3})\cos(\theta_r+\beta) & \cos(\theta_r+\beta-\frac{4\pi}{3})\cos(\theta_r+\beta) \\ \cos(\theta_r+\beta)\cos(\theta_r+\beta-\frac{2\pi}{3}) & \cos(\theta_r+\beta-\frac{2\pi}{3})\cos(\theta_r+\beta-\frac{2\pi}{3}) & \cos(\theta_r+\beta-\frac{4\pi}{3})\cos(\theta_r+\beta-\frac{2\pi}{3}) \\ \cos(\theta_r+\beta)\cos(\theta_r+\beta-\frac{4\pi}{3}) & \cos(\theta_r+\beta-\frac{2\pi}{3})\cos(\theta_r+\beta-\frac{4\pi}{3}) & \cos(\theta_r+\beta-\frac{4\pi}{3})\cos(\theta_r+\beta-\frac{4\pi}{3}) \end{bmatrix}$$

$$-\frac{\xi_s \cdot \xi_d}{2} L_{ms} \cdot \begin{bmatrix} \cos(\alpha)\cos(\theta_r+\beta) & \cos(\alpha-\frac{2\pi}{3})\cos(\theta_r+\beta) & \cos(\alpha-\frac{4\pi}{3})\cos(\theta_r+\beta) \\ \cos(\alpha)\cos(\theta_r+\beta-\frac{2\pi}{3}) & \cos(\alpha-\frac{2\pi}{3})\cos(\theta_r+\beta-\frac{2\pi}{3}) & \cos(\alpha-\frac{4\pi}{3})\cos(\theta_r+\beta-\frac{2\pi}{3}) \\ \cos(\alpha)\cos(\theta_r+\beta-\frac{4\pi}{3}) & \cos(\alpha-\frac{2\pi}{3})\cos(\theta_r+\beta-\frac{4\pi}{3}) & \cos(\alpha-\frac{4\pi}{3})\cos(\theta_r+\beta-\frac{4\pi}{3}) \end{bmatrix}$$

$$-\frac{\xi_s \cdot \xi_d}{2} L_{ms} \cdot \begin{bmatrix} \cos(\alpha)\cos(\theta_r+\beta) & \cos(\alpha)\cos(\theta_r+\beta-\frac{2\pi}{3}) & \cos(\alpha)\cos(\theta_r+\beta-\frac{4\pi}{3}) \\ \cos(\alpha-\frac{2\pi}{3})\cos(\theta_r+\beta) & \cos(\alpha-\frac{2\pi}{3})\cos(\theta_r+\beta-\frac{2\pi}{3}) & \cos(\alpha-\frac{2\pi}{3})\cos(\theta_r+\beta-\frac{4\pi}{3}) \\ \cos(\alpha-\frac{4\pi}{3})\cos(\theta_r+\beta) & \cos(\alpha-\frac{4\pi}{3})\cos(\theta_r+\beta-\frac{2\pi}{3}) & \cos(\alpha-\frac{4\pi}{3})\cos(\theta_r+\beta-\frac{4\pi}{3}) \end{bmatrix}$$

$$\left[L_{sr}\right]_{mixed} = \left[L_{rs}\right]^{T}_{mixed} = L_{ms} \cdot \begin{bmatrix} \cos(\theta_r) & \cos(\theta_r + \frac{2\pi}{3}) & \cos(\theta_r + \frac{4\pi}{3}) \\ \cos(\theta_r + \frac{4\pi}{3}) & \cos(\theta_r) & \cos(\theta_r + \frac{2\pi}{3}) \\ \cos(\theta_r + \frac{2\pi}{3}) & \cos(\theta_r + \frac{4\pi}{3}) & \cos(\theta_r) \end{bmatrix} \tag{3.36}$$

$$-\frac{\xi_s^2}{2} L_{ms} \cdot \begin{bmatrix} \cos(\alpha)\cos(\alpha - \theta_r) & \cos(\alpha)\cos(\alpha - \theta_r - \frac{2\pi}{3}) & \cos(\alpha)\cos(\alpha - \theta_r - \frac{4\pi}{3}) \\ \cos(\alpha - \frac{2\pi}{3})\cos(\alpha - \theta_r) & \cos(\alpha - \frac{2\pi}{3})\cos(\alpha - \theta_r - \frac{2\pi}{3}) & \cos(\alpha - \frac{2\pi}{3})\cos(\alpha - \theta_r - \frac{4\pi}{3}) \\ \cos(\alpha - \frac{4\pi}{3})\cos(\alpha - \theta_r) & \cos(\alpha - \frac{4\pi}{3})\cos(\alpha - \theta_r - \frac{2\pi}{3}) & \cos(\alpha - \frac{4\pi}{3})\cos(\alpha - \theta_r - \frac{4\pi}{3}) \end{bmatrix}$$

$$-\frac{\xi_d^2}{2} L_{ms} \cdot \begin{bmatrix} \cos(\theta_r + \beta)\cos(\beta) & \cos(\theta_r + \beta)\cos(\beta - \frac{2\pi}{3}) & \cos(\theta_r + \beta)\cos(\beta - \frac{4\pi}{3}) \\ \cos(\theta_r + \beta - \frac{2\pi}{3})\cos(\beta) & \cos(\theta_r + \beta - \frac{2\pi}{3})\cos(\beta - \frac{2\pi}{3}) & \cos(\theta_r + \beta - \frac{2\pi}{3})\cos(\beta - \frac{4\pi}{3}) \\ \cos(\theta_r + \beta - \frac{4\pi}{3})\cos(\beta) & \cos(\theta_r + \beta - \frac{4\pi}{3})\cos(\beta - \frac{2\pi}{3}) & \cos(\theta_r + \beta - \frac{4\pi}{3})\cos(\beta - \frac{4\pi}{3}) \end{bmatrix}$$

$$-\frac{\xi_s \cdot \xi_d}{2} L_{ms} \cdot \begin{bmatrix} \cos(\alpha - \theta_r)\cos(\theta_r + \beta) & \cos(\alpha - \theta_r - \frac{2\pi}{3})\cos(\theta_r + \beta) & \cos(\alpha - \theta_r - \frac{4\pi}{3})\cos(\theta_r + \beta) \\ \cos(\alpha - \theta_r)\cos(\theta_r + \beta - \frac{2\pi}{3}) & \cos(\alpha - \theta_r - \frac{2\pi}{3})\cos(\theta_r + \beta - \frac{2\pi}{3}) & \cos(\alpha - \theta_r - \frac{4\pi}{3})\cos(\theta_r + \beta - \frac{2\pi}{3}) \\ \cos(\alpha - \theta_r)\cos(\theta_r + \beta - \frac{4\pi}{3}) & \cos(\alpha - \theta_r - \frac{2\pi}{3})\cos(\theta_r + \beta - \frac{4\pi}{3}) & \cos(\alpha - \theta_r - \frac{4\pi}{3})\cos(\theta_r + \beta - \frac{4\pi}{3}) \end{bmatrix}$$

$$-\frac{\xi_s \cdot \xi_d}{2} L_{ms} \cdot \begin{bmatrix} \cos(\alpha)\cos(\beta) & \cos(\alpha)\cos(\beta - \frac{2\pi}{3}) & \cos(\alpha)\cos(\beta - \frac{4\pi}{3}) \\ \cos(\alpha - \frac{2\pi}{3})\cos(\beta) & \cos(\alpha - \frac{2\pi}{3})\cos(\beta - \frac{2\pi}{3}) & \cos(\alpha - \frac{2\pi}{3})\cos(\beta - \frac{4\pi}{3}) \\ \cos(\alpha - \frac{4\pi}{3})\cos(\beta) & \cos(\alpha - \frac{4\pi}{3})\cos(\beta - \frac{2\pi}{3}) & \cos(\alpha - \frac{4\pi}{3})\cos(\beta - \frac{4\pi}{3}) \end{bmatrix}$$

$$\left[L_{rr}\right]_{mixed}=\begin{bmatrix} L_{lr} & 0 & 0 \\ 0 & L_{lr} & 0 \\ 0 & 0 & L_{lr} \end{bmatrix}+L_{ms}\cdot\begin{bmatrix} 1 & -\frac{1}{2} & -\frac{1}{2} \\ -\frac{1}{2} & 1 & -\frac{1}{2} \\ -\frac{1}{2} & -\frac{1}{2} & 1 \end{bmatrix} \tag{3.37}$$

$$-\frac{\xi_s^2}{2}L_{ms}\cdot\begin{bmatrix} \cos(\alpha-\theta_r)\cos(\alpha-\theta_r) & \cos(\alpha-\theta_r-\frac{2\pi}{3})\cos(\alpha-\theta_r) & \cos(\alpha-\theta_r-\frac{4\pi}{3})\cos(\alpha-\theta_r) \\ \cos(\alpha-\theta_r)\cos(\alpha-\theta_r-\frac{2\pi}{3}) & \cos(\alpha-\theta_r-\frac{2\pi}{3})\cos(\alpha-\theta_r-\frac{2\pi}{3}) & \cos(\alpha-\theta_r-\frac{4\pi}{3})\cos(\alpha-\theta_r-\frac{2\pi}{3}) \\ \cos(\alpha-\theta_r)\cos(\alpha-\theta_r-\frac{4\pi}{3}) & \cos(\alpha-\theta_r-\frac{2\pi}{3})\cos(\alpha-\theta_r-\frac{4\pi}{3}) & \cos(\alpha-\theta_r-\frac{4\pi}{3})\cos(\alpha-\theta_r-\frac{4\pi}{3}) \end{bmatrix}$$

$$-\frac{\xi_d^2}{2}L_{ms}\cdot\begin{bmatrix} \cos(\beta)\cos(\beta) & \cos(\beta-\frac{2\pi}{3})\cos(\beta) & \cos(\beta-\frac{4\pi}{3})\cos(\beta) \\ \cos(\beta)\cos(\beta-\frac{2\pi}{3}) & \cos(\beta-\frac{2\pi}{3})\cos(\beta-\frac{2\pi}{3}) & \cos(\beta-\frac{4\pi}{3})\cos(\beta-\frac{2\pi}{3}) \\ \cos(\beta)\cos(\beta-\frac{4\pi}{3}) & \cos(\beta-\frac{2\pi}{3})\cos(\beta-\frac{4\pi}{3}) & \cos(\beta-\frac{4\pi}{3})\cos(\beta-\frac{4\pi}{3}) \end{bmatrix}$$

$$-\frac{\xi_s\cdot\xi_d}{2}L_{ms}\cdot\begin{bmatrix} \cos(\alpha-\theta_r)\cos(\beta) & \cos(\alpha-\theta_r-\frac{2\pi}{3})\cos(\beta) & \cos(\alpha-\theta_r-\frac{4\pi}{3})\cos(\beta) \\ \cos(\alpha-\theta_r)\cos(\beta-\frac{2\pi}{3}) & \cos(\alpha-\theta_r-\frac{2\pi}{3})\cos(\beta-\frac{2\pi}{3}) & \cos(\alpha-\theta_r-\frac{4\pi}{3})\cos(\beta-\frac{2\pi}{3}) \\ \cos(\alpha-\theta_r)\cos(\beta-\frac{4\pi}{3}) & \cos(\alpha-\theta_r-\frac{2\pi}{3})\cos(\beta-\frac{4\pi}{3}) & \cos(\alpha-\theta_r-\frac{4\pi}{3})\cos(\beta-\frac{4\pi}{3}) \end{bmatrix}$$

$$-\frac{\xi_s\cdot\xi_d}{2}L_{ms}\cdot\begin{bmatrix} \cos(\alpha-\theta_r)\cos(\beta) & \cos(\alpha-\theta_r)\cos(\beta-\frac{2\pi}{3}) & \cos(\alpha-\theta_r)\cos(\beta-\frac{4\pi}{3}) \\ \cos(\alpha-\theta_r-\frac{2\pi}{3})\cos(\beta) & \cos(\alpha-\theta_r-\frac{2\pi}{3})\cos(\beta-\frac{2\pi}{3}) & \cos(\alpha-\theta_r-\frac{2\pi}{3})\cos(\beta-\frac{4\pi}{3}) \\ \cos(\alpha-\theta_r-\frac{4\pi}{3})\cos(\beta) & \cos(\alpha-\theta_r-\frac{4\pi}{3})\cos(\beta-\frac{2\pi}{3}) & \cos(\alpha-\theta_r-\frac{4\pi}{3})\cos(\beta-\frac{4\pi}{3}) \end{bmatrix}$$

$$\frac{d\left[L_{ss}\right]_{mixed}}{d\theta_r} = \begin{bmatrix} 0 & 0 & 0 \\ 0 & 0 & 0 \\ 0 & 0 & 0 \end{bmatrix} \tag{3.38}$$

$$+ \begin{bmatrix} 0 & 0 & 0 \\ 0 & 0 & 0 \\ 0 & 0 & 0 \end{bmatrix}$$

$$+ \frac{\xi_d^2}{2} L_{ms} \cdot \begin{bmatrix} \sin(2\theta_r + 2\beta) & \sin(2\theta_r + 2\beta - \frac{2\pi}{3}) & \sin(2\theta_r + 2\beta - \frac{4\pi}{3}) \\ \sin(2\theta_r + 2\beta - \frac{2\pi}{3}) & \sin(2\theta_r + 2\beta - \frac{4\pi}{3}) & \sin(2\theta_r + 2\beta) \\ \sin(2\theta_r + 2\beta - \frac{4\pi}{3}) & \sin(2\theta_r + 2\beta) & \sin(2\theta_r + 2\beta - \frac{2\pi}{3}) \end{bmatrix}$$

$$+ \frac{\xi_s \cdot \xi_d}{2} L_{ms} \cdot \begin{bmatrix} \cos(\alpha)\sin(\theta_r + \beta) & \cos(\alpha - \frac{2\pi}{3})\sin(\theta_r + \beta) & \cos(\alpha - \frac{4\pi}{3})\sin(\theta_r + \beta) \\ \cos(\alpha)\sin(\theta_r + \beta - \frac{2\pi}{3}) & \cos(\alpha - \frac{2\pi}{3})\sin(\theta_r + \beta - \frac{2\pi}{3}) & \cos(\alpha - \frac{4\pi}{3})\sin(\theta_r + \beta - \frac{2\pi}{3}) \\ \cos(\alpha)\sin(\theta_r + \beta - \frac{4\pi}{3}) & \cos(\alpha - \frac{2\pi}{3})\sin(\theta_r + \beta - \frac{4\pi}{3}) & \cos(\alpha - \frac{4\pi}{3})\sin(\theta_r + \beta - \frac{4\pi}{3}) \end{bmatrix}$$

$$+ \frac{\xi_s \cdot \xi_d}{2} L_{ms} \cdot \begin{bmatrix} \cos(\alpha)\sin(\theta_r + \beta) & \cos(\alpha)\sin(\theta_r + \beta - \frac{2\pi}{3}) & \cos(\alpha)\sin(\theta_r + \beta - \frac{4\pi}{3}) \\ \cos(\alpha - \frac{2\pi}{3})\sin(\theta_r + \beta) & \cos(\alpha - \frac{2\pi}{3})\sin(\theta_r + \beta - \frac{2\pi}{3}) & \cos(\alpha - \frac{2\pi}{3})\sin(\theta_r + \beta - \frac{4\pi}{3}) \\ \cos(\alpha - \frac{4\pi}{3})\sin(\theta_r + \beta) & \cos(\alpha - \frac{4\pi}{3})\sin(\theta_r + \beta - \frac{2\pi}{3}) & \cos(\alpha - \frac{4\pi}{3})\sin(\theta_r + \beta - \frac{4\pi}{3}) \end{bmatrix}$$

$$\frac{d\left[L_{sr}\right]_{mixed}}{d\theta_r} = \frac{d\left[L_{rs}\right]_{mixed}^{T}}{d\theta_r} = -L_{ms} \cdot \begin{bmatrix} \sin(\theta_r) & \sin(\theta_r + \frac{2\pi}{3}) & \sin(\theta_r + \frac{4\pi}{3}) \\ \sin(\theta_r + \frac{4\pi}{3}) & \sin(\theta_r) & \sin(\theta_r + \frac{2\pi}{3}) \\ \sin(\theta_r + \frac{2\pi}{3}) & \sin(\theta_r + \frac{4\pi}{3}) & \sin(\theta_r) \end{bmatrix} \tag{3.39}$$

$$-\frac{\xi_s^2}{2} L_{ms} \cdot \begin{bmatrix} \cos(\alpha)\sin(\alpha - \theta_r) & \cos(\alpha)\sin(\alpha - \theta_r - \frac{2\pi}{3}) & \cos(\alpha)\sin(\alpha - \theta_r - \frac{4\pi}{3}) \\ \cos(\alpha - \frac{2\pi}{3})\sin(\alpha - \theta_r) & \cos(\alpha - \frac{2\pi}{3})\sin(\alpha - \theta_r - \frac{2\pi}{3}) & \cos(\alpha - \frac{2\pi}{3})\sin(\alpha - \theta_r - \frac{4\pi}{3}) \\ \cos(\alpha - \frac{4\pi}{3})\sin(\alpha - \theta_r) & \cos(\alpha - \frac{4\pi}{3})\sin(\alpha - \theta_r - \frac{2\pi}{3}) & \cos(\alpha - \frac{4\pi}{3})\sin(\alpha - \theta_r - \frac{4\pi}{3}) \end{bmatrix}$$

$$+\frac{\xi_d^2}{2} L_{ms} \cdot \begin{bmatrix} \sin(\theta_r + \beta)\cos(\beta) & \sin(\theta_r + \beta)\cos(\beta - \frac{2\pi}{3}) & \sin(\theta_r + \beta)\cos(\beta - \frac{4\pi}{3}) \\ \sin(\theta_r + \beta - \frac{2\pi}{3})\cos(\beta) & \sin(\theta_r + \beta - \frac{2\pi}{3})\cos(\beta - \frac{2\pi}{3}) & \sin(\theta_r + \beta - \frac{2\pi}{3})\cos(\beta - \frac{4\pi}{3}) \\ \sin(\theta_r + \beta - \frac{4\pi}{3})\cos(\beta) & \sin(\theta_r + \beta - \frac{4\pi}{3})\cos(\beta - \frac{2\pi}{3}) & \sin(\theta_r + \beta - \frac{4\pi}{3})\cos(\beta - \frac{4\pi}{3}) \end{bmatrix}$$

$$-\frac{\xi_s \cdot \xi_d}{2} L_{ms} \cdot \begin{bmatrix} \sin(\alpha - \beta - 2\theta_r) & \sin(\alpha - \beta - 2\theta_r - \frac{2\pi}{3}) & \sin(\alpha - \beta - 2\theta_r - \frac{4\pi}{3}) \\ \sin(\alpha - \beta - 2\theta_r - \frac{4\pi}{3}) & \sin(\alpha - \beta - 2\theta_r) & \sin(\alpha - \beta - 2\theta_r - \frac{2\pi}{3}) \\ \sin(\alpha - \beta - 2\theta_r - \frac{2\pi}{3}) & \sin(\alpha - \beta - 2\theta_r - \frac{4\pi}{3}) & \sin(\alpha - \beta - 2\theta_r) \end{bmatrix}$$

$$+\begin{bmatrix} 0 & 0 & 0 \\ 0 & 0 & 0 \\ 0 & 0 & 0 \end{bmatrix}$$

$$\frac{d\left[L_{rr}\right]_{mixed}}{d\theta_r}=\begin{bmatrix}0&0&0\\0&0&0\\0&0&0\end{bmatrix} \tag{3.40}$$

$$-\frac{\xi_s^2}{2}L_{ms}\cdot\begin{bmatrix}\sin(2\alpha-2\theta_r) & \sin(2\alpha-2\theta_r-\frac{2\pi}{3}) & \sin(2\alpha-2\theta_r-\frac{4\pi}{3})\\ \sin(2\alpha-2\theta_r-\frac{2\pi}{3}) & \sin(2\alpha-2\theta_r-\frac{4\pi}{3}) & \sin(2\alpha-2\theta_r)\\ \sin(2\alpha-2\theta_r-\frac{4\pi}{3}) & \sin(2\alpha-2\theta_r) & \sin(2\alpha-2\theta_r-\frac{2\pi}{3})\end{bmatrix}$$

$$+\begin{bmatrix}0&0&0\\0&0&0\\0&0&0\end{bmatrix}$$

$$+\frac{\xi_s\cdot\xi_d}{2}L_{ms}\cdot\begin{bmatrix}\sin(\alpha-\theta_r)\cos(\beta) & \sin(\alpha-\theta_r-\frac{2\pi}{3})\cos(\beta) & \sin(\alpha-\theta_r-\frac{4\pi}{3})\cos(\beta)\\ \sin(\alpha-\theta_r)\cos(\beta-\frac{2\pi}{3}) & \sin(\alpha-\theta_r-\frac{2\pi}{3})\cos(\beta-\frac{2\pi}{3}) & \sin(\alpha-\theta_r-\frac{4\pi}{3})\cos(\beta-\frac{2\pi}{3})\\ \sin(\alpha-\theta_r)\cos(\beta-\frac{4\pi}{3}) & \sin(\alpha-\theta_r-\frac{2\pi}{3})\cos(\beta-\frac{4\pi}{3}) & \sin(\alpha-\theta_r-\frac{4\pi}{3})\cos(\beta-\frac{4\pi}{3})\end{bmatrix}$$

$$+\frac{\xi_s\cdot\xi_d}{2}L_{ms}\cdot\begin{bmatrix}\sin(\alpha-\theta_r)\cos(\beta) & \sin(\alpha-\theta_r)\cos(\beta-\frac{2\pi}{3}) & \sin(\alpha-\theta_r)\cos(\beta-\frac{4\pi}{3})\\ \sin(\alpha-\theta_r-\frac{2\pi}{3})\cos(\beta) & \sin(\alpha-\theta_r-\frac{2\pi}{3})\cos(\beta-\frac{2\pi}{3}) & \sin(\alpha-\theta_r-\frac{2\pi}{3})\cos(\beta-\frac{4\pi}{3})\\ \sin(\alpha-\theta_r-\frac{4\pi}{3})\cos(\beta) & \sin(\alpha-\theta_r-\frac{4\pi}{3})\cos(\beta-\frac{2\pi}{3}) & \sin(\alpha-\theta_r-\frac{4\pi}{3})\cos(\beta-\frac{4\pi}{3})\end{bmatrix}$$

3.4.3 Motor Current Characteristics

Mixed rotor eccentricities also introduce parameter unbalance in the motor, as shown in (3.35). Since the machine inductance matrices for a mixed rotor eccentricity inherit the characteristics from both purely static and dynamic eccentricities, negative sequence information at side-band harmonics, which is referred to the *negative sequence harmonic information*, is expected to appear in supply currents. This rotor eccentricity characteristic information serves as the new, proposed eccentricity fault indicator for a mains-fed induction motor in the presence of a load torque oscillation.

The motor asymmetry induced by a rotor eccentricity also yields a negative sequence component at the fundamental in the supply currents. However, this negative sequence fundamental information is dominated by the inevitable unbalanced power supply for a mains-fed machine. Therefore, only negative sequence harmonic information, which is exempt from the unbalance power supply, should be properly monitored to decouple the load oscillating effects from the rotor eccentricity detection.

3.5 Motor Current Characteristics for a Load Oscillation

Ideally, a position dependent load torque oscillation produces only positive sequence information (fundamental and sideband harmonics) in the stator currents, considering the motor and shaft are not impacted by this type of load variation. However, there is always an inherent level of machine unbalance during the manufacturing and assembly stage. In addition, instrumentation imperfections, such as the current and voltage transducer scaling ratio mismatch, also affect the measurement accuracy. Hence, the normalized negative sequence harmonic information with respect to its positive sequence counterpart

in a mains-fed machine serves as the most reliable indicator to accurately evaluate the increased motor asymmetry level, which is solely caused by a rotor eccentricity fault.

3.6 Chapter Summary

In this chapter, a detailed airgap magnetic field analysis for a purely static eccentricity, a purely dynamic eccentricity and a mixed rotor eccentricity is performed to derive the modified three phase stator and rotor MMFs for each case.

After that, all machine inductances as well as their derivatives are reformulated by applying the classical double-integration method. It is important to point out here, although these modified inductance matrices are derived for a 2-pole model, they are well suited for a multi-pole motor by including a multiplier of machine pole-pair numbers. These eccentricity reformulated impedance matrices are further compared with those caused by a stator inter-turn fault in Chapter 6.

Finally, motor current characteristics corresponding to each type of rotor eccentricity as well as a position dependent load torque oscillation are discussed to provide an insight on distinguishing load torque oscillation from rotor eccentricity faults.

CHAPTER 4

EXTRACTING NEGATIVE SEQUENCE HARMONIC INFORMATION

4.1 Overview

In this Chapter, a new FFT technique is developed to effectively extract negative sequence harmonic information from the three phase currents. The proposed method overcomes the shortcoming in the traditional symmetrical component decomposition method, which can only separate sequence components at the fundamental or its multiples. It also has several advantages over the reference frame transformation method to effectively separate harmonic sequence components. This new technique is important to achieve reliable rotor eccentricity fault detection under arbitrary load conditions. In addition, it also eases the extraction of fundamental per-phase sequence components from phase-phase voltage measurements in many online condition monitoring applications.

4.2 Traditional Symmetrical Component Decomposition

Symmetrical components are most commonly used for analysis of three-phase electrical power systems [35]. If the phase quantities are expressed in phasor notation using complex numbers, a vector can be formed for the three phase quantities. For example, a vector for three phase currents could be written as,

$$\overline{I}_{abc} = \begin{bmatrix} \tilde{I}_a \\ \tilde{I}_b \\ \tilde{I}_c \end{bmatrix} \tag{4.1}$$

and the three symmetrical components phasors arranged into a vector as,

$$\overline{I}_{sym} = \begin{bmatrix} \tilde{I}_p \\ \tilde{I}_n \\ \tilde{I}_z \end{bmatrix} \tag{4.2}$$

where the subscripts p, q, and z refer respectively to the positive, negative, and zero sequence components. A phase rotation operator a is defined to rotate a phasor vector forward by 120 degrees or $\frac{2}{3}\pi$ radians,

$$a = e^{j120^\circ} = e^{j\frac{2}{3}\pi} \tag{4.3}$$

A matrix A can be defined using this operator to transform the phase vector into symmetrical components,

$$\overline{I}_{sym} = \begin{bmatrix} \tilde{I}_p \\ \tilde{I}_n \\ \tilde{I}_z \end{bmatrix} = \frac{1}{3} \cdot A \cdot \tilde{I}_{abc} = \frac{1}{3} \cdot \begin{bmatrix} 1 & a & a^2 \\ 1 & a^2 & a \\ 1 & 1 & 1 \end{bmatrix} \cdot \begin{bmatrix} \tilde{I}_a \\ \tilde{I}_b \\ \tilde{I}_c \end{bmatrix} \tag{4.4}$$

The traditional symmetrical components decomposition method may only separate positive and negative sequence components at fundamental or its multiples, not at characteristic harmonic frequencies, since three phase phasors can be accurately constructed from measurements only at the fundamental or its multiples. For an inverter-fed motor with varying excitation frequency, this method may not work even at the fundamental if the FFT spectrum resolution is not sufficiently high. Therefore, this scheme is not suitable to extract negative sequence harmonic information for the purpose of online condition monitoring.

4.3 Rotating Reference Frame Transformation Method

It is also possible to distinguish negative sequence characteristic harmonics from their positive sequence counterparts by performing DQ transformation in a newly selected rotating reference frame [56]-[57].

In general, the most dominant characteristic harmonics resulting from a rotor eccentricity or load torque oscillation correspond to the case $k=1$ in (1.2) or (1.6). Therefore, one only needs to consider the largest two harmonics in the stator current spectrum,

$$f_{ecc}^{L} = f_e - f_{rm} \quad \text{and} \quad f_{ecc}^{H} = f_e + f_{rm} \tag{4.5}$$

where superscript L denotes the lower harmonic and superscript H indicates the higher one. There are both positive and negative sequence components existing at f_{ecc}^{L} as well as f_{ecc}^{H} in three phase currents.

One can just focus on a single characteristic harmonic, e.g. f_{ecc}^{H}. The three phase current harmonics at this single frequency can then be expressed as,

$$\begin{aligned} i_a &= I_1\cos(\omega_{ecc}^{H}t+\varphi_1) + I_2\cos(\omega_{ecc}^{H}t+\varphi_2) \\ i_b &= I_1\cos(\omega_{ecc}^{H}t+\varphi_1-120^\circ) + I_2\cos(\omega_{ecc}^{H}t+\varphi_2+120^\circ) \\ i_c &= I_1\cos(\omega_{ecc}^{H}t+\varphi_1-240^\circ) + I_2\cos(\omega_{ecc}^{H}t+\varphi_2+240^\circ) \end{aligned} \tag{4.6}$$

where I_1, I_2, φ_1 and φ_2 represent the magnitudes and initial phase angles for the positive and negative sequence harmonic components at ω_{ecc}^{H}, respectively. Equation (4.6) can be also written as,

$$\begin{aligned} i_a &= I_1\cos(\omega_{ecc}^{H}t+\varphi_1) + I_2\cos(-\omega_{ecc}^{H}t+\varphi_3) \\ i_b &= I_1\cos(\omega_{ecc}^{H}t+\varphi_1-120^\circ) + I_2\cos(-\omega_{ecc}^{H}t+\varphi_3-120^\circ) \\ i_c &= I_1\cos(\omega_{ecc}^{H}t+\varphi_1-240^\circ) + I_2\cos(-\omega_{ecc}^{H}t+\varphi_3-240^\circ) \end{aligned} \tag{4.7}$$

where $\varphi_3 = -\varphi_2$. It is interesting to observe that, the negative sequence component at frequency ω_{ecc}^H is actually equivalent to the positive sequence component at the counter frequency $-\omega_{ecc}^H$. Hence, the terms of "negative sequence" and "counter frequency" can be used interchangeably. Note that, similar to the concept of positive/negative sequence components, the notion of counter frequency here is only meaningful to three phase quantities.

One can further transform the three phase characteristic harmonics at f_{ecc}^H into dq-axis components in a newly selected rotating reference frame at $\omega = 2\pi f$,

$$\begin{bmatrix} i_q^f \\ i_d^f \end{bmatrix} = (\frac{2}{3}) \begin{bmatrix} \cos(\theta) & \cos(\theta - 120^\circ) & \cos(\theta - 240^\circ) \\ \sin(\theta) & \sin(\theta - 120^\circ) & \sin(\theta - 240^\circ) \end{bmatrix} * \begin{bmatrix} i_a \\ i_b \\ i_c \end{bmatrix} \tag{4.8}$$

where $\theta = \omega \cdot t$ is the transformation angle. Substituting (4.6) into (4.8) and applying proper trigonometric relations [34] to simplify the final equations, one obtains the dq-axis components as follows,

$$\begin{bmatrix} i_q^f \\ i_d^f \end{bmatrix} = \begin{bmatrix} I_1 \cos[(\omega - \omega_{ecc}^H)t - \varphi_1] + I_2 \cos[(\omega + \omega_{ecc}^H)t + \varphi_2] \\ I_1 \sin[(\omega - \omega_{ecc}^H)t - \varphi_1] + I_2 \sin[(\omega + \omega_{ecc}^H)t + \varphi_2] \end{bmatrix} \tag{4.9}$$

It is clear to see that, in the new rotating reference frame, the original positive sequence harmonic component at ω_{ecc}^H is shifted to $\left|\omega - \omega_{ecc}^H\right|$ and the corresponding negative sequence harmonic component is shifted to $\left|\omega + \omega_{ecc}^H\right|$.

For the purpose of illustrating sequence components decomposition in the new reference frame, space vectors corresponding to the positive and negative sequence harmonic components are shown in Figure 4.1, in the stationary and rotating reference frame, respectively.

Ideally, positive/negative sequence harmonic magnitudes should be equal in the i_q^f and i_d^f spectra. However, due to the limited FFT resolution and measurement noise, there is always a difference in the spectral analysis of i_q^f and i_d^f. Therefore, it becomes difficult to determine the exact magnitudes of the harmonic sequence components using this dq-transformation technique.

In addition, the shifted harmonic sequence components in the new reference frame might overlap with the sequence components from other non-characteristic harmonics. For example, if the three phase currents happen to contain harmonics at $f_{ecc}^H + 2f$, which has nothing to do with a rotor eccentricity or load oscillation, then the positive sequence component at this non-characteristic harmonic would interfere with the negative sequence component at f_{ecc}^H in the new reference frame rotating at f. Since these inherent non-characteristic harmonics vary from motor to motor, it is difficult to specify a uniform rotating reference frame to perform the dq-transformation and accurately extract positive and negative sequence characteristic harmonics.

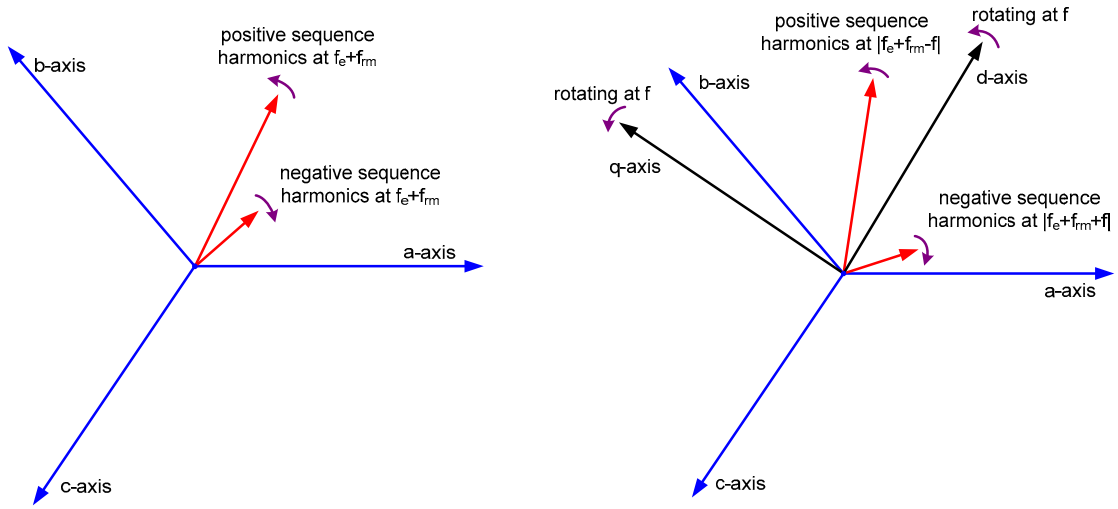

(a) (b)

Figure 4.1 Positive and negative sequence harmonic space vector in (a) stationary reference frame and (b) rotating reference frame

4.4 New FFT Technique to Separate Sequence Information

The conventional spectral analysis performs an FFT on a real number sequence, e.g. a single phase stator current with a sampling frequency f_s and total sampling time T sec, resulting in $N = T \cdot f_s$ samples in total. Again, one can consider only a single frequency characteristic harmonic in phase-a current,

$$i_a = I_1 \cdot \cos(\omega_{ecc} \cdot t + \varphi_1) + I_2 \cdot \cos(\omega_{ecc} \cdot t + \varphi_2) \tag{4.10}$$

or

$$i_a = I \cdot \cos(2\pi \cdot f_{ecc} \cdot t + \theta) \tag{4.11}$$

where the positive and negative sequence components at f_{ecc} are combined together in (4.11) with

$$I = \sqrt{\left[I_1 \cos(\varphi_1) + I_2 \cos(\varphi_2)\right]^2 + \left[I_1 \sin(\varphi_1) + I_2 \sin(\varphi_2)\right]^2} \tag{4.12}$$

$$\theta = \tan^{-1}\left\{\frac{I_1\sin(\varphi_1)+I_2\sin(\varphi_2)}{I_1\cos(\varphi_1)+I_2\cos(\varphi_2)}\right\} \tag{4.13}$$

Equation (4.11) can be further decomposed into two frequency components using Euler's formula, as

$$i_a = (\frac{I}{2})\cdot e^{j2\pi(f_{ecc})t}\cdot e^{j\theta} + (\frac{I}{2})\cdot e^{j2\pi(-f_{ecc})t}\cdot e^{j(-\theta)} \tag{4.14}$$

Therefore, FFT analysis of a real number sequence, $i_a[n]$, splits a single frequency quantity into two parts, f_{ecc} and $(-f_{ecc})$, in the spectrum. Each part shares half of the total magnitude at that frequency and takes opposite phase angle. Obviously, $(-f_{ecc})$ or $f_s - f_{ecc}$ component in $i_a[n]$ spectrum does not provide any additional information.

In order to effectively separate positive and negative sequence harmonic information, three phase harmonics can be constructed into a harmonic space vector in the stationary reference frame,

$$\vec{I}_{ecc} = \frac{2}{3}(i_a\cdot e^{j0^\circ} + i_b\cdot e^{j120^\circ} + i_c\cdot e^{j240^\circ}) \tag{4.15}$$

Similar to (4.14), each of i_a, i_b and i_c can be decomposed into four parts while considering positive and negative sequence components for a single phase separately,

$$\begin{aligned} i_a = {} & (\frac{I_1}{2})\cdot e^{j2\pi(f_{ecc})t}\cdot e^{j\varphi_1} + (\frac{I_1}{2})\cdot e^{j2\pi(-f_{ecc})t}\cdot e^{j(-\varphi_1)} \\ & + (\frac{I_2}{2})\cdot e^{j2\pi(f_{ecc})t}\cdot e^{j\varphi_2} + (\frac{I_2}{2})\cdot e^{j2\pi(-f_{ecc})t}\cdot e^{j(-\varphi_2)} \end{aligned} \tag{4.16}$$

$$\begin{aligned} i_b = {} & (\frac{I_1}{2})\cdot e^{j2\pi(f_{ecc})t}\cdot e^{j(\varphi_1-120^\circ)} + (\frac{I_1}{2})\cdot e^{j2\pi(-f_{ecc})t}\cdot e^{j(-\varphi_1+120^\circ)} \\ & + (\frac{I_2}{2})\cdot e^{j2\pi(f_{ecc})t}\cdot e^{j(\varphi_2+120^\circ)} + (\frac{I_2}{2})\cdot e^{j2\pi(-f_{ecc})t}\cdot e^{j(-\varphi_2-120^\circ)} \end{aligned} \tag{4.17}$$

$$i_c = (\frac{I_1}{2}) \cdot e^{j2\pi(f_{ecc})t} \cdot e^{j(\varphi_1 - 240^\circ)} + (\frac{I_1}{2}) \cdot e^{j2\pi(-f_{ecc})t} \cdot e^{j(-\varphi_1 + 240^\circ)} + (\frac{I_2}{2}) \cdot e^{j2\pi(f_{ecc})t} \cdot e^{j(\varphi_2 + 240^\circ)} + (\frac{I_2}{2}) \cdot e^{j2\pi(-f_{ecc})t} \cdot e^{j(-\varphi_2 - 240^\circ)} \quad (4.18)$$

Substituting (4.16)-(4.18) into (4.15), after a few steps of mathematical manipulation, one reaches a very simple expression for the stator current harmonic space vector,

$$\vec{I}_{ecc} = I_1 \cdot e^{j2\pi(f_{ecc})t} \cdot e^{j(\varphi_1)} + I_2 \cdot e^{j2\pi(-f_{ecc})t} \cdot e^{j(-\varphi_2)} \quad (4.19)$$

FFT analysis of the complex number sequence, $\vec{I}_{ecc}[n]$, splits the positive sequence harmonic magnitude, I_1, at the positive frequency, f_{ecc}, and the negative sequence harmonic magnitude, I_2, at the counter frequency, $(-f_{ecc})$ or $f_s - f_{ecc}$. Note that, the value of f_{ecc} can be either positive or negative depending on the selection of k in (1.2) or (1.6). In case the value of f_{ecc} is a negative number in (4.19), then I_1 appears at f_{ecc} or $f_s + f_{ecc}$ while I_2 appears at $(-f_{ecc})$. Therefore, negative sequence harmonic information is always reflected at the counter frequency component in $\vec{I}_{ecc}[n]$ spectrum.

Although the above mathematical derivation deals only with a single frequency characteristic harmonic, the proposed FFT technique can be easily extended to all frequency components by constructing a stator current space vector, which contains all frequency information, from three phase measurements,

$$\vec{I} = \frac{2}{3}(I_a \cdot e^{j0^\circ} + I_b \cdot e^{j120^\circ} + I_c \cdot e^{j240^\circ}) \quad (4.20)$$

By performing FFT to the complex number sequence, $\vec{I}[n]$, positive and negative sequence components can be conveniently separated at all available frequency indexes in the spectrum. In general, frequency resolution in FFT depends on the total sampling

time. In order to accurately locate the characteristic harmonics in $\vec{I}[n]$ spectrum, it is necessary to sample three phase quantities for a sufficiently long period.

For a four-pole induction motor, the negative sequence component corresponding to the characteristic harmonic, $f_{ecc}^{L} = f_e - f_{rm}$ (positive value), is located at $f_s - (f_e - f_{rm})$, while the positive sequence component corresponding to the characteristic harmonic $f_e - 3f_{rm}$ (negative value) is located at $f_s + (f_e - 3f_{rm})$. When the motor is running at light load conditions, these two components lie very close in the spectrum and may overlap with each other due to spectral leakage effects. Therefore, negative sequence information located at $-f_{ecc}^{H} = -(f_e + f_{rm})$ is a better rotor fault indicator to detect eccentricity induced motor asymmetry.

The proposed new FFT technique has significant advantage over the traditional method using symmetrical component decomposition. First, symmetrical component method requires construction of three phasors at a single frequency through regular FFT analysis for each phase. Due to the finite frequency resolution in FFT, these phasors can be reliably established only at fundamental and its multiples. For a specific characteristic harmonic f_{ecc}, the phase angle information calculated from FFT might be far away from its true value, leading to an inaccurate phasor construction and incredible symmetrical component decomposition. Second, the proposed technique extracts positive and negative sequence information at all frequency components simultaneously by executing the FFT on the space vector complex number sequence while the symmetrical component method performs the decomposition only for a single frequency quantity at each time.

4.5 Application for Phase-Phase Measurements

In many online condition monitoring applications, it often requires extracting fundamental sequence components from motor currents as well as motor voltages. For stator inter-turn fault detection, the impedance matrix is calculated from both current and voltage sequence components to evaluate the motor asymmetry level [46]-[49]. In order to accomplish an accurate estimation of motor efficiency or stator winding temperature [54], positive and negative sequence components in the terminal quantities need to be evaluated in the corresponding per-phase equivalent circuit model separately.

Different from the three phase current measurements, phase-neutral (assuming Y-connected stator winding) voltage measurements are usually inaccessible. Although phase-ground measurements produce exactly the same positive and negative sequence components as phase-neutral voltages [46], they are inconvenient in many cases. (Note that the only difference between phase-neutral and phase-ground measurements resides in their zero sequence components.) In general, only phase-phase voltage measurements are available for online motor condition monitoring.

The traditional procedure to obtain per-phase sequence components from phase-phase measurements is shown in Figure 4.2. First, FFT analysis of each phase-phase voltage yields a phasor at fundamental. After that, sequence components in phase-phase voltages are obtained by applying symmetrical component decomposition to all three phasors. Finally, per-phase sequence components can be derived from corresponding phase-phase sequence components as follows,

$$\tilde{V}^1_{phase} = \tilde{V}^1_{an} = \frac{1}{\sqrt{3}} \tilde{V}^1_{ab} \cdot e^{j(-30^\circ)} = \frac{1}{\sqrt{3}} \tilde{V}^1_{phase-phase} \cdot e^{j(-30^\circ)} \tag{4.21}$$

$$\tilde{V}^2_{phase} = \tilde{V}^2_{an} = \frac{1}{\sqrt{3}}\tilde{V}^2_{ab} \cdot e^{j30^\circ} = \frac{1}{\sqrt{3}}\tilde{V}^2_{phase-phase} \cdot e^{j30^\circ} \tag{4.22}$$

where superscripts 1 and 2 represent positive and negative sequence components respectively. These relationships are also drawn in Figure 4.3.

The proposed new FFT technique also simplifies the transformation procedure in Figure 4.2 to obtain fundamental per-phase sequence components easier and more accurately. This is done by applying the FFT directly to the constructed stator voltage space vector. The definition of a stator voltage space vector is based on phase-neutral voltages,

$$\vec{V} = \frac{2}{3}(V_{an} \cdot e^{j0^\circ} + V_{bn} \cdot e^{j120^\circ} + V_{cn} \cdot e^{j240^\circ}) \tag{4.23}$$

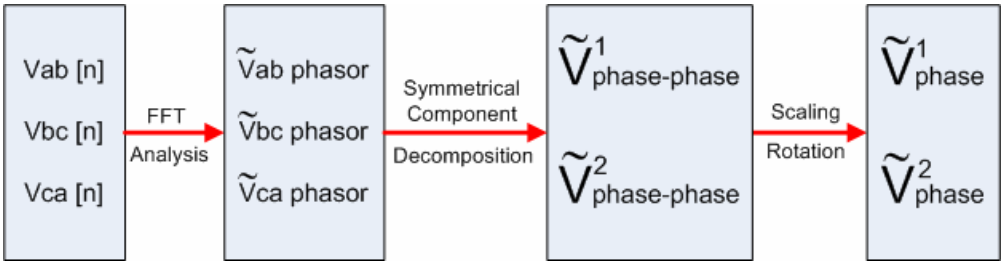

Figure 4.2 Procedure to obtain per phase sequence components from phase-phase measurements

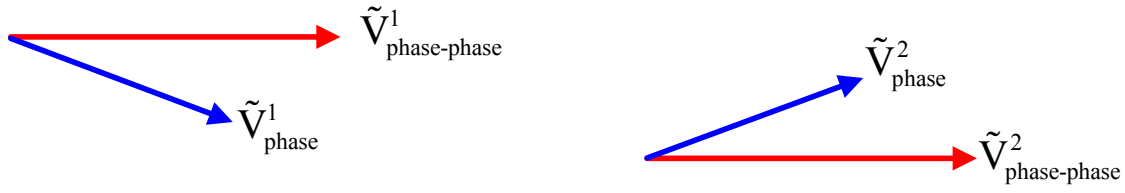

Figure 4.3 Relationship between sequence components from per-phase and phase-phase quantities

Considering the identity expression below,

$$0 = \frac{2}{3}(V_{cn} \cdot e^{j0^\circ} + V_{cn} \cdot e^{j120^\circ} + V_{cn} \cdot e^{j240^\circ}) \tag{4.24}$$

the desired stator voltage space vector can be easily constructed from the two phase-phase voltage measurements by subtracting (4.24) from (4.23) as follows,

$$\vec{V} = \frac{2}{3}(V_{ac} \cdot e^{j0^\circ} + V_{bc} \cdot e^{j120^\circ}) \tag{4.25}$$

The FFT of the stator voltage space vector immediately gives the per-phase positive sequence voltage at f_e and per-phase negative sequence voltage at $-f_e$ or $f_s - f_e$ in the spectrum.

For drive-connected induction motors, the stator excitation frequency is varying with respect to the reference speed and load level. In this case, it becomes even more difficult to extract fundamental sequence components in stator currents and voltages using symmetrical component decomposition. Phasors at the fundamental may not be accurately constructed for a varying excitation frequency due to the limited FFT resolution. Therefore, the proposed FFT technique shows great advantages in drive applications.

4.6 Chapter Summary

This Chapter presents an effective and computationally efficient strategy to extract negative sequence harmonic information from stator currents, which can be further applied in a reliable diagnostics of rotor eccentricity faults in the presence of a load torque oscillation. By applying the FFT to the stator current or the stator voltage space vector, this method can separate sequence components at all frequencies simultaneously. Therefore, the proposed technique has significant advantages over the traditional

symmetrical component decomposition method. In addition to rotor eccentricity detection, this technique can be applied in many other online condition monitoring areas such as stator turn fault detection, thermal estimation, and motor efficiency evaluation. This method is particularly useful for drive applications with a varying excitation frequency.

CHAPTER 5

DEVELOPMENT AND SIMULATION OF NEW ROTOR ECCENTRICITY FAULT INDICATORS

5.1 Overview

The new rotor eccentricity fault indicators in the presence of a load torque oscillation are developed for mains-fed and drive-connected induction motors, respectively, in this chapter. Either a simplified Matlab Simulink model or a complex Finite Element Analysis (FEA) can be applied to simulate induction motor dynamic performance. The Matlab model neglects the time and space harmonics in the induced MMFs. Magnetic saturation and slotting effects are also not considered. This model specifically focuses on the airgap permeance modulation caused by rotor eccentricities. On the other hand, FEA Model includes all above neglected factors and produces much more accurate results. However, it is extremely time-consuming to perform the transient analysis necessary to obtain a sufficiently high FFT spectral resolution.

5.2 A New Eccentricity Indicator in Mains-Fed Machines

A rotor position-dependent load torque oscillation at multiples of the rotational speed, such as in reciprocating compressors, introduces exactly the same harmonic components as a rotor eccentricity, in the single phase stator current spectrum. These load oscillation-related harmonics usually have a much larger magnitude and are likely to completely mask eccentricity-induced fault signatures. In order to achieve reliable

eccentricity fault detection in the presence of a load torque oscillation, some new eccentricity-only related information has to be detected.

Magnetic filed analysis shows that a rotor eccentricity introduces parameter unbalance inside the motor. On the contrary, in the case of a load torque oscillation, the motor itself is still balanced. Therefore, the additional motor asymmetry, caused solely by the rotor fault, represents the new eccentricity-only related information which should be examined as well, in online condition monitoring of induction motors.

In a mains-fed induction motor, motor asymmetry is completely reflected into the negative sequence components in stator currents. Due to the inevitable unbalance in supply voltages, the negative sequence information in fundamental currents is not a reliable rotor fault indicator. Thus it is necessary to properly monitor negative sequence characteristic harmonic information in three phase currents.

Considering the inherent motor unbalance and instrumentation imperfections, it is desirable to calculate the normalized negative sequence component at characteristic harmonics with respect to the corresponding positive sequence harmonic magnitude to accurately evaluate the increased motor asymmetry level caused by rotor eccentricities. Therefore, the additional rotor fault indicator for a mains-fed machine is

$$\delta = I^*_{n\_ecc} = \frac{I_{n\_ecc}}{I_{p\_ecc}} \tag{5.1}$$

where I_{n_ecc} denotes the magnitude of the negative sequence characteristic harmonic component, I_{p_ecc} denotes the corresponding positive sequence counterpart and the superscript $*$ represents the normalized value. To effectively eliminate load oscillation

effects, both the regular characteristic side-band harmonics as well as the proposed additional motor asymmetry indicator should be monitored simultaneously.

5.3 Matlab Simulation for a Mains-Fed Induction Motor

5.3.1 Induction Motor Dynamic Model

Airgap magnetic field analysis presented in Chapter 3 shows that rotor eccentricities introduce parameter unbalance in motor inductance matrices and negative sequence information is expected to appear in supply currents. For the time being, there is no confidence about the voltage level at the stator (and the equivalent rotor) winding neutral points. Consequently, dynamic simulation of a faulty motor is performed in the physical *ABC* system instead of using a qd-axis transformation. All simulation equations are concluded as follows,

$$\begin{bmatrix} v_{as}-v_{s\_n} \\ v_{bs}-v_{s\_n} \\ v_{cs}-v_{s\_n} \end{bmatrix} = \begin{bmatrix} r_s & 0 & 0 \\ 0 & r_s & 0 \\ 0 & 0 & r_s \end{bmatrix} \cdot \begin{bmatrix} i_{as} \\ i_{bs} \\ i_{cs} \end{bmatrix} + \frac{d}{dt} \begin{bmatrix} \lambda_{as} \\ \lambda_{bs} \\ \lambda_{cs} \end{bmatrix} \tag{5.2}$$

$$\begin{bmatrix} 0-v_{r\_n} \\ 0-v_{r\_n} \\ 0-v_{r\_n} \end{bmatrix} = \begin{bmatrix} r_r & 0 & 0 \\ 0 & r_r & 0 \\ 0 & 0 & r_r \end{bmatrix} \cdot \begin{bmatrix} i_{ar} \\ i_{br} \\ i_{cr} \end{bmatrix} + \frac{d}{dt} \begin{bmatrix} \lambda_{ar} \\ \lambda_{br} \\ \lambda_{cr} \end{bmatrix} \tag{5.3}$$

$$\begin{bmatrix} \lambda_{abcs} \\ \lambda_{abcr} \end{bmatrix} = \begin{bmatrix} [L_{ss}] & [L_{sr}] \\ [L_{sr}]^T & [L_{rr}] \end{bmatrix} . \begin{bmatrix} i_{abcs} \\ i_{abcr} \end{bmatrix} \tag{5.4}$$

$$\begin{aligned} i_{as} + i_{bs} + i_{cs} &= 0 \\ i_{ar} + i_{br} + i_{cr} &= 0 \end{aligned} \tag{5.5}$$

where r_s and r_r are the stator and rotor per phase resistance, v_{s_n} and v_{r_n} are the unknown stator and equivalent rotor neutral point voltages. All the inductance matrices in (5.4) have been reformulated for a purely static eccentricity, a purely dynamic eccentricity and a mixed rotor eccentricity, respectively. Note that three phase stator and rotor currents are forced to sum to zero in (5.5) during the dynamic simulation since there is no zero sequence component in either i_{abcs} or i_{abcr}.

The mechanical equation of motion depends on the load characteristics. It is assumed that, for simplicity, the load torque consists only of an inertial toque and its expression is explicitly known. Therefore, the mechanical equation is simply,

$$T_{em} - T_{load} = J_{eq} \cdot \frac{d\omega_{rm}}{dt} = J_{eq} \cdot \frac{d\omega_r}{dt} \tag{5.6}$$

for a 2-pole machine. The developed electromagnetic torque, T_{em}, can be obtained from the magnetic coenergy, W_{co}, as follows [30], [36]

$$T_{em} = \left.\frac{\partial W_{co}}{\partial \theta_{rm}}\right|_{\vec{I}_s, \vec{I}_r} = \left.\frac{\partial W_{co}}{\partial \theta_r}\right|_{\vec{I}_s, \vec{I}_r} \tag{5.7}$$

where $\vec{I}_s$ and $\vec{I}_r$ denote stator and rotor current vectors,

$$\begin{aligned} \vec{I}_s &= \begin{bmatrix} i_{as} & i_{bs} & i_{cs} \end{bmatrix}^T \\ \vec{I}_r &= \begin{bmatrix} i_{ar} & i_{br} & i_{cr} \end{bmatrix}^T \end{aligned} \tag{5.8}$$

In a linear magnetic system, the coenergy is equal to the stored magnetic energy,

$$W_{co} = \frac{1}{2} \cdot \begin{bmatrix} \vec{I}_s^T & \vec{I}_r^T \end{bmatrix} \cdot \begin{bmatrix} [L_{ss}] & [L_{sr}] \\ [L_{sr}]^T & [L_{rr}] \end{bmatrix} \cdot \begin{bmatrix} \vec{I}_s \\ \vec{I}_r \end{bmatrix} \tag{5.9}$$

Therefore, in the 2-pole machine model, T_{em} has the form of,

$$T_{em} = \frac{1}{2} \cdot \begin{bmatrix} \vec{I}_s^T & \vec{I}_r^T \end{bmatrix} \cdot \frac{d}{d\theta_r} \begin{bmatrix} [L_{ss}] & [L_{sr}] \\ [L_{sr}]^T & [L_{rr}] \end{bmatrix} \cdot \begin{bmatrix} \vec{I}_s \\ \vec{I}_r \end{bmatrix} \tag{5.10}$$

Note that in the case of rotor eccentricities, all inductance matrices shown in (5.4) and (5.10) vary as a function of θ_r due to the non-uniform airgap permeance modulation effects. Matlab Simulink model schematics using the reformulated machine inductances for a mains-fed machine are given in Figure 5.1. Motor parameters used to simulate the Matlab Simulink model are listed in Appendix A for readers' reference.

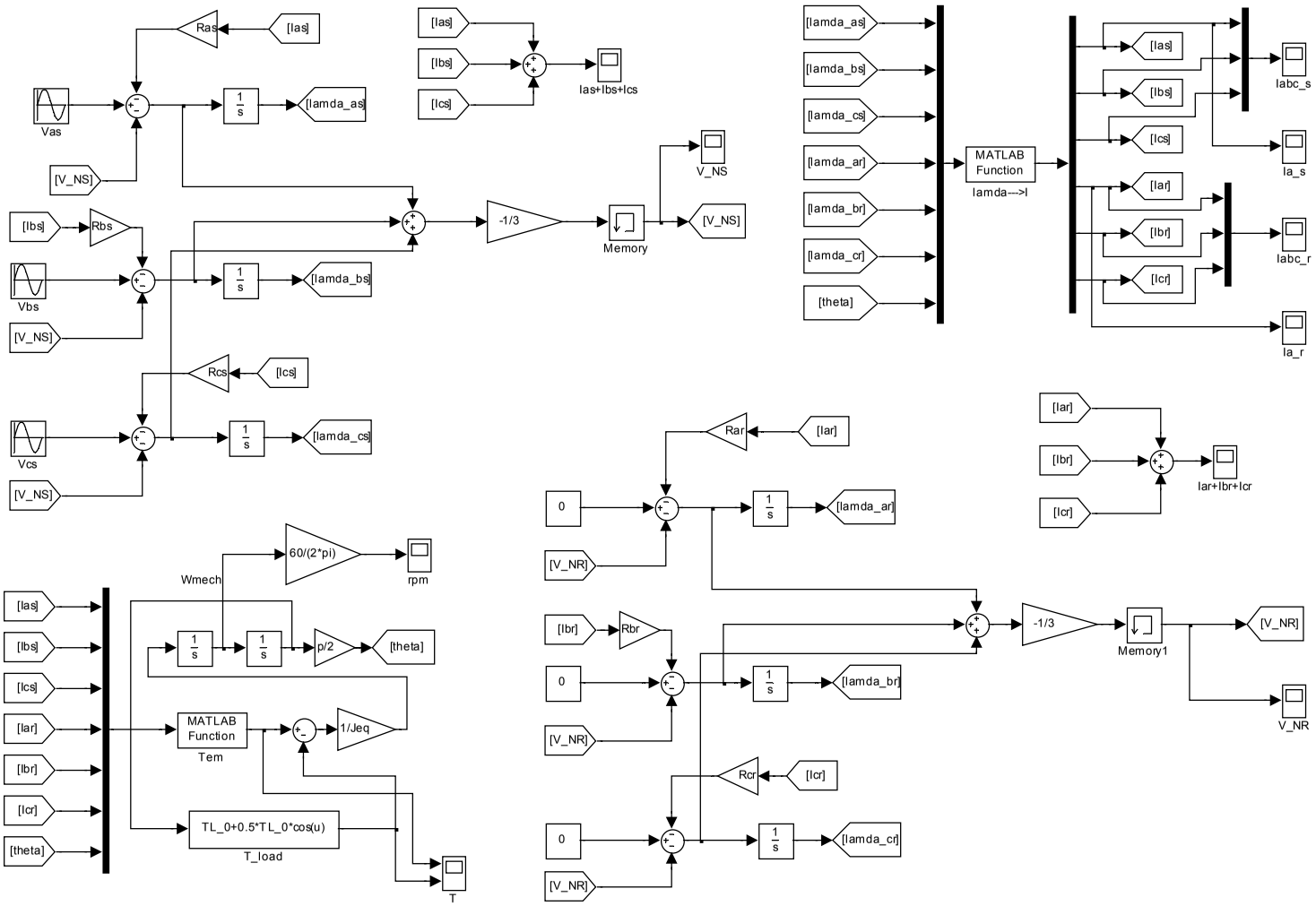

Figure 5.1 Simulink schematics using reformulated motor inductances for mains-fed machines

5.3.2 Purely Static Eccentricity in a Mains-Fed IM

A mains-fed 3-phase, 2-pole induction motor is simulated under a constant load condition for a purely static eccentricity fault with $\xi_s = 0.5,\ \alpha = 0$ and $slip = 0.0125$. It is clear from Figure 5.2 that only the fundamental component exists in the single phase i_a^s spectrum. By taking the rotating reference frame transformation method, fundamental positive and negative sequence components are separated in the i_{qs}^f spectrum at 50 Hz and 70 Hz, respectively, as shown in Figure 5.3, where $f = 10$ Hz.

Although simulation results here show that this method works well to manifest the negative sequence component for a purely static eccentricity, the rotating frequency of this new reference frame has to be selected very carefully to avoid undesired overlapping with other non-characteristic harmonics for a practical eccentric motor. In addition, negative sequence harmonics obtained from this technique may have different magnitudes for d-axis and q-axis components, which leads to an uncertainty in determining the actual levels of negative sequence characteristic harmonics.

A better way to distinguish positive and negative sequence components is to apply an FFT to the stator current space vector, $\vec{I}$, so that the fundamental sequence components are separated explicitly in Figure 5.4 at ±60 Hz. Due to its relative advantage over the reference frame transformation method, applying the FFT to the stator current or terminal voltage space vector will be used later on to extract negative sequence information in the terminal quantities.

Repeated simulations, including varying the constant load level, the static eccentricity coefficient, ξ_s, and the motor fault position, α, lead to some insightful observations. The positive sequence fundamental current increases significantly from no

load to full load, but the negative sequence fundamental component almost remains unchanged while keeping a constant $\xi_s = 0.5$. Therefore, the normalized negative sequence fundamental component, I_{ne}^*, with respect to the positive sequence fundamental counterpart, decreases as the load level increases (or rpm decreases) in Figure 5.5. In other words, the value of I_{ne}^* is highly dependent on the load level even for a fixed degree of static eccentricity.

On the other hand, the negative sequence fundamental component increases remarkably when the degree of static eccentricity increases. Meanwhile, the positive sequence component stays nearly unchanged for a constant load level. Thus, the value of I_{ne}^* increases as the severity degree of static eccentricity increases if the load level is fixed, as shown in Figure 5.6.

Variation of the motor fault position or the angle α does not impact the magnitudes of positive or negative sequence components. However, the phase angle difference between the fundamental positive and negative sequence components in i_q^f, i_d^f or $\vec{I}$ spectrum varies as a function of the angle α, as shown in Figure 5.7, if both the load level and the degree of static eccentricity are fixed. Simulation results also clearly demonstrate that the voltage levels at both stator and equivalent rotor winding neutral points maintain zero in the presence of a static eccentricity. This observation will be further theoretically verified in Chapter 6. Actually, zero sequence information acts as an important distinction between the rotor eccentricity and the stator inter turn fault although both of them yield parameter unbalance inside the motor.

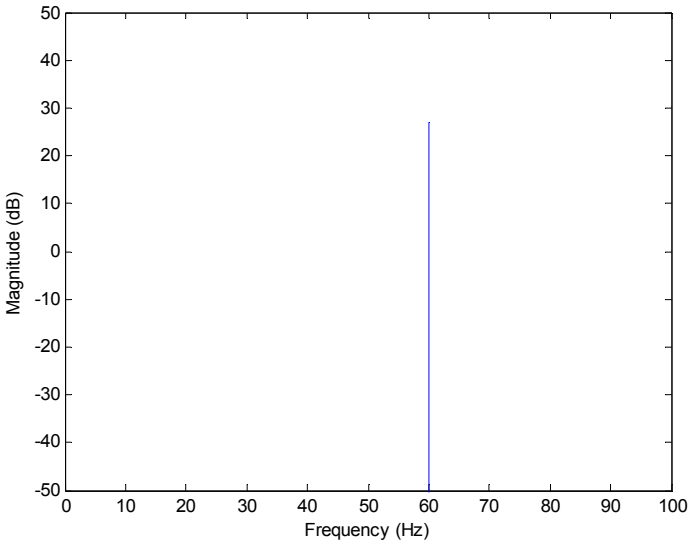

Figure 5.2 Simulated mains-fed i_a^s spectrum with $\xi_s = 0.5$, $\alpha = 0$, $slip = 0.0125$

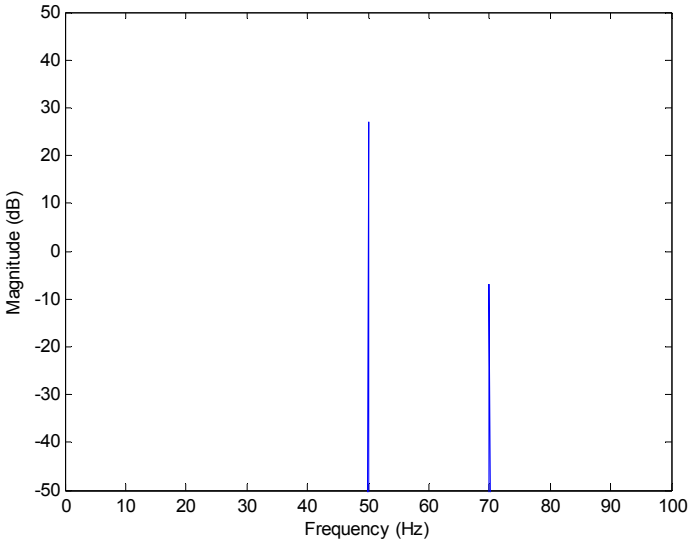

Figure 5.3 Simulated mains-fed i_q^f spectrum with $\xi_s = 0.5$, $\alpha = 0$, $slip = 0.0125$

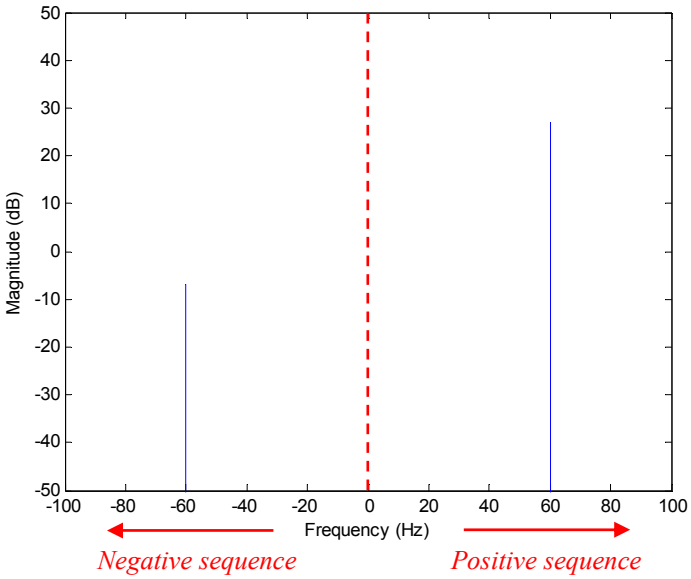

Figure 5.4 Simulated mains-fed $\vec{I}$ spectrum with $\xi_s = 0.5$, $\alpha = 0$, $slip = 0.0125$

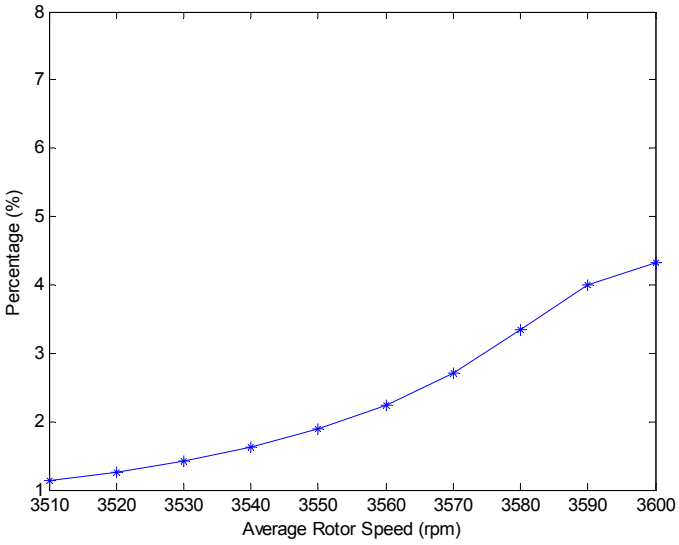

Figure 5.5 Normalized negative sequence fundamental component w.r.t. the load level where $\xi_s = 0.5$, $\alpha = 0$

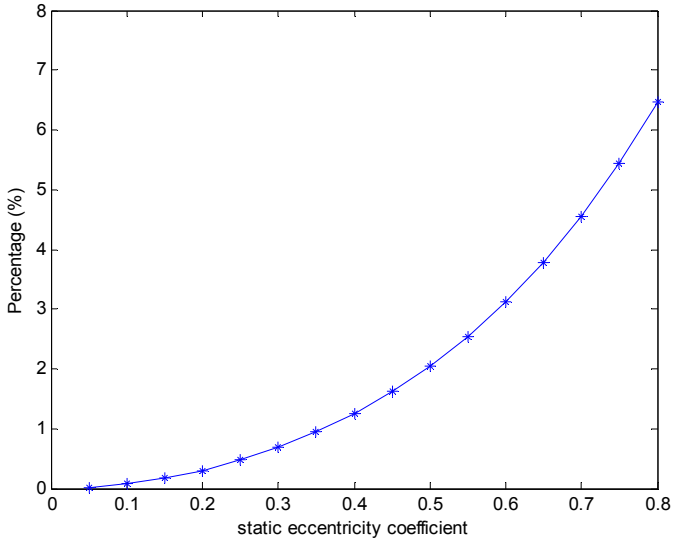

Figure 5.6 Normalized negative sequence fundamental component w.r.t. the degree of static eccentricity where $slip = 0.0125$, $\alpha = 0$

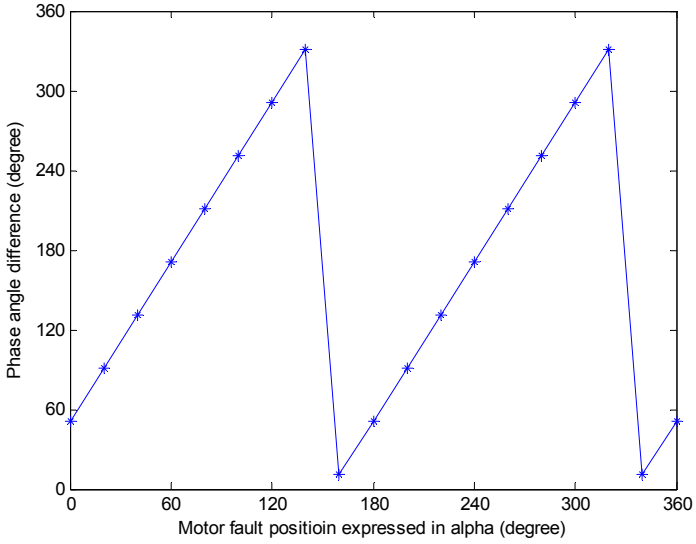

Figure 5.7 Phase angle difference between positive and negative sequence components w.r.t. the motor fault position where $\xi_s = 0.5$.

5.3.3 Purely Dynamic Eccentricity in a Mains-Fed IM

Single phase stator current spectrum for a purely dynamic eccentricity with a constant load level in a mains-fed machine is shown in Figure 5.8, where $\xi_d = 0.5,\ \beta = 0$ and $slip = 0.0125$. Due to the dynamic airgap permeance modulation in this case, side-band harmonics located at $(1 \pm 2k \cdot s) f_e$ also appear in the stator currents. In other words, stator current harmonics at 61.5 Hz, 58.5 Hz, 63 Hz, 57 Hz, etc., exist for a dynamic eccentricity with $slip = 0.0125$. These dynamic eccentricity induced current harmonics are similar to those caused by a broken rotor bar fault since both of them introduce rotating asymmetry into the airgap magnetic field.

FFT analysis of the stator current space vector, as shown in Figure 5.9, demonstrates clearly that no negative sequence components, neither at fundamental nor side-band harmonics, exist for a purely dynamic eccentricity. Again, the stator and rotor neutral point voltages are confirmed to be zero in the simulation.

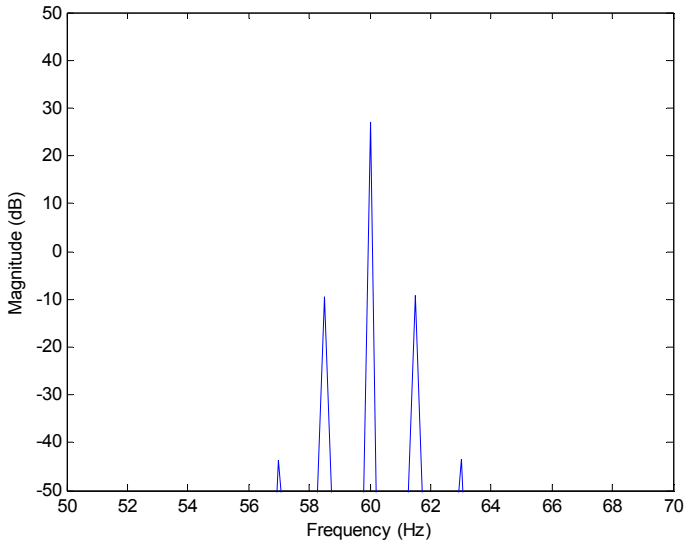

Figure 5.8 Simulated mains-fed i_a^s spectrum with $\xi_d = 0.5$, $\beta = 0$, $slip = 0.0125$

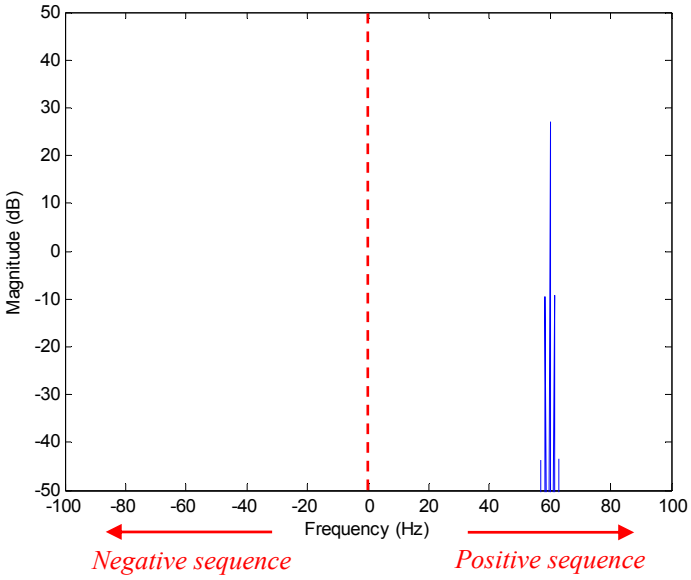

Figure 5.9 Simulated mains-fed $\vec{I}$ spectrum with $\xi_d = 0.5$, $\beta = 0$, $slip = 0.0125$

5.3.4 Mixed Rotor Eccentricity in a Mains-Fed IM

For a mixed rotor eccentricity, characteristic side-band harmonics at $f_e \pm k \cdot f_{rm}$ can be detected in the single phase stator current spectrum, as shown in Figure 5.10, where $\xi_s = 0.5$, $\xi_d = 0.5$, α=15°, $\beta = 0$, and at a constant load level with $slip = 0.0125$. Although harmonics at $f_e - k \cdot f_{rm}$ can be identified by zooming in the current spectrum, their magnitudes are not trustable due to the FFT spectrum leakage effects for this 2-pole machine at a light load condition. Characteristic harmonics located at $f_e + k \cdot f_{rm}$ serve as more reliable indicators for a mixed rotor eccentricity in this case.

The spectrum of the stator current space vector is shown again in Figure 5.11, where the sequence components at the characteristic harmonics $f_e + k \cdot f_{rm}$ are explicitly separated. Similar to a purely static or dynamic eccentricity, variation of the motor fault position, i.e., variation of the values for angle α and/or β, does not change the magnitudes of sequence components for a mixed rotor eccentricity.

Mixed rotor eccentricity also introduces a shaft speed oscillation as shown in Figure 5.12, where the average speed is still kept around 3555 rpm or $slip = 0.0125$. In other words, the average shaft speeds for a healthy and an eccentric motor are almost same while maintaining the same load level.

Since the stator and rotor neutral points always remain at zero voltage, simulation schematics shown in Figure 5.1 can be simplified to those shown in Figure 5.13 in order to accelerate the simulation speed for a mains-fed machine.

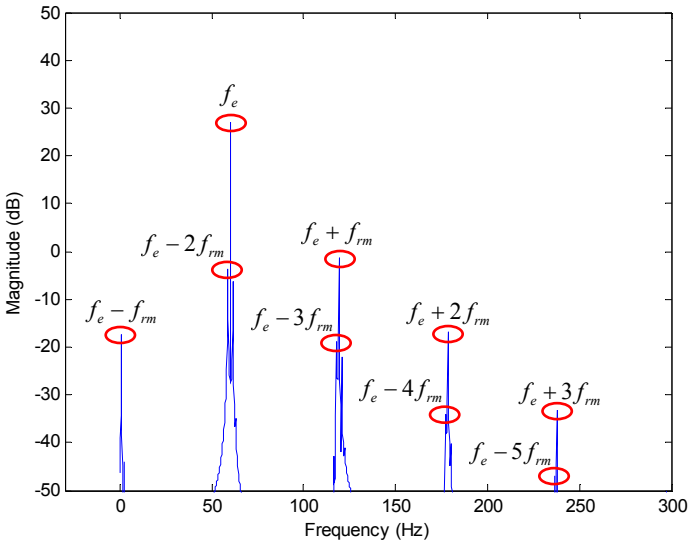

Figure 5.10 Simulated mains-fed i_a^s spectrum with $\xi_s = 0.5$, $\xi_d = 0.5$, α=15°, $\beta = 0$, $slip = 0.0125$

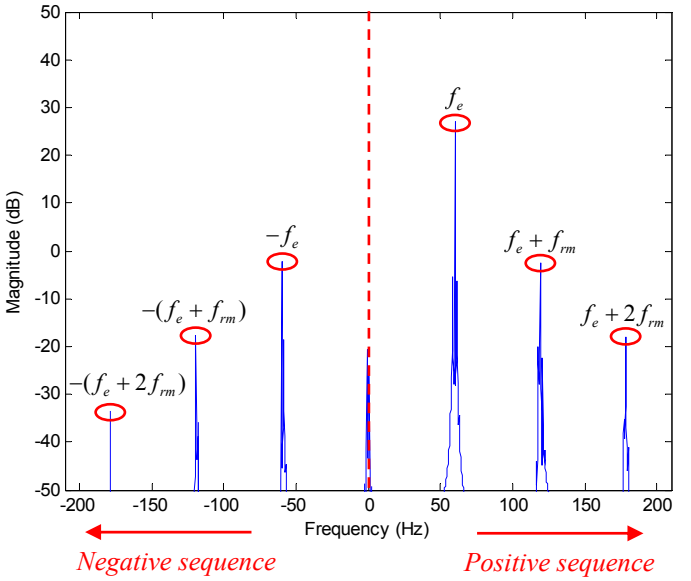

Figure 5.11 Simulated mains-fed $\vec{I}$ spectrum with $\xi_s = 0.5$, $\xi_d = 0.5$, α=15°, $\beta = 0$, $slip = 0.0125$

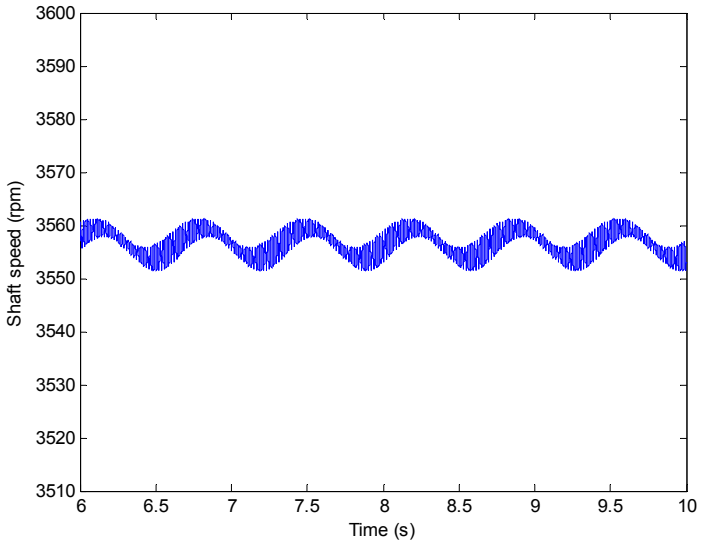

Figure 5.12 Simulated mains-fed motor shaft speed profile with $\xi_s = 0.5$, $\xi_d = 0.5$, α=15°, $\beta = 0$, $slip = 0.0125$

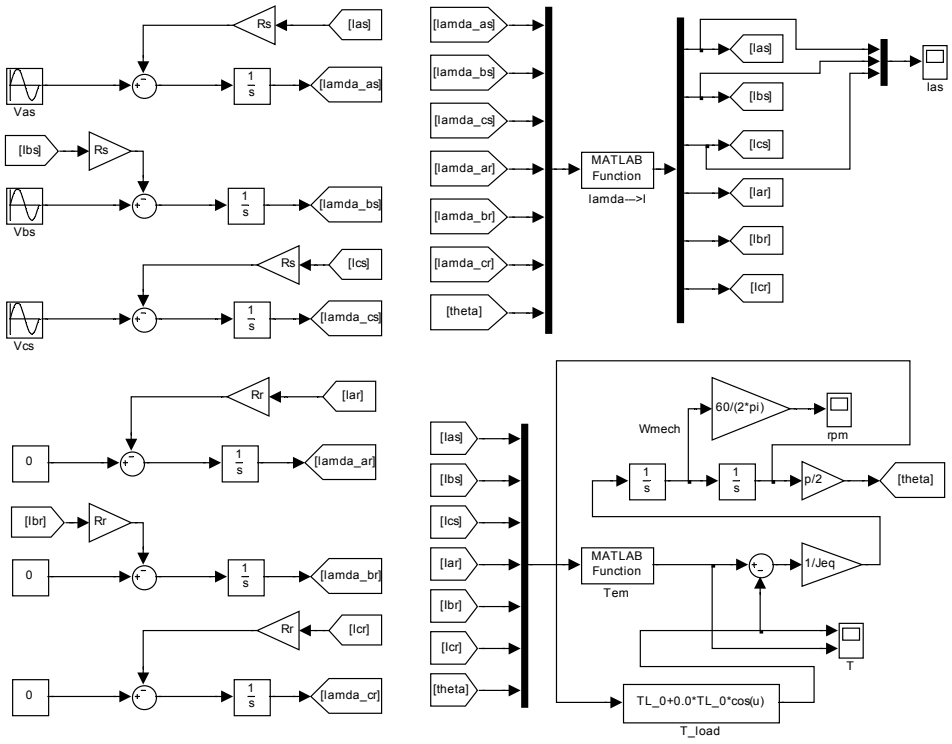

Figure 5.13 Simplified Simulink schematics to simulate mains-fed rotor eccentricities

Simulation results shown in Figure 5.10 through Figure 5.12 correspond to a mixed rotor eccentricity with $\xi_s = 0.5$ and $\xi_d = 0.5$. The purpose of applying these coefficients is to explicitly show all the rotor eccentricity characteristic harmonics in the stator current spectrum and, therefore, to further verify the effectiveness of those reformulated machine inductance matrices presented in Chapter 3. Obviously, the chosen values of $\xi_s = 0.5$ and $\xi_d = 0.5$ are far away from the practical case. A more reasonable setting for a mixed rotor eccentricity is to set $\xi_s = 0.3$ and $\xi_d = 0.2$. Simulation results corresponding to this setting are shown in Figure 5.14 through Figure 5.16. In practice, only the two most dominant characteristic harmonics $f_e \pm f_{rm}$ have a sufficiently large magnitude to be effectively monitored in the stator current spectrum, whereas negative sequence harmonic information at $-(f_e + f_{rm})$ is a more reliable indicator to detect the induced motor asymmetry.

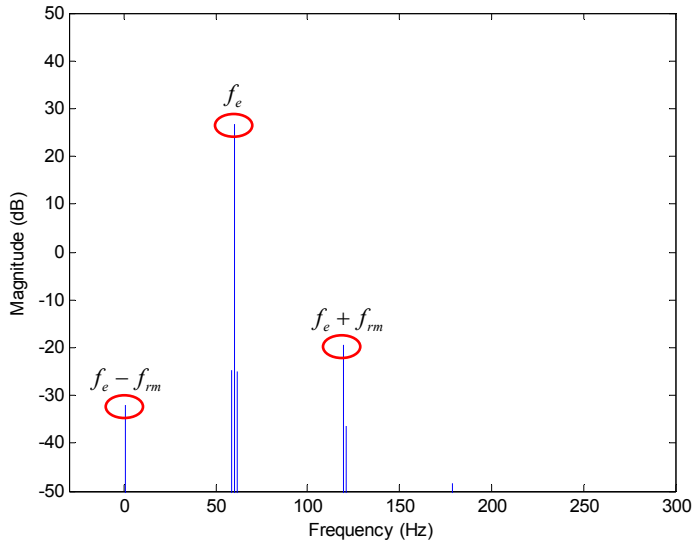

Figure 5.14 Simulated mains-fed i_a^s spectrum with $\xi_s = 0.3$, $\xi_d = 0.2$, α=0, $\beta = 0$, $slip = 0.0125$

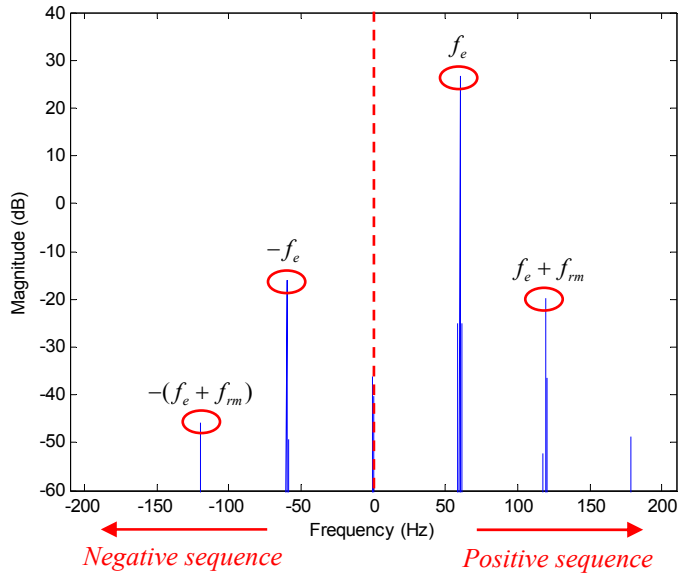

Figure 5.15 Simulated mains-fed $\vec{I}$ spectrum with $\xi_s = 0.3$, $\xi_d = 0.2$, α=0, $\beta = 0$, $slip = 0.0125$

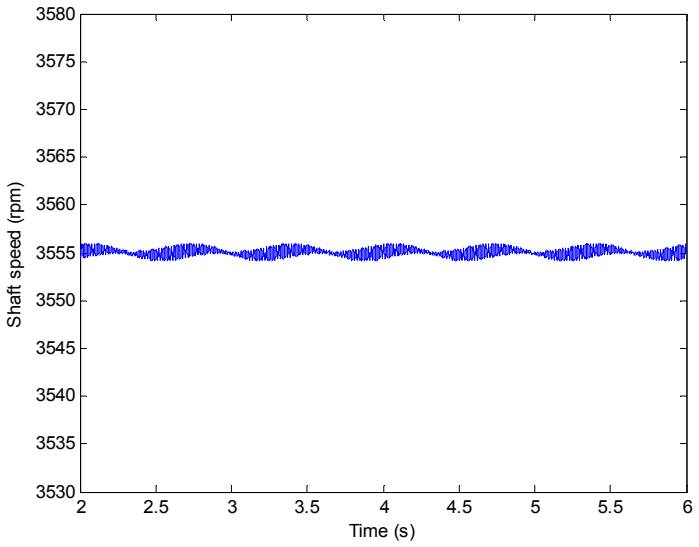

Figure 5.16 Simulated mains-fed motor shaft speed profile with $\xi_s = 0.3$, $\xi_d = 0.2$, α=0, $\beta = 0$, $slip = 0.0125$

5.3.5 Position-Dependent Load Oscillation in a Mains-Fed IM

A 100% load torque oscillation, $T_{load} = T_{avg} + T_{avg} \cdot \cos(\theta_{rm})$, is implemented in the simulation to show the load oscillation-induced side-band harmonics. Simulation results shown in Figure 5.17 illustrate a much larger harmonic magnitude at $f_e + f_{rm}$ for a load torque oscillation case compared with that resulting from a rotor eccentricity in Figure 5.14. Under this ideal simulation condition, i.e., purely sinusoidal input voltage and perfectly symmetric motor, there is no negative sequence component in the stator current space vector spectrum, as shown in Figure 5.18.

A load torque oscillation also leads to a relatively large fluctuation in the simulated shaft speed profile of Figure 5.19. Note that the average motor speed is still kept at 3555 rpm. In practice, this shaft speed oscillation resulting from a load torque oscillation is significantly diminished by the mechanical damping effects.

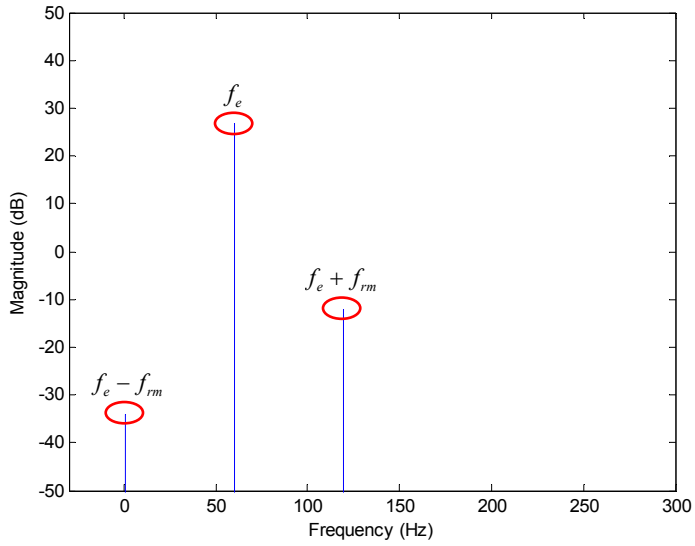

Figure 5.17 Simulated mains-fed i_a^s spectrum with 100% load torque oscillation

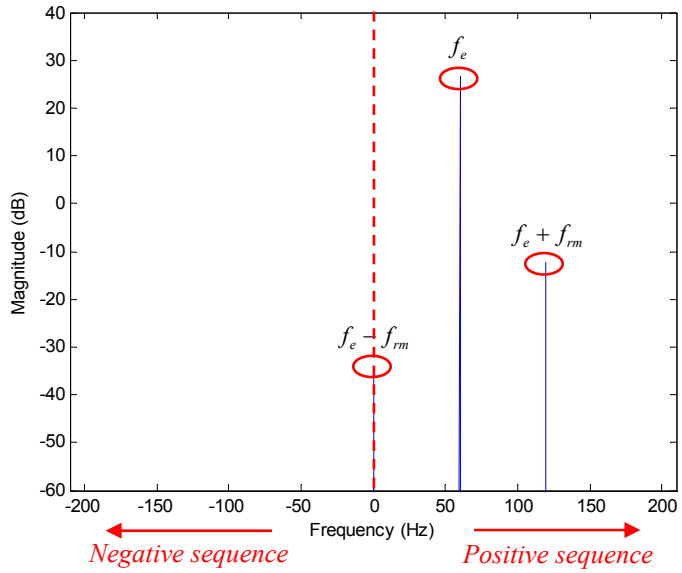

Figure 5.18 Simulated mains-fed $\vec{I}$ spectrum with 100% load torque oscillation

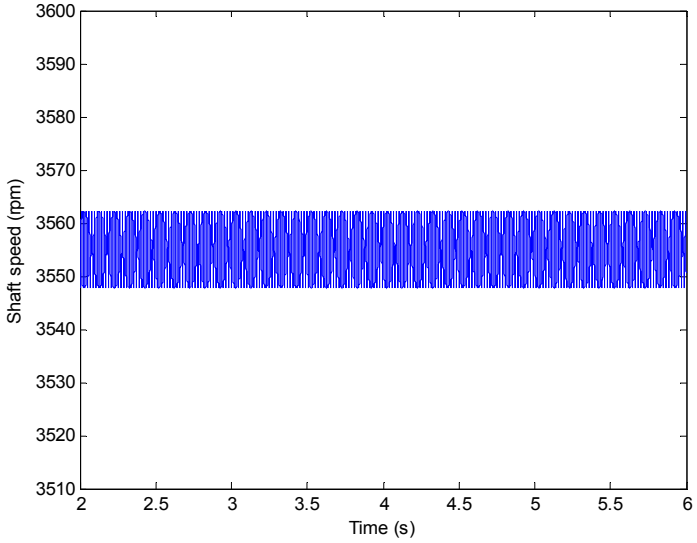

Figure 5.19 Simulated mains-fed motor shaft speed profile for a healthy motor with 100% load torque oscillation

5.4 A New Eccentricity Indicator for Drive-Connected Machines

In principal, a closed-loop induction motor drive provides a current-regulated voltage source to the motor. It typically consists of an inner, high bandwidth, current-regulating loop and an outer, low bandwidth, speed-regulating loop, as shown in Figure 5.20. The current control loop is implemented in a synchronous reference frame and PI controllers are used in both loops to achieve low steady state errors. Due to the intrinsic PI controller low-pass filtering characteristics, part of the eccentricity related characteristic harmonic information is transferred from the stator currents to the motor terminal voltages, depending on the control loop regulation capabilities. This complementary relationship in the distribution of rotor fault indicators requires detecting eccentricity related harmonics in both stator current and stator voltage spectra simultaneously [41]-[43].

Similarly, a rotor position dependent load torque oscillation in a closed-loop, drive-connected induction motor introduces exactly the same harmonic components in both stator current and terminal voltage spectra as well. These load oscillation related harmonics usually have much larger magnitudes and are likely to cause ambiguity in rotor eccentricity detection. Therefore, similar to a mains-fed machine, some new eccentricity-only related information has to be extracted to eliminate load oscillation effects in a drive-connected induction motor.

In a mains-fed or open-loop controlled induction motor, motor asymmetry is completely reflected into the stator currents [44]. Specifically, negative sequence harmonic information, instead of the negative sequence fundamental information, should be detected considering the inevitable unbalance in the mains supply. However, this

scheme can not be directly applied to a closed-loop drive application since the negative sequence harmonic information is extremely small in a drive-connected induction motor due to the relatively strong PI controller regulation capabilities.

On the other hand, the drive-connected motor terminal voltages come from the current regulated voltage source inverter. The inherent unbalance in the inverter output is very small, which is notably different from the mains-fed machine case. In addition, due to the control loop low-pass filtering characteristic, all negative sequence information would be completely transferred to the terminal voltages if the PI controller regulation capabilities were perfect. In practice, both stator currents and terminal voltages contain eccentricity induced motor asymmetry information. Therefore, negative sequence fundamental components in both stator currents and terminal voltages need to be monitored in a closed-loop drive.

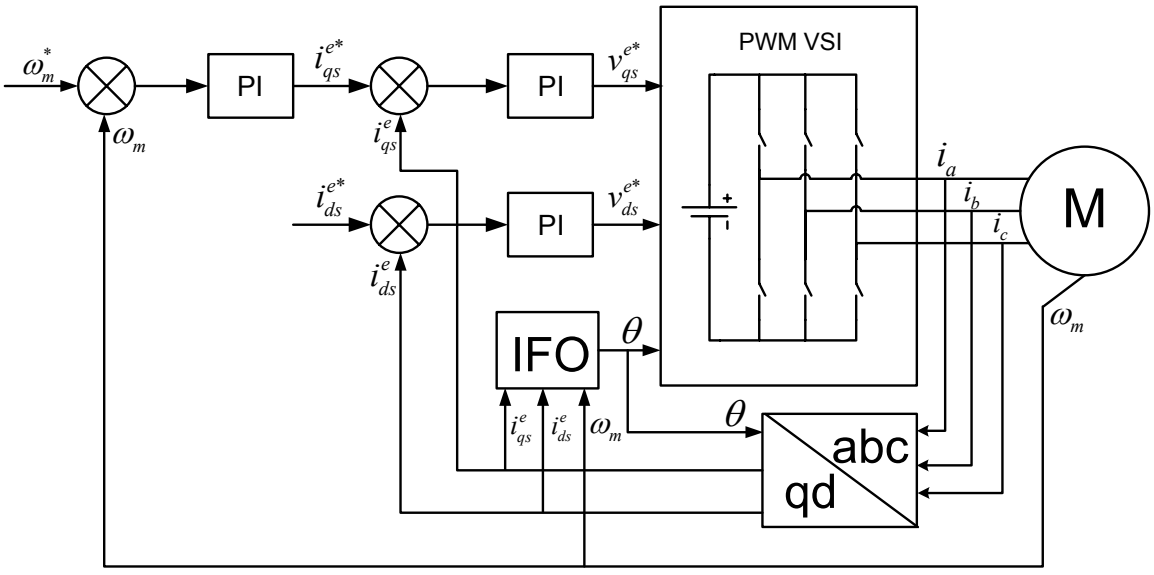

Figure 5.20 A typical closed-loop induction motor drive system

Rotor eccentricity induced motor asymmetry comes from the parameter unbalance in the inductance matrices and is a function of the stator excitation frequency and the slip frequency. The distribution ratio of the negative sequence information in the stator currents and the terminal voltages is also frequency dependent. To accurately evaluate the rotor eccentricity-induced motor asymmetry level, a summation of the normalized negative sequence fundamental components with respect to their positive sequence fundamental counterparts in the stator currents and the terminal voltages is proposed to be an additional rotor eccentricity fault indicator. That is,

$$\delta = I_{ne}^{*} + V_{ne}^{*} = \frac{I_{ne}}{I_{pe}} + \frac{V_{ne}}{V_{pe}} \tag{5.11}$$

where I_{ne}, I_{pe}, V_{ne} and V_{pe} denote the magnitudes of negative and positive sequence fundamental components in stator currents and terminal voltages, respectively. Since the bandwidth and closed-loop transfer function characteristics of the regulators are normally unknown, it is not possible to formulate a more sophisticated summation of the normalized voltage and current. For this reason, a simple unweighted sum is adopted.

For a closed-loop drive-connected induction motor, the proposed additional fault indicator, δ, combined with the traditional characteristic harmonic indicators in stator current and terminal voltage spectra, provide reliable and sensitive detection of rotor eccentricity faults even in the presence of a load torque oscillation.

5.5 Matlab Simulation for a Drive-Connected Induction Motor

The stator and equivalent rotor neutral points have been confirmed from simulation results to have a zero voltage level for a mains-fed eccentric motor. In other words, the neutral points ideally have the same potential level as the ground. Simulation schematics for a closed-loop, drive-connected induction motor is shown in Figure 5.21, where the speed loop and current loop bandwidths are set to be 25 rad/s and 2000 rad/s, respectively. Corresponding PI controller proportional gain, k_p, and integral again, k_i, for each loop are calculated accordingly [39]-[41]. The mechanical reference speed is selected to be 3000 rpm, leading to $f_{rm} = 50$ Hz, and the average load torque is set to yield a drive excitation frequency of 50.75 Hz.

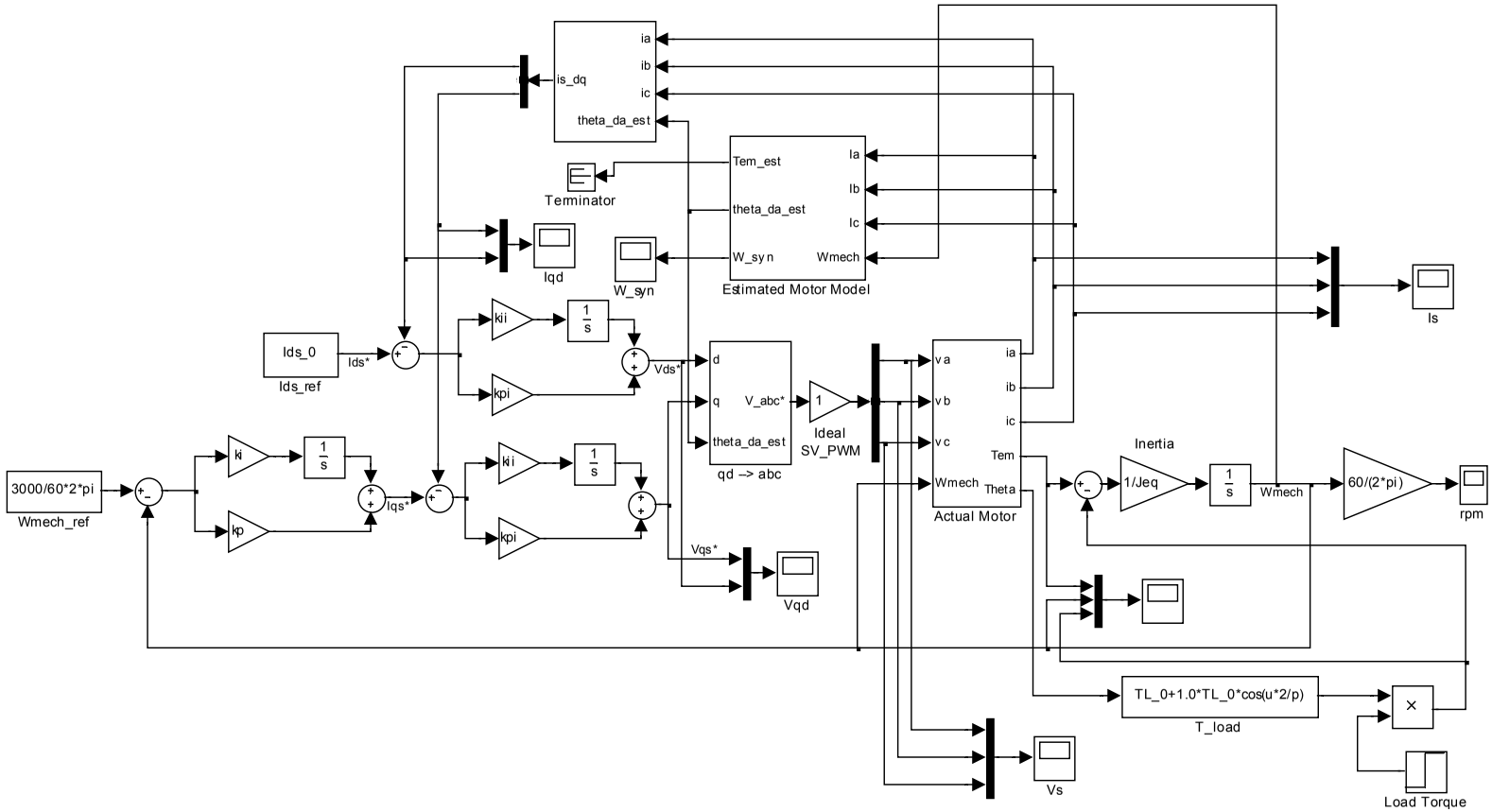

Figure 5.21 Simulink schematics using reformulated motor inductances for closed-loop drive-connected machines

5.5.1 Mixed Rotor Eccentricity in a Drive-Connected IM

Simulated single phase stator current and terminal voltage spectra for a mixed rotor eccentricity are shown in Figure 5.22 and Figure 5.23, where $\xi_s = 0.3$, $\xi_d = 0.2$, α=0, $\beta = 0$. The corresponding space vector spectra are shown in Figure 5.24 and Figure 5.25, respectively. It is clear from the simulation results that for a closed-loop drive-connected induction motor, the rotor eccentricity introduces dominant side-band harmonics in both the stator currents and the terminal voltages. As for the negative sequence information, it mainly exists in the current and voltage fundamental components. Meanwhile, negative sequence harmonic information in a closed-loop drive is much smaller compared with that in a mains-fed machine.

5.5.2 Position-Dependent Load Oscillation in a Mains-Fed IM

Simulation results for a 100% load torque oscillation in a closed-loop drive are shown in Figure 5.26 through Figure 5.29. Ideally, load oscillation yields only positive sequence information in stator currents and terminal voltages. Therefore, negative sequence fundamental information can be monitored to eliminate load oscillation effects.

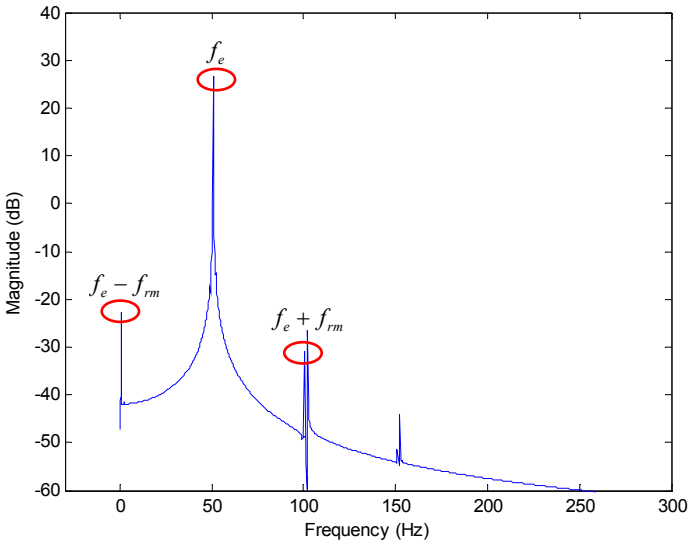

Figure 5.22 Simulated drive-connected i_a^s spectrum with $\xi_s = 0.3$, $\xi_d = 0.2$, α=0, $\beta = 0$

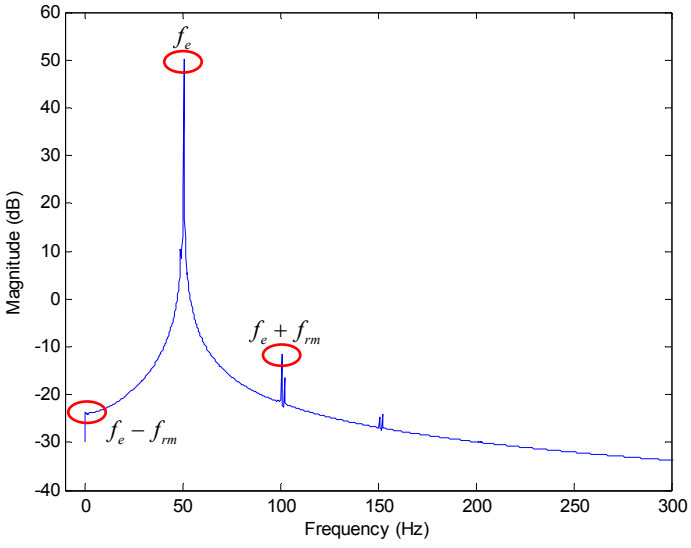

Figure 5.23 Simulated drive-connected v_a^s spectrum with $\xi_s = 0.3$, $\xi_d = 0.2$, α=0, $\beta = 0$

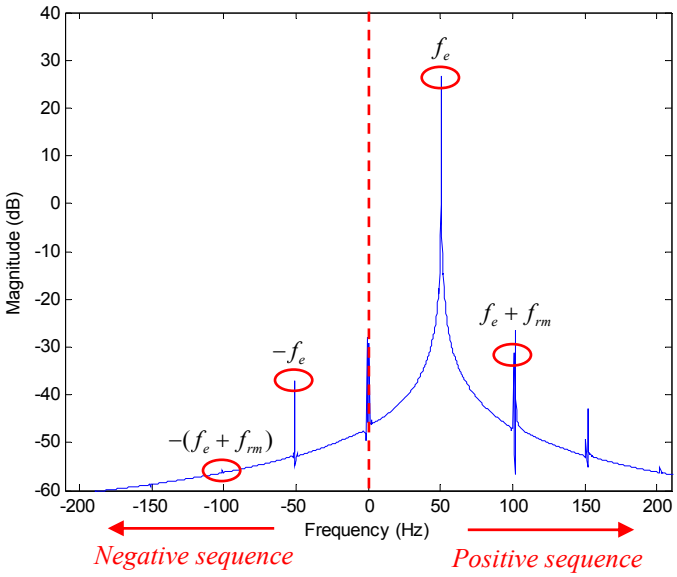

Figure 5.24 Simulated drive-connected $\vec{I}$ spectrum with $\xi_s = 0.3$, $\xi_d = 0.2$, α=0, $\beta = 0$

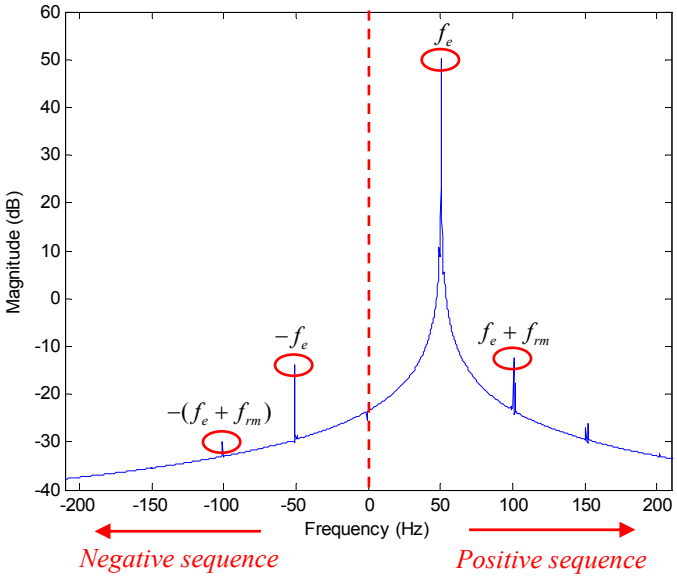

Figure 5.25 Simulated drive-connected $\vec{V}$ spectrum with $\xi_s = 0.3$, $\xi_d = 0.2$, α=0, $\beta = 0$

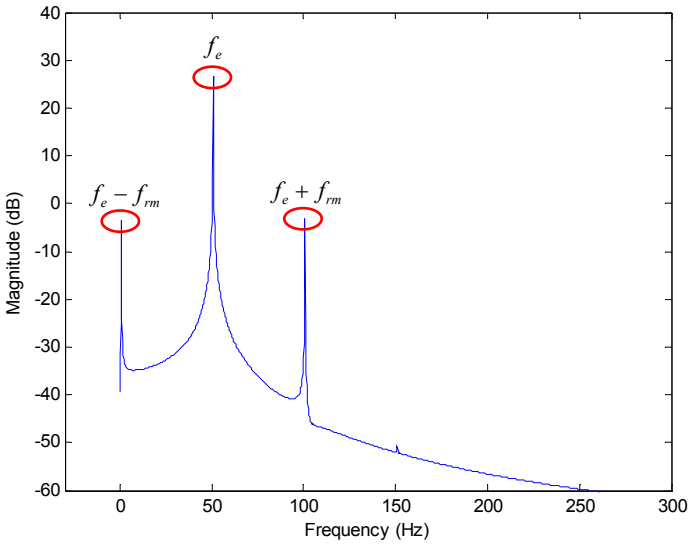

Figure 5.26 Simulated drive-connected i_a^s spectrum with 100% load torque oscillation

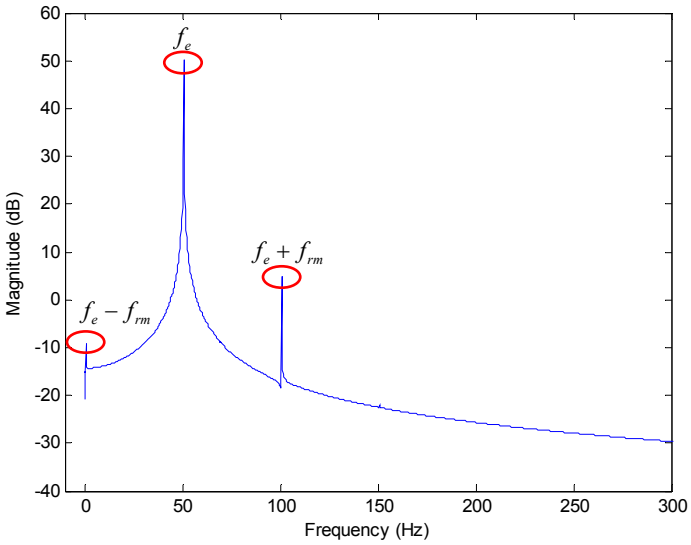

Figure 5.27 Simulated drive-connected v_a^s spectrum with 100% load torque oscillation

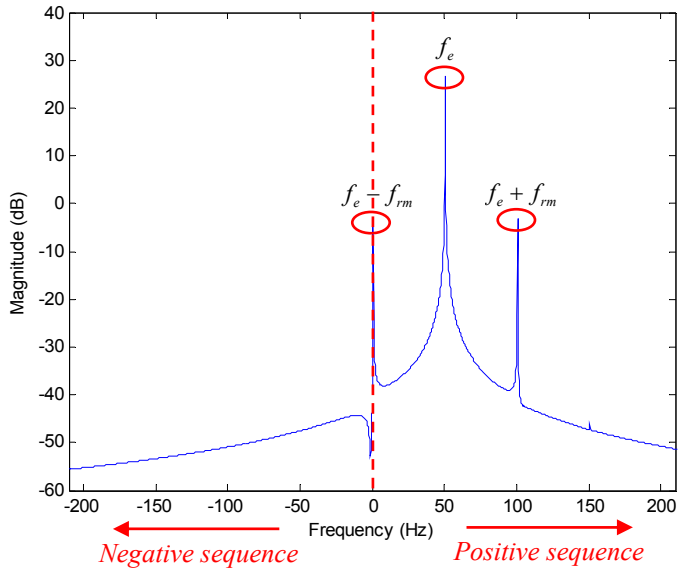

Figure 5.28 Simulated drive-connected $\vec{I}$ spectrum with 100% load torque oscillation

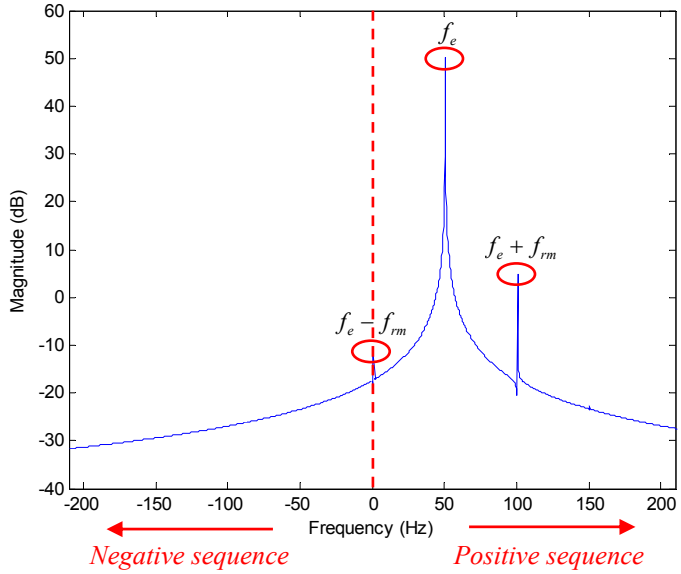

Figure 5.29 Simulated drive-connected $\vec{V}$ spectrum with 100% load torque oscillation

5.6 Simulation Results Based on Finite Element Model

FEA model-based simulation results are more convincing than those obtained from a Matlab model since FEA can incorporate magnetic saturation, winding space harmonics, as well as slotting effects in the simulation. Considering the fact that FFT analysis requires a fine frequency resolution to properly locate characteristic side-band harmonics, FEA simulation is extremely time-consuming when applying transient analysis for a sufficiently long period.

5.6.1 2-D Finite Element Model

A 36-slot, 28-bar, 2-pole induction motor can be modeled in Maxwell® 2D as shown in Figure 5.30. In order to simulate a purely static or dynamic eccentricity, the center of rotor can be moved away from the center of stator. In addition, the center of rotation can be also displaced from both the center of stator and the center of rotor to emulate a mixed rotor eccentricity fault.

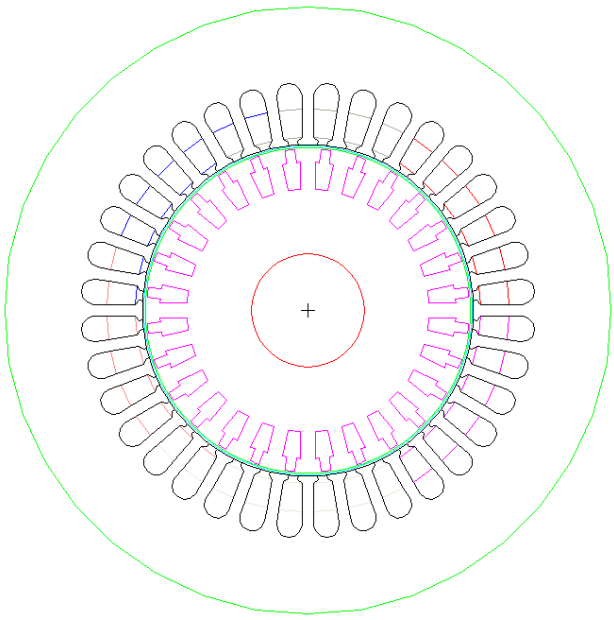

Figure 5.30 Maxwell 2D model for the induction motor

5.6.2 Mixed Rotor Eccentricity for a Mains-Fed Machine

Assuming D_s is the distance between the center of stator and the center of rotation, D_d is the distance between the center of rotor and the center of rotation, and D is the nominal motor airgap length, then the static eccentricity percentage is defined to be the ratio between D_s and D. Similarly, the dynamic eccentricity percentage is defined to be the ratio between D_d and D. In addition, the centers of stator, rotor and rotation lie on a straight line. A mixed rotor eccentricity with 30% static eccentricity and 30% dynamic eccentricity is implemented in the FEA model. Simulation results, shown in Figure 5.31 and Figure 5.32, clearly demonstrate the existence of side-band characteristic harmonics as well as negative sequence information in the stator currents.

5.6.3 Position-Dependent Load Oscillation for a Mains-Fed Machine

A 50% load torque oscillation was also simulated in the FEA model and it leads to much larger side-band harmonics in the simulation results shown in Figure 5.33 and Figure 5.34. Again, only positive sequence information exists in the stator currents.

It is important to note that the value of J_{eq} is critical to the magnitude of side-band harmonics resulting from a load torque oscillation. The smaller the value of J_{eq} used in the simulation, more significant the motor shaft speed oscillation and the larger the magnitude of induced side-band harmonics. For example, simulation results shown in Figure 5.33 and Figure 5.34 are based on a 50% load torque oscillation and one tenth of the nominal value of J_{eq} (J_{eq} is only 0.01 kg·m^2 for simulation results shown in Figure 5.33 and Figure 5.34). It is clear that side-band harmonics have much larger magnitudes in Figure 5.33 and Figure 5.34 than those in Figure 5.17 and Figure 5.18.

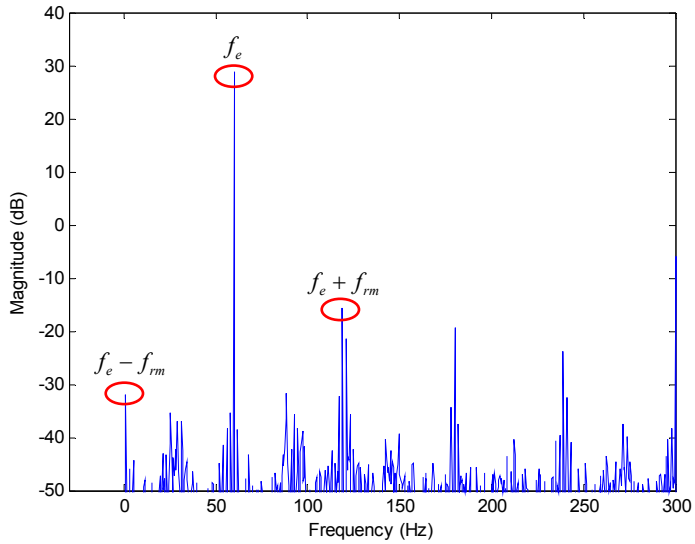

Figure 5.31 FEA model simulated mains-fed i_a^s spectrum with 30% static eccentricity and 30% dynamic eccentricity

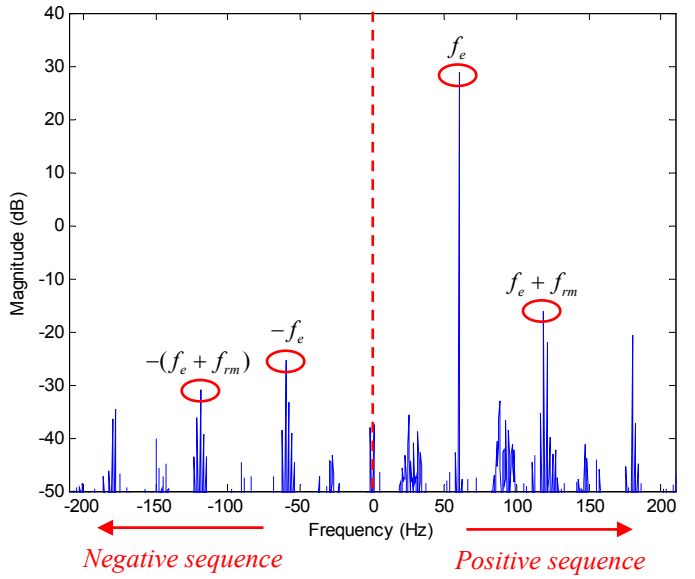

Figure 5.32 FEA model simulated mains-fed $\vec{I}$ spectrum with 30% static eccentricity and 30% dynamic eccentricity

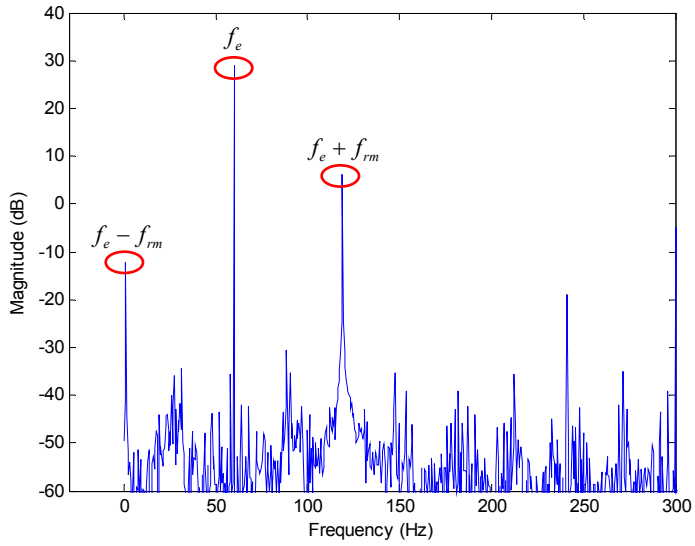

Figure 5.33 FEA model simulated mains-fed i_a^s spectrum with 50% load torque oscillation

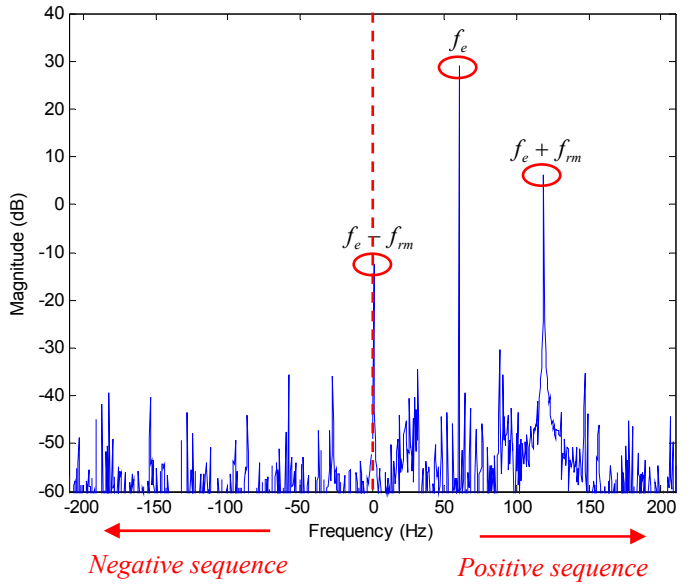

Figure 5.34 FEA model simulated mains-fed $\vec{I}$ spectrum with 50% load torque oscillation

5.6.4 FEA Simulation for a Drive-Connected Machine

FEA simulation for a closed-loop drive-connected induction motor can be implemented by incorporating vector control algorithm into FEA program. The control algorithm can be written in C and compiled into an executable file. In the Solver Setup window as shown in Figure 5.35, this executable file is specified to interact with the main FEA program after completing each iteration step of the magnetic field solution [41].

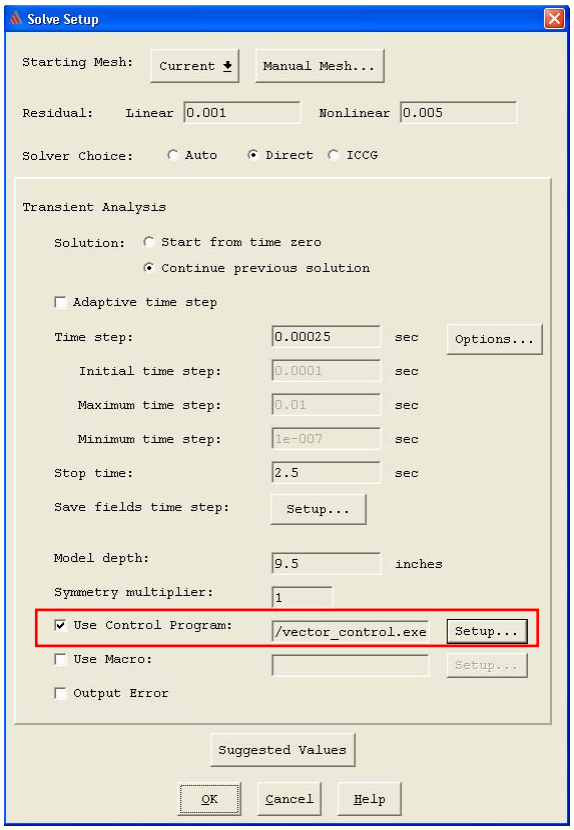

Figure 5.35 Maxwell 2D solver setup interface

5.7 Chapter Summary

In order to achieve an effective detection of rotor eccentricities in the presence of a load torque oscillation, eccentricity-only related information has to be extracted to eliminate load oscillation effects. Based on the different motor operation characteristics, additional rotor eccentricity indicator are developed for a mains-fed and a drive-connected induction motor, respectively. Extensive simulation results from both Matlab and FEA models are presented in this Chapter to confirm the efficacy of the proposed new rotor fault signature.

CHAPTER 6

SEPARATING ROTOR ECCENTRICITY INDUCED MOTOR ASYMMETRY FROM OTHER SOURCES

6.1 Overview

Although rotor eccentricity induced negative sequence information is a useful additional fault signature to eliminate load oscillation effects, negative sequence components in terminal quantities might result from other sources, such as unbalanced power supply, stator winding mismatch, magnetic saturation induced asymmetry, motor assembly defects, instrumentation imperfections, stator inter-turn faults, etc., [52]-[53]. Therefore, it is necessary to effectively differentiate eccentricity induced motor asymmetry from other factors.

6.2 Inherent Motor Asymmetry

Similar to the stator inter-turn fault detection, inherent motor asymmetry and instrumentation imperfectness should be properly evaluated throughout the motor operating range since they are highly dependent on the working conditions. In general, the effects of motor non-idealities are relatively easier to be compensated by either using data lookup table methods [45]-[46] or applying neural network techniques [44] during the motor commissioning stage.

6.3 Stator Inter-Turn Faults

A stator inter-turn fault leads to exactly the same negative sequence information as a rotor eccentricity, at both fundamental and characteristic side-band harmonics. There are

a few other techniques to assess the stator winding insulation condition, such as monitoring the sequence component impedance matrix [48]-[49], or detecting the voltage mismatch level [47]. However, these methods essentially still utilize the stator turn fault induced negative sequence information in motor terminal quantities. In the extreme case where both the load torque oscillation and the stator turn fault occur simultaneously, even the newly proposed additional rotor eccentricity indicator in (5.1) and (5.11) fails.

Fortunately, except for examining negative sequence information in stator currents and voltages, an incipient stator turn fault can be also detected by monitoring zero-sequence components [50]-[53]. The zero-sequence information serves as the last resort to separate eccentricity induced motor asymmetry from that caused by a stator turn fault.

6.4 Zero-Sequence Information

In a Y-connected induction motor, the zero-sequence voltage is defined as,

$$V_0 = \frac{1}{3}(V_{as} + V_{bs} + V_{cs}) \tag{6.1}$$

where V_{as}, V_{bs} and V_{bs} are the line-neutral voltages, which can be expressed in the following condensed form,

$$\overline{V}_{abcs} = r_s \cdot [E] \cdot \overline{i}_{abcs} + [L_{ss}] \cdot p\overline{i}_{abcs} + p[L_{ss}] \cdot \overline{i}_{abcs} + [L_{sr}] \cdot p\overline{i}_{abcr} + p[L_{sr}] \cdot \overline{i}_{abcr} \tag{6.2}$$

where $\overline{V}_{abcs}$, $\overline{i}_{abcs}$ and $\overline{i}_{abcr}$ are the stator voltage, stator current and rotor current vectors, respectively. The matrix $[E]$ is an identity matrix for a healthy or eccentric motor,

$$[E]_{healthy} = [E]_{ecc} = \begin{bmatrix} 1 & 0 & 0 \\ 0 & 1 & 0 \\ 0 & 0 & 1 \end{bmatrix} \tag{6.3}$$

Applying (6.2) into (6.1), a compact expression for the zero-sequence voltage can be obtained after a few steps of mathematical manipulation,

$$V_0 = (\frac{1}{3}) \sum_{n=a,b,c} V_{ns} = \sum_{n=a,b,c} \left\{ \begin{array}{c} \sum_{m=a,b,c} r_s \cdot [E]_{ms,ns} \cdot i_{ns} \\ + \sum_{m=a,b,c} [L_{ss}]_{ms,ns} \cdot pi_{ns} + \sum_{m=a,b,c} p[L_{ss}]_{ms,ns} \cdot i_{ns} \\ + \sum_{m=a,b,c} [L_{sr}]_{ms,nr} \cdot pi_{nr} + \sum_{m=a,b,c} p[L_{sr}]_{ms,nr} \cdot i_{nr} \end{array} \right\} \tag{6.4}$$

It is easy to show that the zero-sequence voltage for a healthy motor is ideally zero considering the fact that the summation of three phase currents is zero.

6.4.1 Zero-Sequence Information for a Stator Inter-Turn Fault

In the case of a stator inter-turn fault, each matrix in (6.2) has the following form,

$$[E]_{turn} = \begin{bmatrix} 1-\eta & 0 & 0 \\ 0 & 1 & 0 \\ 0 & 0 & 1 \end{bmatrix} \tag{6.5}$$

$$[L_{ss}]_{turn} = L_{ls} \cdot [E]_{turn} + L_{ms} \begin{bmatrix} (1-\eta)^2 & -\frac{1}{2}(1-\eta) & -\frac{1}{2}(1-\eta) \\ -\frac{1}{2}(1-\eta) & 1 & -\frac{1}{2} \\ -\frac{1}{2}(1-\eta) & -\frac{1}{2} & 1 \end{bmatrix} \tag{6.6}$$

$$[L_{sr}]_{turn} = L_{ms} \begin{bmatrix} (1-\eta)\cos(\theta_r) & (1-\eta)\cos(\theta_r + \frac{2}{3}\pi) & (1-\eta)\cos(\theta_r + \frac{4}{3}\pi) \\ \cos(\theta_r + \frac{4}{3}\pi) & \cos(\theta_r) & \cos(\theta_r + \frac{2}{3}\pi) \\ \cos(\theta_r + \frac{2}{3}\pi) & \cos(\theta_r + \frac{4}{3}\pi) & \cos(\theta_r) \end{bmatrix} \tag{6.7}$$

$$p[L_{ss}]_{turn} = \begin{bmatrix} 0 & 0 & 0 \\ 0 & 0 & 0 \\ 0 & 0 & 0 \end{bmatrix} \tag{6.8}$$

$$p[L_{sr}]_{turn} = -\omega_r L_{ms} \begin{bmatrix} (1-\eta)\sin(\theta_r) & (1-\eta)\sin(\theta_r + \frac{2}{3}\pi) & (1-\eta)\sin(\theta_r + \frac{4}{3}\pi) \\ \sin(\theta_r + \frac{4}{3}\pi) & \sin(\theta_r) & \sin(\theta_r + \frac{2}{3}\pi) \\ \sin(\theta_r + \frac{2}{3}\pi) & \sin(\theta_r + \frac{4}{3}\pi) & \sin(\theta_r) \end{bmatrix} \tag{6.9}$$

where η denotes the fractional percentage in the stator a-phase inter-turn fault. Substituting (6.5)-(6.9) into (6.4) gives the zero-sequence voltage for a stator inter-turn fault,

$$V_0 = \frac{1}{3}\left\{ \begin{array}{c} -\eta r_s I_s \cos(\omega_e t + \alpha) + \eta \omega_e L_{ls} I_s \sin(\omega_e t + \alpha) \\ +(\frac{3}{2} - \eta)\eta \omega_e L_{ms} I_s \sin(\omega_e t + \alpha) + \frac{3}{2}\eta \omega_e L_{ms} I_r \sin(\omega_e t + \beta) \end{array} \right\} \tag{6.10}$$

where I_s, I_r, α and β are the amplitudes and the initial a-phase angles for the stator and equivalent rotor currents, respectively. It is clear to see from (6.10), only fundamental component at ω_e ideally exists in the zero-sequence voltage for a stator inter-turn fault. The magnitude of the zero-sequence information is dominated by the contribution from the machine single phase magnetizing inductance, L_{ms}. In practice, for an inverter-fed machine, high-frequency components that are intrinsic to the PWM operation and triplen harmonics resulting from some types of modulation methods may also exist in the zero-sequence voltage. These harmonic components are not related to the stator inter-turn fault and can be easily low-pass filtered in the measurement instrumentation.

6.4.2 Zero-Sequence Information for Rotor Eccentricity

Similar calculation for the zero-sequence voltage can be applied to an eccentric motor by substituting (3.17)-(3.18) and (3.20)-(3.21), or (3.35)-(3.36) and (3.38)-(3.39), into (6.4) for a purely static eccentricity and a mixed rotor eccentricity, respectively. In both cases, rotor eccentricities result in a null zero-sequence voltage, which further confirms the conclusion obtained form simulation results presented in Chapter 5.

6.4.3 Comparison of Zero-Sequence Information

Theoretical analysis conforms to the physical reasoning very well. Rotor eccentricity faults only lead to a permeance modulation in the airgap and the resulting motor parameter unbalance in inductance matrices is symmetrically "seen" by three phase windings. Consequently, for an eccentric motor, summation of all column elements in inductance matrices (excluding leakage inductance components) as well as their derivatives is always zero. On the contrary, a stator inter-turn fault yields different effective number of turns for each phase and the resulting motor parameter unbalance is not symmetrical. Therefore, zero-sequence information arises in this case.

Although line-neutral voltages may not be accessible in all cases, monitoring zero-sequence information may still be incorporated into rotor eccentricity diagnostic strategies for some critical applications. Actually, continuous measurement of zero-sequence information does not increase the motor condition monitoring cost significantly [58]. With this additional zero-sequence measurement, it is beneficial to improve the total diagnostic performance for both rotor eccentricity and stator inter-turn faults detection.

6.5 Chapter Summary

This chapter presents a brief review of different factors that may produce negative sequence information in supply currents and/or terminal voltages. Motor inherent non-idealities and instrumentation mismatch can be determined and stored during the commissioning stage, and used later on to properly set up the fault signature threshold values in online motor condition monitoring. To effectively separate rotor eccentricity induced motor asymmetry from that resulting from a stator inter-turn fault, supplementary zero-sequence information has to be examined as well.

CHAPTER 7

EXPERIMENTAL SETUP AND IMPLEMENTATION OF LOAD TORQUE OSCILLATION

7.1 Overview - Basic Experimental Setup

The basic experimental setup is illustrated in Figure 7.1, wherein the experiments are performed for both mains-fed and closed-loop drive-connected induction motors. Motor terminal quantities are sensed through current/voltage transducers and fed into the National Instrument data acquisition (NI DAQ) device. The dynamometer of the motor consists of a DC generator and five parallel connected resistor banks. By controlling the on/off status of these rheostats, an oscillating load condition is emulated. A man-made rotor eccentricity is intentionally created inside the motor and tested under a constant load. The results obtained from an eccentric motor are further compared with those for a healthy motor under both constant load and oscillating load conditions.

7.1.1 Motor Eccentricity Implementation

To properly create a rotor eccentricity fault and avoid stator-to-rotor rub, the rotor outer surface is first machined to increase the airgap length from 0.014″ to 0.039″. A static eccentricity is created by enlarging the bearing housings and placing 0.01″ shims on both sides to offset the rotor. A dynamic eccentricity is created by machining the motor shaft below the bearing and inserting a 0.015″ shim on one side. For comparison purpose, another motor with the same specifications is also machined around the rotor outer surface to achieve exactly the same enlarged airgap length, while no eccentricity fault is created for the second motor.

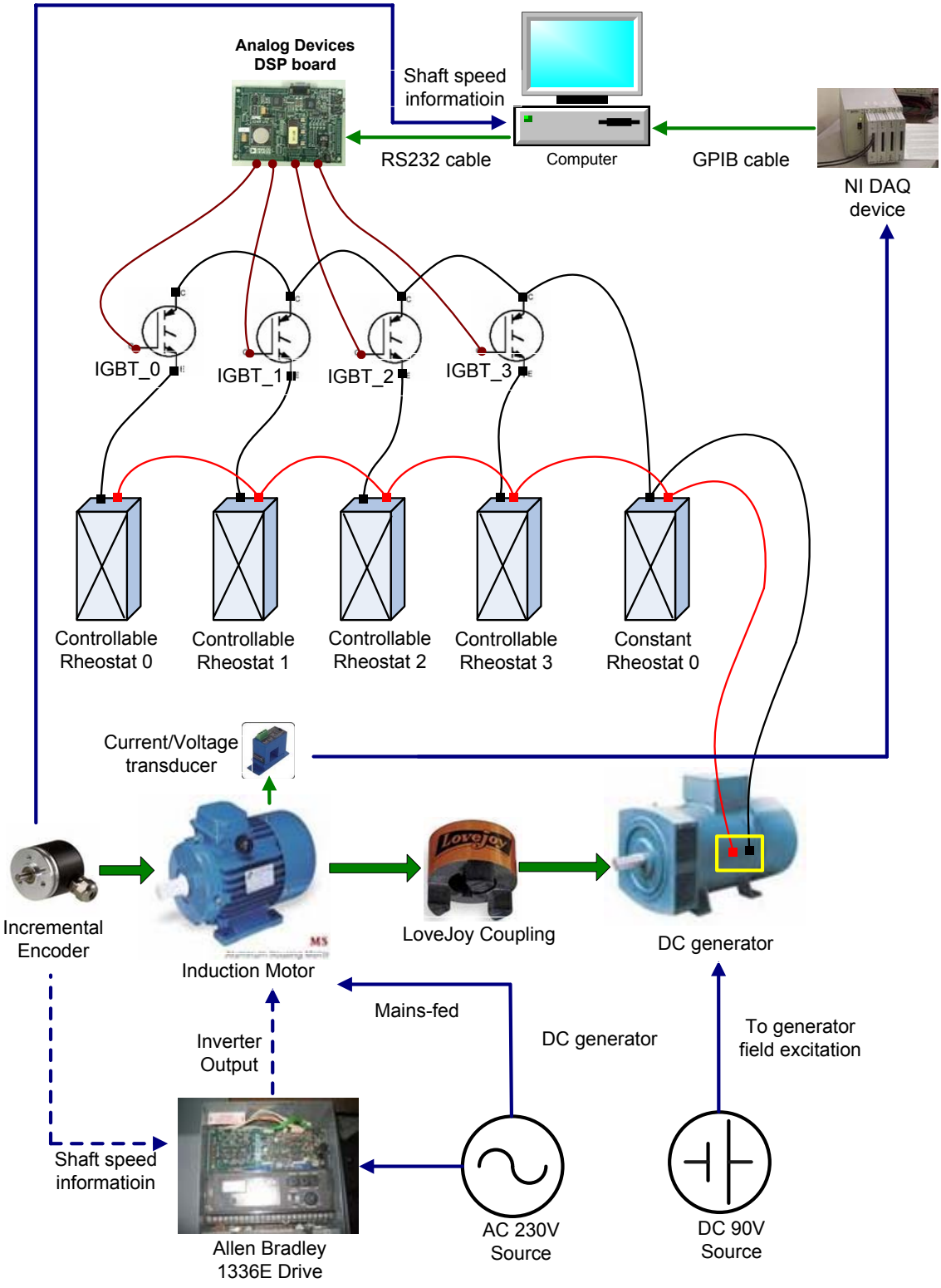

Figure 7.1 Illustration of experimental setup with load oscillation control circuit

The motor tested in the experiments is a three phase general purpose induction motor, whose nameplate data and impedance information are listed in Appendix B. The motor is only operated with 230 Volts configuration, resulting in two isolated neutrals in stator windings. Since the airgap length is significantly increased, the motor is operated with a larger slip (reduced speed) and lower output power if the stator current is still limited by the originally rated value.

7.1.2 Motor Dynamometer System

A 10 hp dc generator is linked to the motor shaft through Lovejoy couplings. Several resistor banks are connected in parallel to the dc machine armature winding to control the motor load level. A resistor bank has at most eight 50 ohm resistors and eight 100 ohm resistors connected in parallel. In general, for a constant load operation, one or two resistor banks are sufficient to reach the rated current condition with a dc field excitation of 90 Volts.

To implement an oscillating load, five resistor banks are connected in parallel to the dc generator, wherein four of them have a serially connected IGBT switch respectively, as shown in Figure 7.1. By controlling the on/off status of IGBTs, different numbers of resistor banks are plunged into the load system to imitate a quasi sinusoidal load torque oscillation.

7.1.3 Closed-Loop Drive Configuration

An Allen-Bradley drive 1336E drive is used for the closed-loop, drive-connected motor operation. Corresponding encoder is an Allen-Bradley 845S incremental optical one. Main parameters of the drive and the encoder are given in Appendix B.

7.1.4 Voltage and Current Measurements

For sensorless motor condition monitoring, only measurements of the supply currents and the terminal voltages are required. They can be sensed via LEM LA-55P and LEM LV-25P transducers, respectively. To analyze the characteristic side-band harmonics as well as the sequence information in terminal quantities, two phase currents (I_a, I_b) and two phase-phase voltages (V_{ab}, V_{bc}) measurements are sufficient. However, to evaluate zero-sequence information for a wye-connected induction motor, three phase-neutral voltage measurements are mandatory.

For the low voltage connection, there are two floating neutrals in stator windings, as shown in Figure 7.2, where both N_1 and N_2 are stator neutral points. Ideally, both neutrals should have the same voltage level assuming there is no mismatch among phase windings. For a complete assessment of zero-sequence information, both points should be detected.

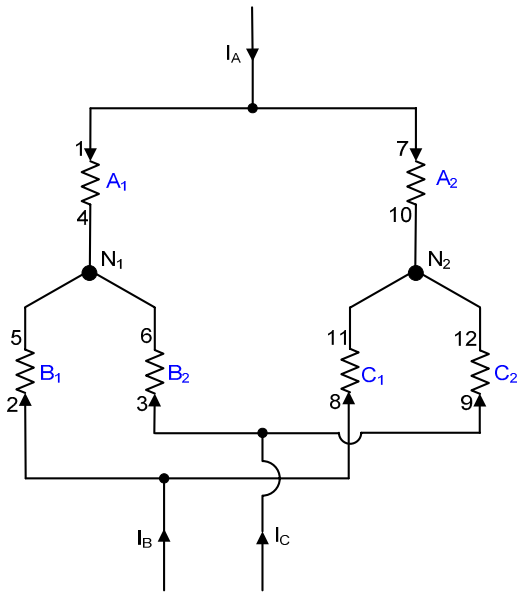

Figure 7.2 Stator winding configuration for 230 Volts operation

On-line data acquisition uses a 5 kHz sampling rate and a total 5 seconds sampling time to acquire a 0.2 Hz frequency resolution in the FFT spectral analysis. This measurement requirement consumes moderate memory storage and provides sufficient accuracy for the practical implementation.

7.2 Implementation of Load Torque Oscillation

One way to create a position-dependent load torque oscillation is to mount an unbalanced disk on the motor shaft. The unbalanced disk has a steel bolt and nut placed in holes on a balanced metal plate. These holes are drilled at different radial distances from the rotor shaft. The tangential force produced by the bolt and nut depend on their total mass, the radial distance from the shaft, and the shaft speed [38].

Although this experimental setup creates a small amount of load torque oscillation, it also imposes a significant centrifugal force on the motor shaft. Therefore, this method essentially creates a rotor eccentricity (mainly dynamic eccentricity) inside the motor, which is not the concerned case of a purely load torque oscillation in reciprocating compressors.

7.2.1 Purely Load Oscillation Implementation Principle

The schematics to implement a purely load torque oscillation is illustrated in Figure 7.3. In this scheme, each of the four resistor banks (R_0, R_1, R_2 and R_3) is serially connected to an IGBT to constitute a parallel branch of the dynamometer. The remaining resistor bank (R_4) is directly connected to the dynamometer dc output. For the control purpose, the gate signals for each IGBT switch are the outputs of an Analog Devices DSP board (SHARK® ADSP-2181). Detailed information regarding this DSP board is given in Appendix C.

The main Visual DSP++ program on the computer produces a sequence of user-defined high and low voltage signals (2 Volts and 0 Volts) at each of the four I/O flags on the DSP board. These DSP outputs are further sent to the IGBT board to control the on/off status of the IGBTs as well as the parallel branches. Each of the resistor banks R_1-R_4 has only one resistor R conducted and the consumed power would be V_{dc}^2/R if this parallel branch is on. The resistor bank, R_4, has $m \times R$ resistors connected in parallel and consumes a total power of $(m \cdot V_{dc}^2)/R$ continuously. The switching sequence for each parallel branch and the voltage level for the corresponding IGBT gate signal are given in Table 7.1. This switching pattern is repeated to yield a quasi sinusoidal load oscillation as plotted in Figure 7.4. One advantage of the proposed switching sequence is to keep the average load level unchanged before and during the load oscillation condition. Hence, no significant shaft speed variation occurs after the load oscillation is enforced. If the motor shaft speed is fed back to the main Visual DSP++ program to synchronize the motor speed with the switching frequency, a time-varying or position-varying load torque oscillation is accomplished with this scheme.

7.2.2 IGBT Configurations

The IGBT board configuration is shown in Figure 7.5. It consists of two IGBT modules and one single phase diode rectifier. The IGBT chip used in the experiments is IRGBC30U from International Rectifier, which has a collector-to-emitter blocking voltage of 600 Volts and a maximum continuous collector current of 23 A at room temperature. These ratings are sufficiently large for the experimental investigation of the load torque oscillation performed in this research. The IGBT module is connected to the DSP board through the BNC cables as shown in Figure 7.6.

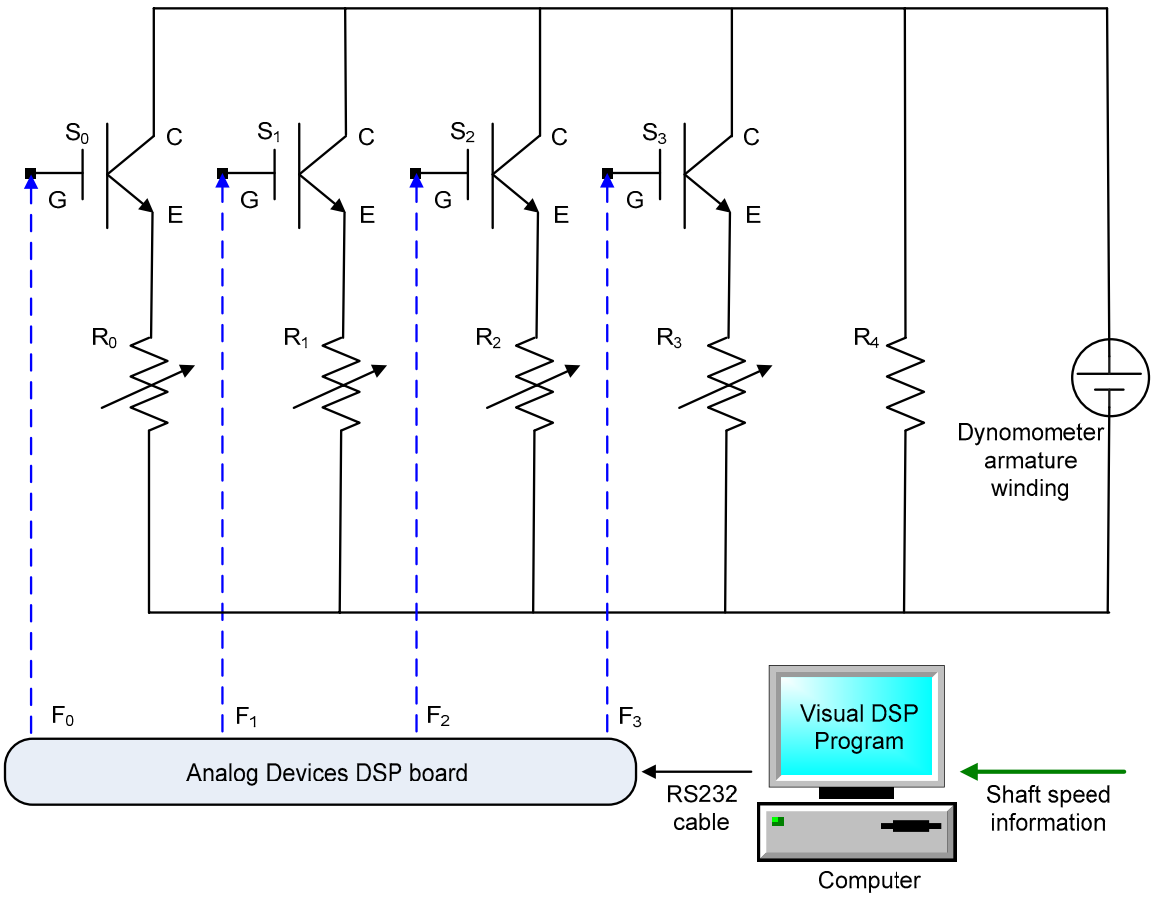

Figure 7.3 Schematics to control load torque oscillation

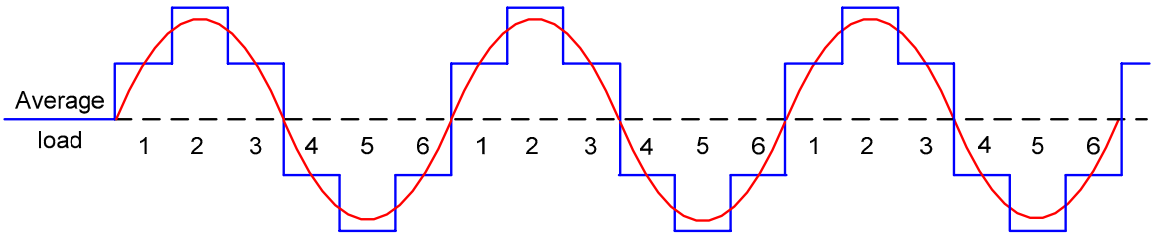

Figure 7.4 Quasi sinusoidal load torque oscillation profile

Table 7.1 Mechanism to implement a quasi sinusoidal load oscillation

K	Constant load	1	2	3	4	5	6	Repeat 1
F_0	H	H	H	H	H	L	H	H
F_1	H	H	H	H	L	L	L	H
F_2	L	H	H	H	L	L	L	H
F_3	L	L	H	L	L	L	L	L
$R_0 = R$	On	On	On	On	On	Off	On	On
$R_1 = R$	On	On	On	On	Off	Off	Off	On
$R_2 = R$	Off	On	On	On	Off	Off	Off	Off
$R_3 = R$	Off	Off	On	Off	Off	Off	Off	Off
$R_4 = R/m$	On	On	On	On	On	On	On	On
Output Power	$\frac{(m+2)\cdot V_{dc}^2}{R}$	$\frac{(m+3)\cdot V_{dc}^2}{R}$	$\frac{(m+4)\cdot V_{dc}^2}{R}$	$\frac{(m+3)\cdot V_{dc}^2}{R}$	$\frac{(m+1)\cdot V_{dc}^2}{R}$	$\frac{(m+0)\cdot V_{dc}^2}{R}$	$\frac{(m+1)\cdot V_{dc}^2}{R}$	$\frac{(m+3)\cdot V_{dc}^2}{R}$

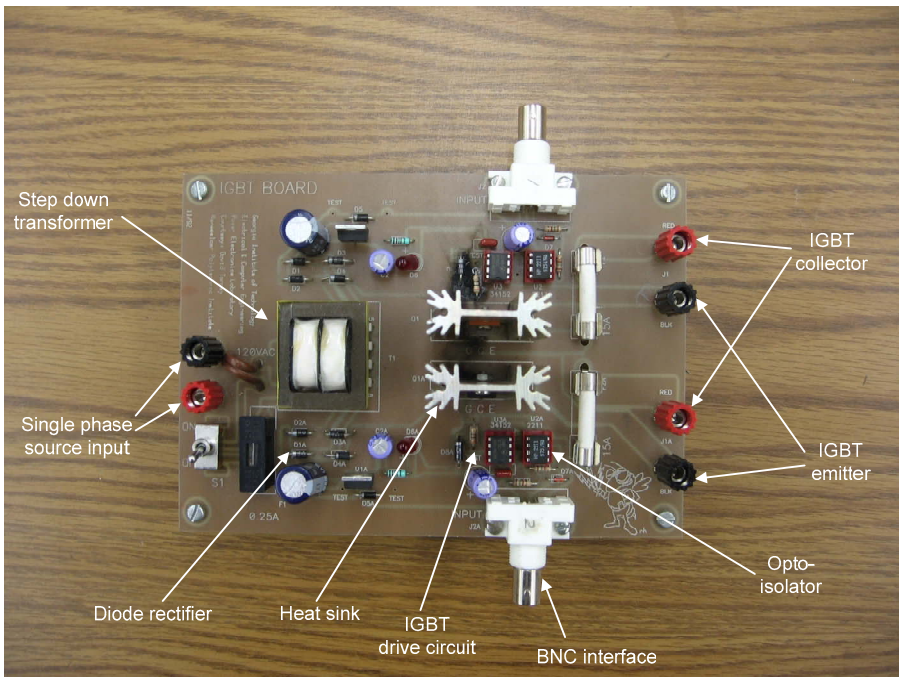

Figure 7.5 IGBT board configuration

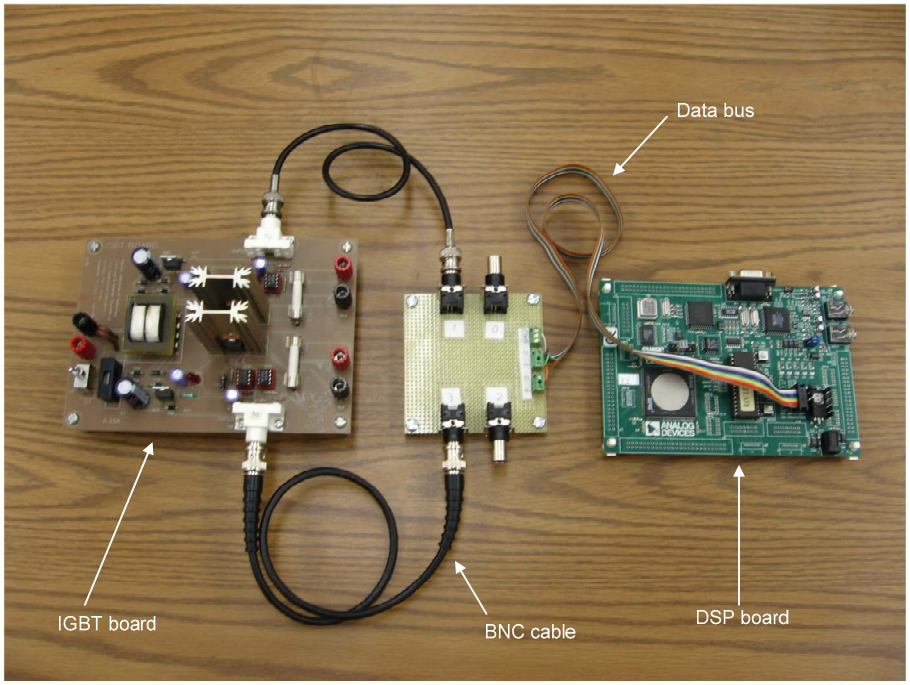

Figure 7.6 Connection between the DSP board and IGBT board

7.3 Chapter Summary

In this chapter, the experimental setup for the drive-motor-dynamometer system is described. Specifically, the method of creating a man-made rotor eccentricity as well as the principle and implementation of a time-varying (position-varying) load torque oscillation are emphasized in detail. For the purpose of illustration, pictures for the DSP board and the IGBT module are presented as well. The selected IGBT chip provides sufficiently large blocking voltage and current rating, which facilitate the experimental implementation of a load torque oscillation. Experiments are taken for the eccentric motor under a constant load and for the healthy motor under a load oscillation to evaluate the effectiveness of the newly proposed rotor fault indicator.

CHAPTER 8

RELIABLE ROTOR ECCENTRICTY DETECTION SCHEME AND EXPERIMENTAL RESULTS

8.1 Overview

Based on the experimental setup described in Chapter 7, extensive motor tests have been performed to verify the proposed new rotor eccentricity fault indicators used to eliminate load oscillation effects. In all the experimental results shown in this chapter, a relatively large degree of load oscillation, wherein the oscillating component is as large as the average torque, was used. This was done in order to emulate the real world case of a reciprocating compressor. This type of load represents the worst case of a position-dependent oscillating load torque. Furthermore, in the results of this chapter, the degree of eccentricity used in the experiments is relatively small (around 20%-30%). Using a large degree of load oscillation and a small degree of rotor eccentricity, the sensitivity and effectiveness of the proposed indicator is demonstrated and verified. Since these experiments are very difficult to implement at various levels of eccentricity, a practical worst case was chosen.

The eccentric motor was tested with a constant load level throughout the motor operating range from a mains supply and a current regulated voltage source inverter. For the purpose of comparison, the healthy machine was tested with two types of loads. First, the healthy motor runs with the same constant load level as that experienced by the eccentric motor. This type of load test for the healthy motor is beneficial to reveal the characteristic side-band harmonics caused by rotor eccentricities. It is also useful to

observe the dominant effects from the unbalanced power supply on the fundamental negative sequence information in the mains-fed supply currents.

Second, the healthy motor is tested with a load torque oscillation. Considering the fact that motor asymmetry information, which is evaluated via the normalized negative sequence components with respect to their positive sequence counterparts, is highly dependent on the load level or the motor speed, it is necessary to set the average load level during a load torque oscillation equal to the constant load tested for the eccentric machine. Thus, the average motor speed for the healthy motor with a load oscillation is very close to that for the eccentric motor with a constant load. Furthermore, the magnitudes of the positive sequence fundamental currents are almost same under these two test conditions. Actually, for a mains-fed machine, the shaft speed variation during a load oscillation is alleviated by the mechanical damping effect, which is dependent on the equivalent motor-load system inertia. For the closed-loop drive-connected case, the motor speed is almost constant even under a load oscillation condition due to the relatively strong regulation capabilities of the PI controllers.

8.2 Experimental Results for Mains-Fed Condition

The supply current space vector spectra for the eccentric motor with a constant load, as well as for the healthy motor with a constant load and an oscillating load are shown in Figure 8.1 through Figure 8.3, respectively. The average load level of the imitated load oscillation is set equal to the constant load for the eccentric and healthy motors. Therefore, the average speed for all three cases is around 1776 rpm and their positive sequence fundamental currents have nearly the same magnitudes.

Both rotor eccentricity and load torque oscillation show significant side-band harmonics in the stator current space vector spectrum, wherein the positive-sequence harmonic information from the load oscillation is much larger than that from the eccentric motor. Load torque oscillation also induces negative sequence harmonic information, whose magnitudes are even larger than those resulting from the eccentric motor due to the inherent motor asymmetry and instrumentation imperfections. As for the healthy motor with a constant load condition, only very small amount of positive sequence harmonics can be observed in the current spectrum. These harmonic components which exist in the healthy motor supply currents are often used for sensorless speed estimation.

It is important to note that all three cases have a large amount of negative sequence fundamental information in the supply currents. These negative sequence fundamental components are primarily owing to the dominant effect of the unbalanced mains supply at the fundamental. In order to accurately evaluate the motor asymmetry level at these three conditions, normalized negative sequence components at $-f_e$, $-\left(f_e + f_{rm}\right)$, and $-\left(f_e - f_{rm}\right)$ are calculated respectively and listed in Table 8.1. Obviously, normalized negative sequence harmonic information at $-(f_e + f_{rm})$ and $-(f_e - f_{rm})$ represents a much more reliable indicator to reflect the increased motor asymmetry level caused by rotor eccentricities.

Experiments are further swept through the motor operation range while keeping the average load level in a load oscillation always equal to the constant load applied to the eccentric motor. Normalized negative sequence characteristic harmonic currents are calculated at $-(f_e + f_{rm})$ and $-(f_e - f_{rm})$. Final experimental results are plotted in Figure

8.4 and Figure 8.5, respectively. As stated previously, the negative sequence component for an ideal, healthy motor with a load oscillation should be zero. The fact this component in not zero, is due to the inherent asymmetry in the motor impedance. In addition, the change in the normalized negative sequence harmonic information with respect to the load oscillation level is negligible, except at very small load oscillations. It is important to see that, at both characteristic harmonic frequencies, normalized negative sequence harmonic information for an eccentric motor with a constant load is much larger than that from a healthy motor with a load torque oscillation. From these figures, it is also concluded that normalized negative sequence harmonic information at $-\left(f_e + f_{rm}\right)$ serves as a better fault indicator than that at $-\left(f_e - f_{rm}\right)$ since it provides a larger margin to set up threshold values. In addition, detecting negative sequence harmonic at $-\left(f_e + f_{rm}\right)$ is easier than that at $-\left(f_e - f_{rm}\right)$ since the latter may be obscured by other non-characteristic harmonics due to FFT spectral leakage effects. Experimental results shown here clearly confirm the effectiveness of this newly proposed eccentricity fault indicator, which was previously derived from theoretical analysis and verified by simulation results. By detecting normalized negative sequence harmonic information in the stator current space vector spectrum, a reliable rotor eccentricity diagnostics can be realized even in the presence of a load torque oscillation.

It is also worthy to note that the normalized negative sequence harmonic information is not continuously decreasing as the average load level increases. At the no load condition, positive sequence harmonic components have relatively small magnitudes and therefore the normalized negative sequence harmonic information is larger. As the average load level increases, these proposed additional eccentricity fault indicators

decrease accordingly. However, at some point, normalized negative sequence harmonics begin to increase again.

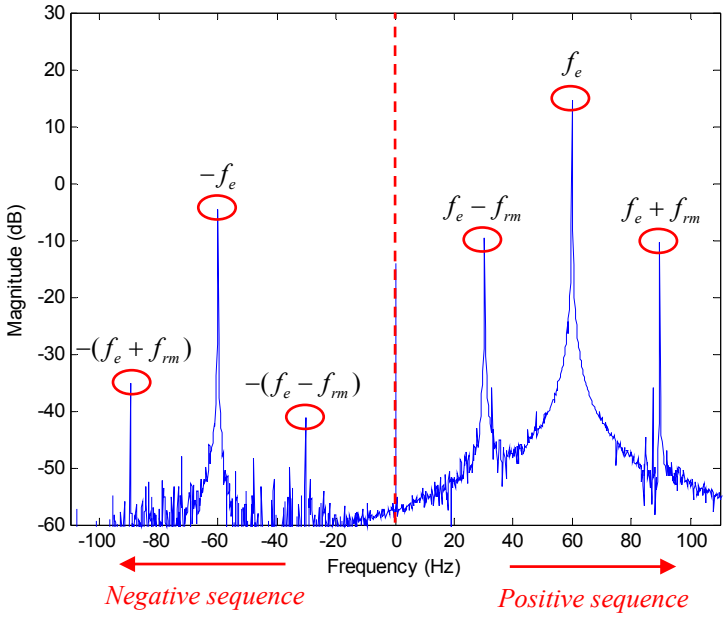

Figure 8.1 Mains-fed eccentric motor $\vec{I}$ spectrum at 1776 rpm with constant load

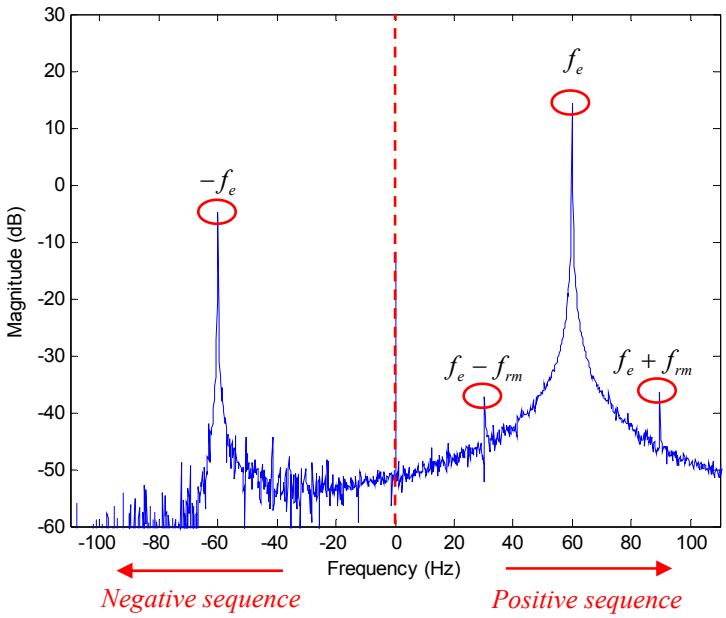

Figure 8.2 Mains-fed healthy motor $\vec{I}$ spectrum at 1776 rpm with constant load

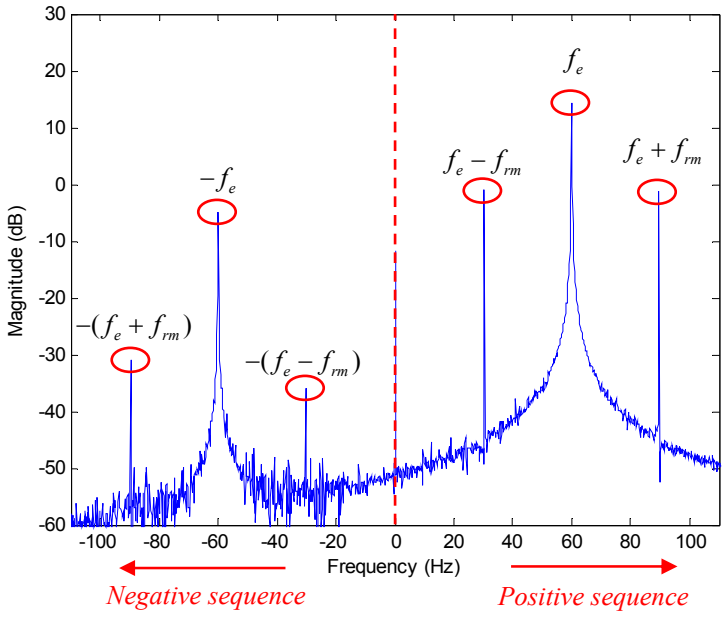

Figure 8.3 Mains-fed healthy motor $\vec{I}$ spectrum at average 1776 rpm with load oscillation

Table 8.1 Normalized negative sequence components at $-f_e$, $-(f_e + f_{rm})$ and $-(f_e - f_{rm})$ in supply currents

Motor and load type	$-f_e$	$-(f_e + f_{rm})$	$-(f_e - f_{rm})$
Eccentric motor with constant load	11.08%	5.72%	2.64%
Healthy motor with constant load	10.85%	Close to zero	Close to zero
Healthy motor with load oscillation	10.90%	3.15%	1.45%

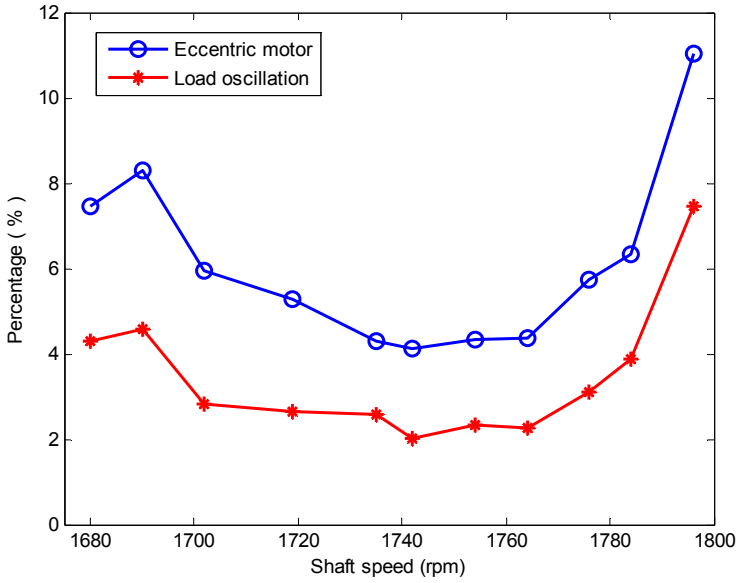

Figure 8.4 Normalized negative sequence harmonic currents at $-(f_e + f_{rm})$ for an eccentric motor with constant load and a healthy motor with load oscillation

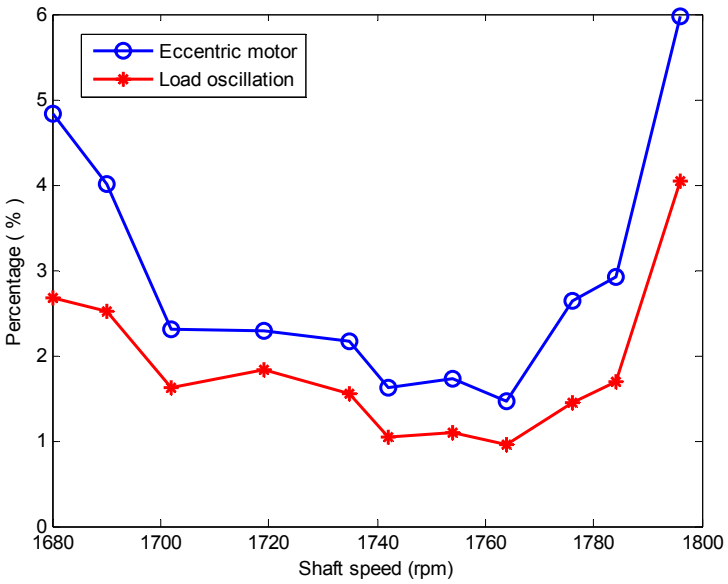

Figure 8.5 Normalized negative sequence harmonic currents at $-(f_e - f_{rm})$ for an eccentric motor with constant load and a healthy motor with load oscillation

8.3 Experimental Results for Closed-Loop Drive-Connected Condition

FFTs of the stator current and terminal voltage space vectors for the eccentric motor are shown in Figure 8.6 and Figure 8.7. The drive reference speed is 1350 rpm, corresponding to a rotor mechanical rotational frequency of 22.5Hz, and a stator excitation frequency of 47.2 Hz. Therefore, eccentricity characteristic harmonics are located at $f_{ecc}^{L} = f_e - f_{rm} = 24.7\text{Hz}$ and $f_{ecc}^{H} = f_e + f_{rm} = 69.7\text{Hz}$, respectively. Similarly, FFTs for the healthy motor at the same operating conditions (same reference speed and constant load level) are shown in Figure 8.8 and Figure 8.9. For the sake of clarity, all spectra magnitudes are expressed in dB again.

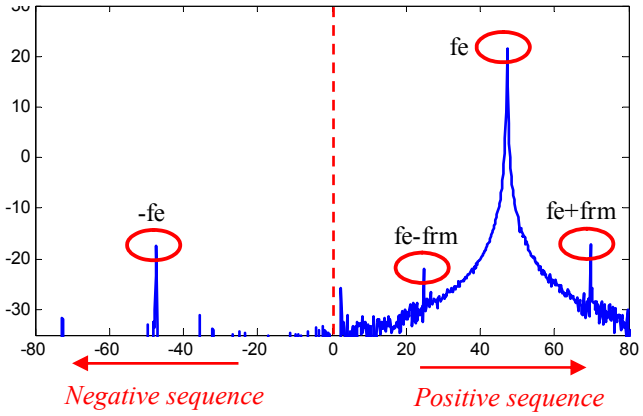

Figure 8.6 FFT spectrum of stator current space vector for the eccentric motor

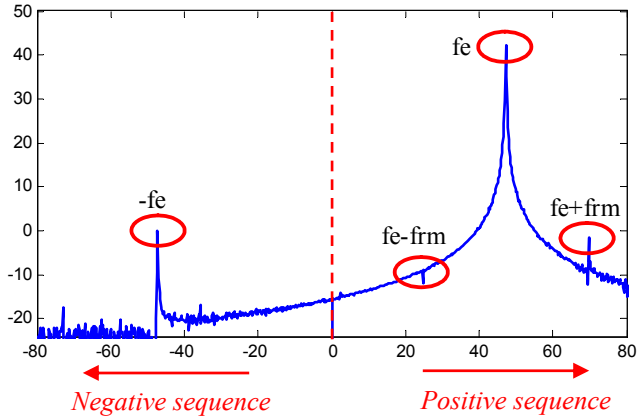

Figure 8.7 FFT spectrum of stator voltage space vector for the eccentric motor

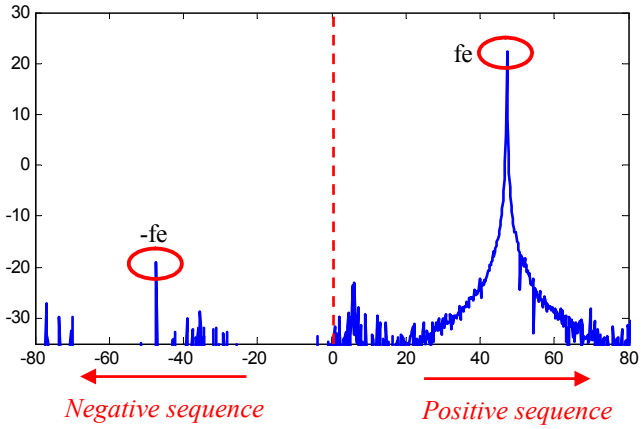

Figure 8.8 FFT spectrum of stator current space vector for the healthy motor

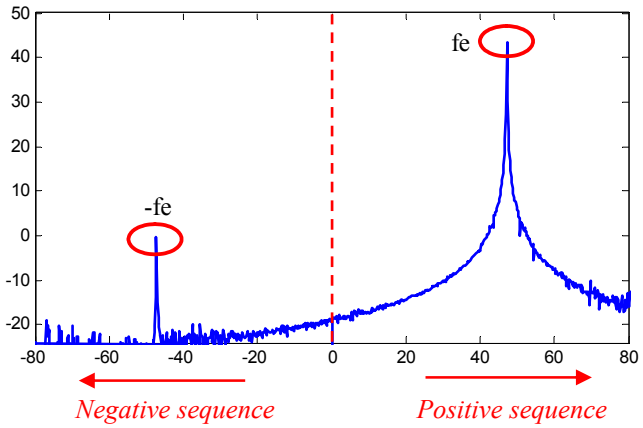

Figure 8.9 FFT spectrum of stator voltage space vector for the healthy motor

It is clear from the figures that the rotor eccentricity characteristic side-band harmonics at f_{ecc}^{L} and f_{ecc}^{H} have significantly increased magnitudes in both the stator current and terminal voltage space vector spectra for the eccentric motor as shown in Figure 8.6 and Figure 8.7, while these components are almost negligible for the healthy motor as shown in Figure 8.8 and Figure 8.9. As for the increased negative sequence fundamental components at $(-f_e)$ resulting from the rotor eccentricity, it is not easy to observe the difference in their magnitudes directly from these space vector spectra due to the inherent motor, drive and instrumentation asymmetry level. In addition, all negative sequence components at eccentricity characteristic harmonics, $(-f_{ecc}^{L})$ and $(-f_{ecc}^{H})$ are negligible in both eccentric and healthy motor spectra owing to the strong PI controller regulation capabilities in a closed-loop drive system.

In order to properly evaluate the increased motor asymmetry caused by a rotor eccentricity fault, normalized stator current and terminal voltage negative sequence components at the fundamental excitation frequency should be calculated accordingly. The value of I_{ne}^{*} is increased from 0.85% to 1.14%, and the value of V_{ne}^{*} is increased

from 0.66% to 0.78% for this operation condition. The total motor asymmetry indicator, δ, which is defined in (5.11), is increased from 1.51% to 1.92%.

Due to the intrinsic control loop low-pass filtering characteristic, the complementary distribution of motor asymmetry information between stator currents and terminal voltages depends on both the frequency and the load level. Therefore, a single indicator from either normalized negative sequence current or normalized negative sequence voltage is not sufficient.

In the experiments, the motor reference speed is varied continuously from 300 rpm to 1750 rpm with 50 rpm steps for both the eccentric and the healthy motor. The resistor bank connected to the dc generator dynamometer is kept constant (12 × 50 ohm) during this process. Three motor asymmetry indexes, I_{ne}^{*}, V_{ne}^{*} and δ, are plotted in Figure 8.10 through Figure 8.12, respectively. Obviously, the total motor asymmetry indicator, δ, provides a much more reliable signature of increased motor asymmetry compared with the single component indicator, I_{ne}^{*} or V_{ne}^{*}. This additional motor asymmetry information resulting from a rotor eccentricity fault can be monitored to effectively eliminate load oscillation effects for rotor eccentricity detection in a closed-loop induction motor drive.

Notice that in the inverter-fed case, the change in asymmetry indicator is less than that in the mains-fed case. This is due to the fact that the main-fed case utilizes the negative sequence harmonic information, while the inverter-fed case using the fundamental negative sequence components. The inverter supply, while nearly balanced, does contain some inherent negative sequence information, especially at low speed, due to the IGBT dead time in the inverter control. This phenomenon is clear in Figure 8.10 and Figure 8.11. In these figures, the normalized fundamental negative sequence voltage

and current are varying significantly from one operating point to the next at low speed. The curves then smooth out at higher speeds.

In general, the total percentage of negative sequence information in a machine increases with respect to the motor speed due to the inductive nature of the induction motor, except for very low speed and mechanical resonance points. In addition, the inherent motor asymmetry is also a function of the stator excitation frequency and the slip frequency. In order to properly compensate for the inherent asymmetry from the motor, drive and instrumentation through the whole operating range, thresholds should be carefully calculated during the motor commissioning stage. Such techniques [44]-[49] have been well developed for incipient stator inter-turn fault detection by either using data lookup table or neural network schemes.

8.4 Reliable Rotor Eccentricity Detection Scheme

Finally, a full rotor eccentricity detection scheme is proposed in Figure 8.13. Three phase stator currents and two line-line voltages are first sampled and then transformed into space vectors. FFT analysis of these spectra yields harmonic magnitudes corresponding to rotor eccentricity characteristic signatures. Inherent motor and instrumentation asymmetry level is also calculated during the commissioning stage. For some critical industrial applications, zero sequence voltage information should be detected as well to compensate for additional motor asymmetry caused by stator inter turn faults. Combing all three fault indicators together, a reliable rotor eccentricity fault diagnostics can be achieved by following the proposed online condition monitoring scheme as shown in Figure 8.13. This method can effectively eliminate the impacts from

a rotor position-dependent load torque oscillation and prevent dependence on accurate estimation of motor parameters.

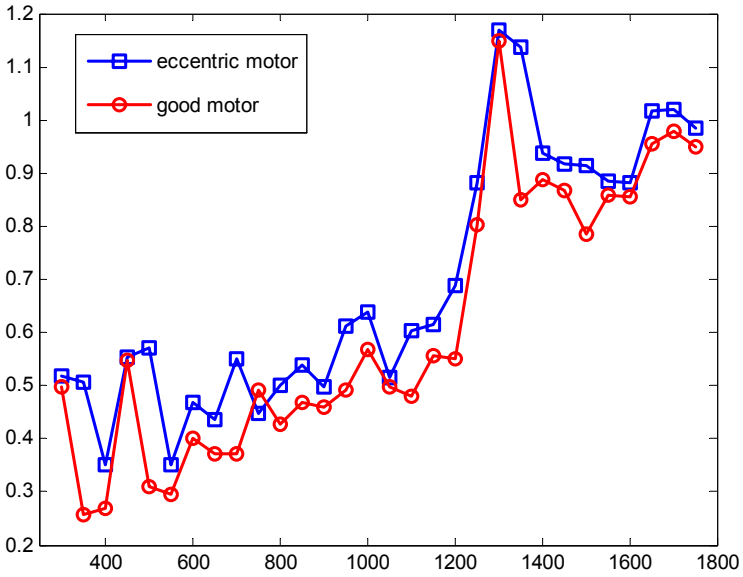

Figure 8.10 Normalized fundamental negative sequence stator current vs. reference speed

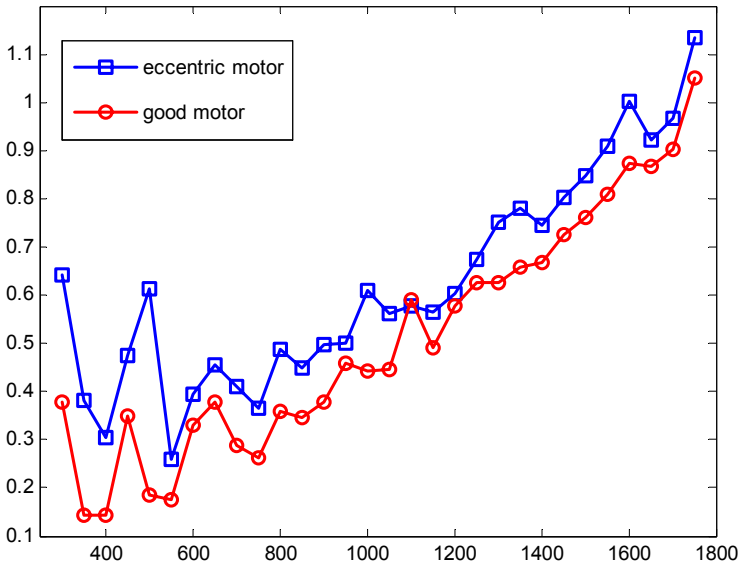

Figure 8.11 Normalized fundamental negative sequence stator voltage vs. reference speed

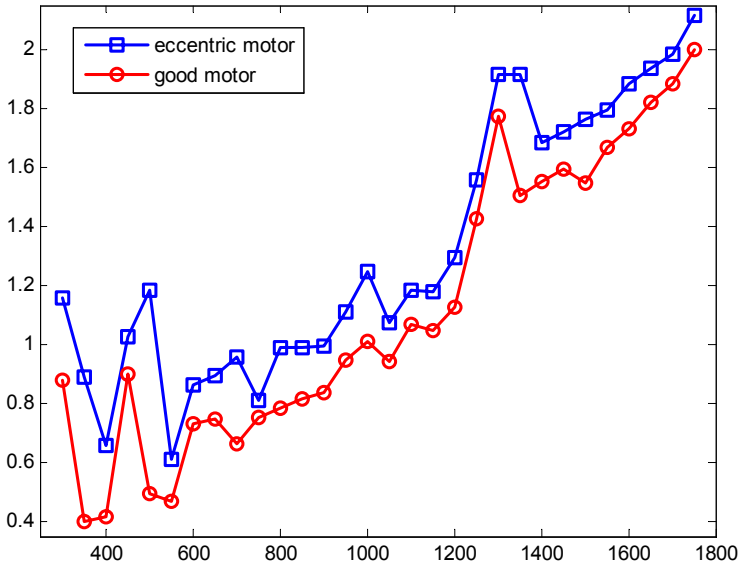

Figure 8.12 Normalized total fundamental negative sequence components vs. reference speed

8.5 Chapter Summary

Extensive experiments have been performed for both the eccentric motor and the healthy motor under constant load and oscillating load conditions, respectively. Experimental results presented in this chapter demonstrate the efficacy of the proposed additional rotor eccentricity indicator to eliminate load oscillation effects. Considering the inherent asymmetry level of the motor and instrumentation as well as the possible stator inter-turn faults, a comprehensive online rotor eccentricity detection scheme is proposed at the end of the chapter to guide the future implementation of a comprehensive online rotor eccentricity condition monitoring system.

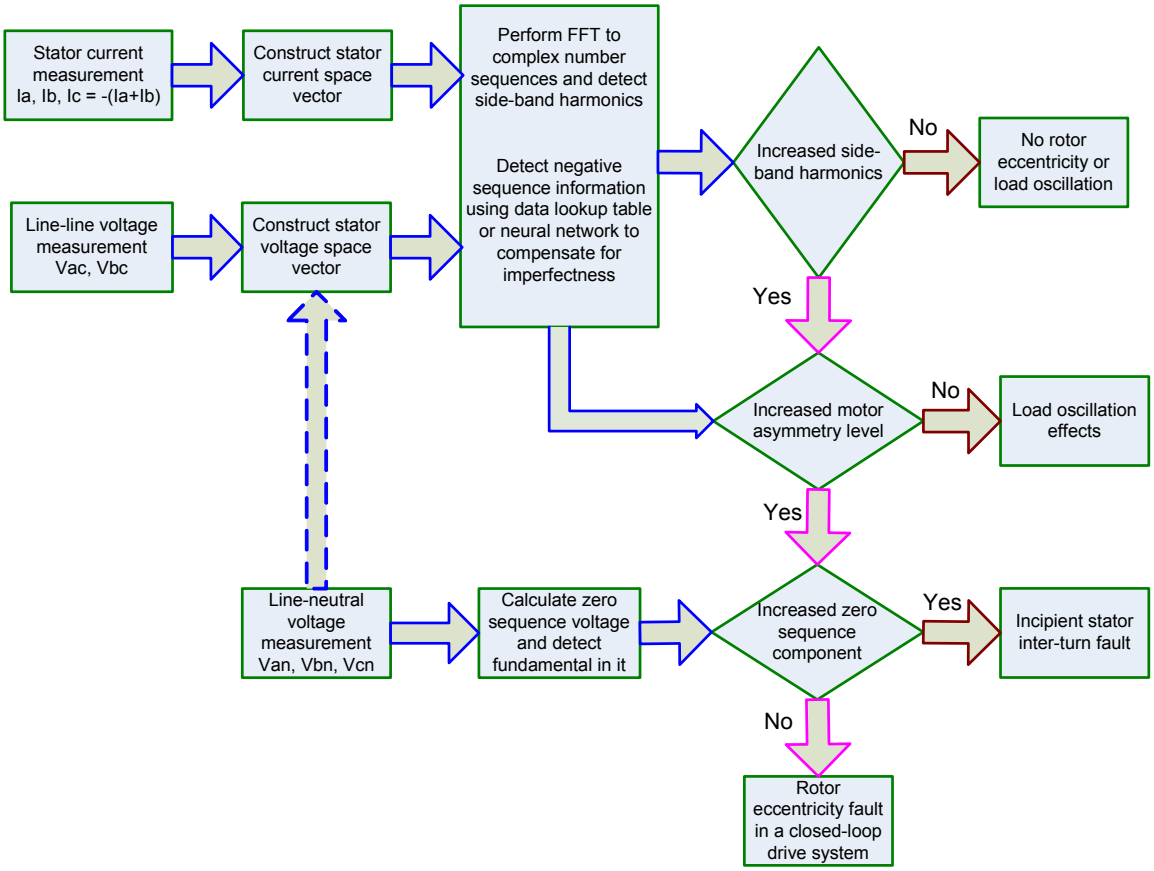

Figure 8.13 Proposed complete online rotor eccentricity fault detection scheme for induction motors

CHAPTER 9

CONCLUSIONS, CONTRIBUTIOINS, AND RECOMMENDATIONS FOR FUTURE WORK

9.1 Conclusions

The traditional method used to detect rotor eccentricities monitors only a single phase stator current spectrum, which may be overwhelmed by a position-dependent load torque oscillation. Previous techniques used to differentiate these two effects rely heavily on the accurate estimate of motor parameters, which is in general impossible considering the temperature rise, magnetic saturation as well as skin effects. The objective of this research is to develop a reliable and computationally efficient method to effectively detect rotor eccentricity faults in the presence of a load torque oscillation.

A detailed magnetic field analysis is performed to investigate the airgap permeance modulation caused by a rotor eccentricity. Based on the modified stator and rotor MMFs, all machine inductances and their derivatives are reformulated. Similar to a stator turn fault, rotor eccentricities also increase the motor asymmetry level. On the other hand, a position dependent load torque oscillation is still connected to a healthy motor. Ideally only positive sequence information exists. Therefore, the additional motor asymmetry caused by a rotor eccentricity serves as the newly proposed rotor fault indicator in the presence of a load toque oscillation. For a mains-fed machine, normalized negative sequence harmonic information is assessed since the fundamental is significantly polluted by the unbalanced power supply. For an inverter-fed machine, due to the relatively

strong PI controller regulation capabilities, negative sequence fundamental information in both the stator currents and the terminal voltages should be monitored.

To accurately extract negative sequence harmonic information, FFT analysis is applied to the stator current space vector, as opposed to using the traditional symmetrical component decomposition or a rotating reference frame transformation. This new FFT approach has significant advantages over the other two techniques since it has the capability to separate sequence components at all frequencies simultaneously with minimum ambiguity.

To be a reliable rotor fault indicator, the rotor eccentricity induced negative sequence information has to be separated from other sources, such as the motor inherent unbalance, instrumentation imperfection, stator turn fault, etc. Inherent motor non-idealities can be properly compensated using either neural network or data look up table techniques during the motor commissioning stage. To separate rotor eccentricity induced negative sequence information from those associated with a stator turn fault, zero-sequence information serves as the last resort to deal with this problem.

Motor dynamic performance can be simulated by using either a Matlab Simulink model or a Finite Element Model. Matlab model focuses only on the airgap permeance modulation effects and neglects all other factors. An FEA model gives much more accurate results while paying the price of an extremely long simulation time. Both types of simulation clearly demonstrate the existence of the proposed rotor fault indicators.

Extensive experimental investigations are taken for both an eccentric motor with a constant load and a healthy motor with an oscillating load. Experimental results clearly demonstrate that a healthy motor with a significant degree of load oscillation yields much

larger magnitudes at the positive sequence harmonics than those resulting from an eccentric motor with a constant load. In addition, due to the inherent motor unbalance and instrumentation mismatch, the magnitudes at the negative sequence harmonics resulting from a load oscillation are close to or even larger than those from a rotor eccentricity. In other words, separating rotor eccentricities from a load torque oscillation should not rely on purely detecting the magnitudes of the negative sequence harmonics. Experimental results also show that the normalized negative sequence fundamental currents are almost same for both the eccentric and the healthy motors owing to the dominant unbalanced power supply. Therefore, only the normalized negative sequence harmonics serve as the reliable rotor fault indicators and provide sufficient threshold margins to eliminate load oscillation effects for a mains-fed machine.

As for the drive-connected machines, negative sequence harmonic information is negligible due to the PI controller strong regulation capabilities. Experimental results explicitly show that rotor eccentricity induced motor asymmetry is reflected in both the stator currents and the terminal voltages. This complimentary distribution of negative sequence information in motor terminal quantities is dependent on the drive excitation frequency and the slip frequency. Therefore, the summation of the normalized negative sequence fundamental components in both the stator currents and the terminal voltages should be monitored for a closed-loop drive.

It is important to note that the newly proposed rotor fault indicators for both mains-fed and drive-connected induction motors, similar to the regular eccentricity indicators, are highly nonlinear with respect to the load level. To accurately set up the threshold

values for these fault signatures, it is necessary to go through the entire motor operating range during the learning stage for online condition monitoring.

9.2 Contributions

First, a comprehensive literature review of existing techniques regarding separating load effects from rotor faults detection was presented and carefully analyzed. This led to the final development of a comprehensive algorithm to completely eliminate load effects from the rotor faults detection.

A detailed analysis of airgap magnetic field in the presence of a mixed eccentricity was then developed and all the machine inductances were reformulated accordingly. This procedure not only facilitates the induction motor dynamic simulation using Matlab model instead of adopting a time-consuming FEA model, but also provides a fundamental understanding of machine operating characteristics under fault conditions.

A new FFT technique was proposed to very efficiently extract negative sequence information from 3-phase terminal quantities for all frequency components simultaneously. This method also eases the construction of the per-phase sequence components based on the phase-phase measurement.

A new rotor fault indicator was then proposed for both mains-fed machines and drive-connected machines to effectively detect the eccentricity fault in the presence of a load torque oscillation. To the author's knowledge, for the first time, the negative sequence information in the supply currents or the terminal voltages due to an eccentricity fault was proposed to be a rotor fault indicator with both simulation and experimental verifications.

Finally, a reliable, computationally efficient and comprehensive algorithm has been developed for both mains-fed and drive-connected induction motors to completely eliminate load effects. In addition, inherent motor unbalance and possible stator turn fault induced negative sequence information are properly compensated or separated from the additional motor asymmetry caused solely by a rotor eccentricity.

9.3 Recommendations for Future Work

Although a comprehensive eccentricity fault detection scheme has been proposed to completely eliminate load oscillation effects, it has not been tested on a practical industrial load with an oscillating characteristic, such as a reciprocating compressor. The effectiveness of the proposed scheme is only experimentally proven through one man-made eccentric motor with a fixed degree of rotor eccentricities. Hence, it is necessary to test the newly proposed fault indicators under different levels of rotor eccentricities as well as oscillating loads to perform the sensitivity analysis for the normalized negative sequence information.

Theoretical analysis and simulation results have shown that the zero sequence voltage remains unchanged for an eccentric motor. This characteristic can be utilized to distinguish rotor eccentricity induced motor asymmetry from that resulting from a stator turn fault. However, this conclusion also needs to be further experimentally verified under the condition of slight insulation degradation in stator windings.

The proposed normalized negative sequence harmonic information for a mains-fed machine works quite well since it provides a large margin between the eccentric motor and the healthy motor with a load oscillation. However, the proposed summation of the normalized negative sequence fundamental information in both the supply currents and

the terminal voltages only gives a small margin to set up the threshold values due to the strong PI controller regulation capabilities. Further research needs to focus on the drive-connected induction motors to improve the reliability and sensitivity of detecting eccentricity faults in the presence of a load torque oscillation.

Finally, further work should be done on integrating this technique into an overall motor AND load fault detection scheme. Little work has been done to date on detecting incipient faults in loads such as pumps and compressors. The diagnostic techniques proposed here should be used in concert with current-based methods to detect abnormal operating conditions in rotating equipment that is closely mechanically coupled to the motor. Faults in the load will alter the level and characteristic of the load-induced harmonics in the stator current spectrum.

APPENDIX A

MOTOR PARAMETERS USED FOR SIMULATION

Table A.1 Motor parameters used for simulation

R_s	0.232001ohm
R_r	0.241179 ohm
X_{ls}	0.472706 ohm
X_{lr}	0.966634 ohm
X_m	37.2841 ohm
f	60 Hz
$Poles$	2
V_{L_L}	460 Volts
J_{eq}	0.1 kg·m^2
n_{rated}	3555 rpm
s_{rated}	0.0125
T_{load_rated}	27.5633 N·m

APPENDIX B

MOTOR AND DRIVE PARAMETERS USED FOR EXPERIMENTS

Table B.1 Nameplate information for the experimental motor

Manufacturer	GE
Model #	5KE213BC205B
Frequency	60 Hz
Rated power	7.5 hp
RPM	1755
Voltage	**230**/460 Volts
Current	**18.2**/9.1 Ampere
Power factor	86.5%
Frame	213 T
NEMA design	A

Table B.2 Impedance information for the experimental motor

	460 volts connection parameters (delta equivalent)	230 volts connection parameters (delta equivalent)	230 volt connection Parameters (wye equivalent)
R_1 (ohms @25C)	2.0885	0.5221	0.1740
L_1 (mH)	16.5400	4.1350	1.3783
R_2 (ohms @25C)	1.9167	0.4792	0.1597
L_2 (mH)	21.1100	5.2775	1.7592
L_m (mH)	633.2900	158.3225	52.7742
Airgap length (inch)	0.014		
# of stator slots	48		
# of rotor bars	40		

Table B.3 Main parameters for the Allen-Bradley drive and encoder

Manufacturer	Allen-Bradley
Model #	1336E-B020-AA-EN-HA2-L7E
Voltage	380-480 Volts AC
Frame size	B
Enclose type	AA
Power rating	20 hp (15 kw)
Output frequency	0-200 Hz
Current loop bandwidth	2000 rad/s used in experiments
Speed loop bandwidth	16 rad/s used in experiments
PWM frequency	12 kHz used in experiments
L option board	L7E
Encoder model	Allen-Bradley 845S
Encoder type	Incremental, Optical
Encoder supply voltage	5 Volts DC
Encoder resolution	1024 ppr

APPENDIX C

INTRODUCTIOIN TO SHARK DSP BOARD

USED FOR CREATING LOAD OSCILLATIOIN

The DSP board used for creating an oscillating load is the ADSP-21061 EZ-KIT Lite™ evaluation kit. The evaluation board is designed to be used with VisualDSP++™ development environment and is based on the ADSP-21061 SHARC floating-point digital signal processor (DSP). Figure C.1 illustrates the layout of the ADSP 21061 EZ-KIT Lite board.

The ADSP-21061 SHARC processor can be accessed by using a PC through a serial port. The monitor program that runs on the EZ-KIT Lite gives the user access to the ADSP-21061 processor's internal memory space through the serial port. The pushbutton and user programmable LEDs provide user control and board status. Additionally, the AD1847 SoundPort codec provides access to an audio input and an audio output, which are not used in the experimental investigation of a load oscillation.

The ADSP-21061 processor operates at 40 MHz and has four I/O flags that the user can program as inputs or outputs. Bits in the MODE2 register control the direction (1=output and 0=input) and bits in the ASTAT (arithmetic status) register contain the value of each of the flag pins. Flag0, 1, 2 and 3 are also connected to LED D2, D3, D4 and D6, respectively. The LED is lit when the flag is cleared. The SHARC DSP also has three external interrupt pins. They are prioritized, individually maskable (IMASK register), and can be configured to be either edge sensitive or level sensitive, which is controlled by bits in MODE2 register again.

In the experiment, to control the on/off status of IGBTs which are serially connected to the resistor banks, all four I/O flags on the DSP board are configured as outputs. Meanwhile, IRQ0-IRQ2 are set to be edge sensitive to guide the flags to output proper voltage level (2 volts or 0) to the IGBT driving circuit according to the rising edge of clock signals.

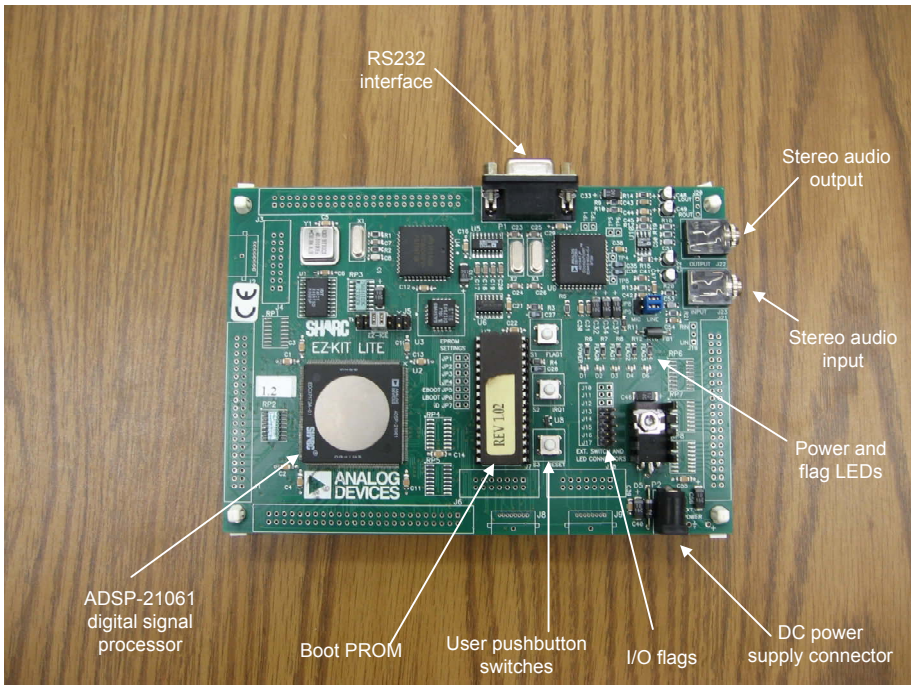

Figure C.1 ADSP 21061 EZ-KIT Lite board layout

REFERENCES

[1] W. T. Thomson; and M. Fenger; "Current signature analysis to detect induction motor faults," *IEEE Industry Applications Magazine*, vol. 7, iss. 4, pp. 26-34, July-Aug. 2001.

[2] S. M. A. Cruz, A. J. M. Cardoso, and H. A. Toliyat, "Diagnosis of stator, rotor and airgap eccentricity faults in three-phase induction motors based on the multiple reference frames theory," *Conference Record of the 2003 IEEE Industry Applications Conference*, vol. 2, pt. 2, p. 1340-1346, 2003.

[3] G. B. Kliman and J. Stein, "Induction motor fault detection via passive current monitoring," in *Proc. Int. Conf. Electrical Machines*, pp. 13-17, Aug. 1990.

[4] S. Nandi, S. Ahmed, and H. Toliyat, "Detection of rotor slot and other eccentricity related harmonics in a three phase induction motor with different rotor cages", *IEEE Transactions on Energy Conversion*, v 16, n 3, p 253-60, Sept. 2001.

[5] R. R. Schoen and T. G. Habetler, "Effects of time-varying loads on rotor fault detection in induction machines," *IEEE Transactions on Industry Applications*, vol. 31, no. 4, pp. 900-906, July-Aug. 1995.

[6] R. R. Schoen and T.G. Habetler, "Evaluation and implementation of a system to eliminate arbitrary load effects in current-based monitoring of induction machines," *IEEE Transactions on Industry Applications*, vol. 33, no. 6, pp. 1571-1577, Nov.-Dec. 1997.

[7] R. R. Schoen and T. G. Habetler, "A new method of current-based condition monitoring in induction machines operating under arbitrary load conditions," *Electric Machines and Power Systems*, v 25, n 2, p 141-52, Feb.-March 1997.

[8] S. M. A. Cruz and A. J. M. Cardoso, "Rotor cage fault diagnosis in operating three-phase induction motors, under the presence of time-varying loads," *9th European Conference on Power Electronics and Applications*, p 11 pp, EPE 2001.

[9] A. J. M. Cardoso, S. M. A. Cruz, J. F. S. Carvalho, and E. S. Saraiva, "Rotor cage fault diagnosis in three-phase induction motors, by Park's vector approach,"

Conference Record of the 1995 IEEE Industry Applications Conference, vol. 1, pt. 1, p. 642-646, 1995.

[10] C. Kral, F. Pirker, and G. Pascoli, "Influence of load torque on rotor asymmetry effects in squirrel cage induction machines including detection by means of the Vienna monitoring method," *9th European Conference on Power Electronics and Applications*, p. 9 pp, EPE 2001.

[11] C. Kral, F. Pirker, G. Pascoli, and H. Oberguggenberger, "On the sensitivity of induction machine rotor cage monitoring ─ the Vienna monitoring method", *Symposium on Power Electronics, Electrical Drives Automation and Motion*, p. B1/13-18, 2000.

[12] R. R. Obaid and T. G. Habetler, "Current-based algorithm for mechanical fault detection in induction motors with arbitrary load conditions", *Conference Record of the 2003 IEEE Industry Applications Conference*, pt. 2, p 1347-51 vol.2, 2003.

[13] R. R. Obaid and T. G. Habetler, "A simplified technique for detecting mechanical faults using stator current in small induction motors", *Conference Record of the 2000 IEEE Industry Applications Conference*, pt. 1, p 479-83, vol.1, 2000.

[14] X. Huang, and T. G. Habetler, "Detection of rotor eccentricity faults in closed-loop drive-connected induction motors using an artificial neural network", *IEEE 35th Annual Power Electronics Specialists Conference*, pt. 2, p 913-18, Vol.2, 2004.

[15] G. Salles, F. Filippetti, C. Tassoni, G. Crellet, and G. Franceschini, "Monitoring of induction motor load by neural network techniques," *IEEE Transactions on Power Electronics*, vol. 15, no. 4, pp. 762-768, July 2000.

[16] F. Filippetti, G. Franceschini, C. Tassoni, G. Salles, and G. Grellet, "Monitoring of induction machines load torque disturbances: An alternative NN-based approach," in *Proc. IEEE-IAS'98*.

[17] F. Filippetti, G. Franceschini, and C. Tassoni, "NN aided on line diagnostics of induction motor rotor faults," *IEEE Transactions on Industrial Applications,* vol. 31, pp.892-899, July/Aug. 1995.

[18] F. Filippetti, G. Franceschini, C. Tassoni and P. Vas, "AI techniques in induction machines diagnosis including the speed ripple effect," *IEEE. Transactions on Industrial Applications*, vol.34, pp. 98-108, Jan/Feb. 1998.

[19] M. Drif, N. Benouzza, A. Bendiabdellah, and J. A. Dente, "Induction motor load effect diagnostic utilizing instantaneous power spectrum," *9th European Conference on Power Electronics and Applications*, p. 10 pp, EPE 2001.

[20] F. Stanislaw, etc., "Instantaneous power as a medium for the signature analysis of induction motors," *IEEE Transactions on Industrial Applications*, vol. 32, pp. 904-909, July/Aug. 1996.

[21] M. Blodt, J. Faucher, B. Dagues, and M. Chabert, "Mechanical Load Fault Detection in Induction Motors by Stator Current Time-Frequency Analysis," *IEEE International Electric Machines and Drives Conference*, pp. 1881-1888, 2005.

[22] M. Blodt, J. Regnier, and J. Faucher, "Distinguishing load torque oscillations and eccentricity faults in induction motors using stator current wigner distributions," *Conference Record of the 2006 IEEE Industry Applications Conference*, Oct. 2006.

[23] D. G. Dorrell, "The effects of dynamic rotor eccentricity in cage induction motors," in *Proc. UPEC'94*, University College Galway, Galway, Ireland, 1994, pp. 402-405.

[24] D. G. Dorrell, W. T. Thomson, S. Roach, "Analysis of airgap flux, current, and vibration signals as a function of the combination of static and dynamic airgap eccentricity in 3-phase induction motors," *IEEE Transactions on Industrial Applications*, vol. 33, no. 1, pp. 24-34, Jan.-Feb. 1997.

[25] S. Nandi, R. M. Bharadwaj, H. A. Toliyat, "Performance analysis of a three-phase induction motor under mixed eccentricity condition," *IEEE Transactions on Energy Conversion*, vol. 17, no. 3, pp. 392-399, Sep. 2002.

[26] S. Nandi, R. M. Bharadwaj, H. A. Toliyat; "Mixed eccentricity in three phase induction machines: analysis, simulation and experiments," *Conference Record of the 2002 IEEE Industry Applications Conference*, vol. 3, pp.1525-1532, Oct. 2002.

[27] J. R. Cameron, W. T. Thomson, A. B. Dow, "Vibration and current monitoring for detecting airgap eccentricity in large induction motors," *IEE Proceedings* B, vol. 133, no. 3, pp. 155-163, May 1986.

[28] J. R. Cameron, W. T. Thomson, A. B. Dow, "Online current monitoring of induction motors-a method for calculating the level of airgap eccentricity," *Third International Conf. on Electrical Machines and Drives*, pp. 173-178, 1987.

[29] N. A. Al-Nuaim and H. Toliyat, "A novel method for modeling dynamic air-gap eccentricity in synchronous machines based on modified winding function theory," *IEEE Transactions on Energy Conversion*, vol. 13, no. 2, pp. 156-162, June 1998.

[30] H. Toliyat, M. Arefeen, and A. Parlos, "A method for dynamic simulation of air-gap eccentricity in induction machines," *IEEE Transactions on Industrial Applications*, vol. 32, pp. 910-918. July/Aug. 1996.

[31] S. Nandi, H. Toliyat, and A. Parlos, "Performance analysis of a single phase induction motor under eccentric condition," *Conference Record of the 1997 IEEE Industry Applications Conference*, pp. 174-181, 1997.

[32] T. J. Sobczyk, P. Vas, and C. Tassoni, "Models for induction motors with air-gap asymmetry for diagnostic purposes," *in Proc. International Conference on Electrical Machines (ICEM 1996)*, vol. 2, pt. 2, pp. 79-84, 1996.

[33] T. J. Sobczyk, P. Vas, and C. Tassoni, "A comparative study of effects due to eccentricity and external stator and rotor asymmetries by monoharmonic models," *in Proc. International Conference on Electrical Machines (ICEM 2000)*, vol. 2, pt. 2, pp 946-950, 2000.

[34] P. C. Krause, *Analysis of Electric Machinery*. New York: McGraw-Hill, 1986.

[35] J. L. Blackburn, *Symmetrical Components for Power Systems Engineering*, Marcel Dekker, New York, 1993.

[36] A. E. Fitzgerald, C. Kingsley, S. D. Umans, *Electric Machinery*, McGraw-Hill, 6th edition, July 2002.

[37] R. R. Schoen, "On-Line Current-Based Condition Monitoring of Three-Phase Induction Machines," *Ph.D. Dissertation*, School of Electrical and Computer Engineering, Georgia Institute of Technology, August 1994.

[38] R. R. Obaid, "Detection of Rotational Mechanical Asymmetry in Small Induction Machines," *Ph.D. Dissertation*, School of Electrical and Computer Engineering, Georgia Institute of Technology, May 2003.

[39] N. Mohan, *Electric Drives: An Integrative Approach*, MNPERE, June 2004.

[40] N. Mohan, A*dvanced Electric Drives: Analysis, Control and Modeling using Simulink*, MNPERE, October 2001.

[41] X. Huang, "Diagnostics of Air Gap Eccentricity In Closed-Loop Drive Connected Induction Motors," *Ph.D. Dissertation*, School of Electrical and Computer Engineering, Georgia Institute of Technology, May 2005.

[42] X. Huang, and T. G. Habetler, "Detection of mixed air gap eccentricity in closed-loop drive-connected induction motors," *IEEE International Symposium on Diagnostics for Electric Machines, Power Electronics and Drives (SDEMPED 2003)*, p 312-16, 2003.

[43] X. Huang, and T. G. Habetler, "Analysis of air gap eccentricity in closed-loop drive-connected induction motors", *IEEE International Electric Machines and Drives Conference*, pt. 3, p 1443-7 vol.3, 2003.

[44] R. M. Tallam, T. G. Habetler, and R. G. Harley, "Stator winding turn-fault detection for closed-loop induction motor drives," *IEEE Transactions on Industry Applications*, vol. 39, no. 3, pp. 720-724, May-June 2003.

[45] G. B. Kliman, W. J. Premerlani, R. A. Hoegl, and D. Hoeweler, "A new approach to on-line turn fault detection in ac motors," Conf. Rec. IEEE-IAS Annual Meeting, vol. 1, pp. 687-693, 1996.

[46] J. Sottile, F. C. Trutt, and J. L. Kohler, "Experimental investigation of on-line methods for incipient fault detection," *Conference Record of the 2000 Industrial Applications Conference*, vol. 4, pp. 2682-2687, 2000.

[47] J. Sottile, F. C. Trutt, J. L. Kohler, "Condition monitoring of stator windings in induction motors II Experimental investigation of voltage mismatch detectors," *IEEE Transactions on Industry Applications*, vol. 38, iss. 5, pp. 1454-1459, Sept.-Oct. 2002.

[48] J. L. Kohler, J. Sottile, F. C. Trutt, "Condition monitoring of stator windings in induction motors I Experimental investigation of the effective negative-sequence impedance detector," *IEEE Transactions on Industry Applications*, vol. 38, iss. 5, pp.1447-1453, Sept.-Oct. 2002.

[49] S. B. Lee, R. M. Tallam, T. G. Habetler, "A robust, on-line turn-fault detection technique for induction machines based on monitoring the sequence component

impedance matrix," *IEEE Transactions on Power Electronics*, vol. 18, no. 3, pp. 865-872, May. 2003.

[50] M. A. Cash; T. G. Habetler; G. B. Kliman, "Insulation failure prediction in AC machines using line-neutral voltages", *IEEE Transactions on* Industry Applications, vol. 34, iss. 6, pp. 1234-1239, Nov.-Dec. 1998.

[51] M. A. Cash; and T. G. Habetler; "Insulation failure prediction in inverter-fed induction machines using line-neutral voltages," *Applied Power Electronics Conference and Exposition (APEC '98)*, vol. 2, pp. 1035-1039, Feb. 1998.

[52] M. W. Degner, A. B. Diez, "Diagnostics of induction machines using the zero sequence voltage," *Conference Record of the 2004 Industrial Applications Conference*, vol. 2, pp. 735-742, Oct. 2004.

[53] F. Briz, M.W. Degner, P. Garcia, A. B. Diez, "Induction machine diagnostics using zero sequence component, " *Conference Record of the 2005 Industrial Applications Conference*, vol. 1, pp. 34-41, Oct. 2005.

[54] Z. Gao, T. G. Habetler, R. G. Harley, "A robust rotor temperature estimator for induction machines in the face of changing cooling conditions and unbalanced supply," *IEEE International Electric Machines and Drives Conference*, pp. 591-596, May 2005.

[55] L. Wu, T. Habetler, and R. Harley, "Separating load torque oscillation and rotor fault effects in stator current-based motor condition monitoring," *IEEE International Electric Machines and Drives Conference*, pp. 1889-1894, 2005.

[56] L. Wu, B. Lu, T. Habetler, and R. Harley, "Improved online condition monitoring using static eccentricity-induced negative sequence current information in induction machines," in *Proc. 31st Annual Conference of the IEEE Industrial Electronics Society (IECON'05)*, pp. 1737-1742, Nov. 2005.

[57] L. Wu, Z. Gao, T. G. Habetler, and R. G. Harley, "An Effective Technique on Extracting Negative Sequence Harmonic Information in Stator Current Based Induction Motor Condition Monitoring," in *Proc. 17th IEEE International Conference on Electric Machines 2006 (ICEM 2006)*, Sep. 2006.

[58] A. Cash, "Detection of Turn Faults Arising from Insulation Failure in the Stator Windings of AC Machines," *Ph.D. Dissertation*, School of Electrical and Computer Engineering, Georgia Institute of Technology, Aug. 1998.

VITA

Mr. Long Wu was born in Wuhu, Anhui Province, China on October 17, 1976. He received the dual Bachelor of Engineering degrees in Electrical Engineering (Power System and its Automation) and Accounting from Shanghai Jiao Tong University (SJTU), China in 1998, and the Master of Science degree in Electrical Engineering from Marquette University, Milwaukee, WI in 2003, respectively.

In August 2003, he began his graduate study at Georgia Institute of Technology, Atlanta, GA, where he is pursuing the Ph.D. degree in Electrical Engineering. While at Georgia Tech, he has been working as a Graduate Research Assistant in Power Electronics and Electric Machines Lab in the school of Electrical and Computer Engineering. His research interests include condition monitoring of electrical machines and drives system, electrical machine design, motion control and power electronics.

He is a member of Eta Kappa Nu (HKN). He is also a student member of IEEE and the IEEE Power Engineering Society's Georgia Tech Chapter.